Dipl.-Ing. Martin Schnedlitz

To be or not to be alloyed: Alloying and structural rearrangements in core-shell nanoparticles

DOCTORAL THESIS

For obtaining the academic degree
Doktor der technischen Wissenschaften

Doctoral Programme of Technical Sciences
Technical Physics

Graz University of Technology

Supervisor: Assoc. Prof. Mag. Dipl.-Ing. DDr. Andreas W. Hauser
Co-Supervisor: Em. Univ. Prof. Dipl.-Phys. Dr. Wolfgang E. Ernst
Institute of Experimental Physics

Graz, 2020

Deutsche Fassung:
Beschluss der Curricula-Kommission für Bachelor-, Master- und Diplomstudien vom 10.11.2008
Genehmigung des Senates am 1.12.2008

EIDESSTATTLICHE ERKLÄRUNG

Ich erkläre an Eides statt, dass ich die vorliegende Arbeit selbstständig verfasst, andere als die angegebenen Quellen/Hilfsmittel nicht benutzt, und die den benutzten Quellen wörtlich und inhaltlich entnommenen Stellen als solche kenntlich gemacht habe.

Graz, am ……. ……..
(Unterschrift)

Englische Fassung:

STATUTORY DECLARATION

I declare that I have authored this thesis independently, that I have not used other than the declared sources / resources, and that I have explicitly marked all material which has been quoted either literally or by content from the used sources.

……. ……..
date (signature)

Abstract

Nanosized bimetallic clusters and particles are receiving increased attention as the combination of surface-size effects and intermetallic interactions can trigger unexpected physical properties and generate new phenomena which are unknown for bulk systems. Potential applications cover a wide range of fields, including heterogeneous catalysis, optics, electronics and biomedical applications.

In contrast to bulk alloys, the spatial distribution of the components in a bimetallic particle plays a key role in determining the final functionality of the system. One particularly appealing configuration when dealing with magnetic particles is the so-called "core-shell" structure, where a magnetic core is covered by a protective layer. Such hybrid systems are promising candidates for medical applications including diagnostic as well as therapeutic purposes. On one hand, a protective layer with a thickness of several nanometres prevents the metallic core from oxidation. On the other hand, the use of an appropriate biocompatible coating permits the passivation of potentially harmful magnetic materials. However, in most cases, bimetallic core-shell structures are metastable. The structural integrity of these particles can thus be compromised at elevated temperatures due to the onset of diffusion, core migration towards the surface and alloying processes. It has become clear that knowledge about criteria of thermodynamic stability is essential for future applications.

In the course of this thesis bimetallic nanoparticles are synthesised and studied in numerous experiments. The particles are synthesized using the helium droplet technique, which provides an extraordinarily cold as well as interaction-free environment for the growth of onion-type nanostructures. A special focus was placed on Fe-/Co-/Ni-Au core-shell particles, as the large lattice mismatch between the magnetic materials and Au results in interesting behaviour at elevated temperatures due to the dominance of short range ordering effects. The particles are studied using time-of-flight mass spectrometry, transmission electron microscopy as well as X-ray absorption of fine structures. Their

thermally induced behaviour is observed and further studied via large scale force-field, molecular dynamics and cellular automaton calculations. Synergies between experimental measurements and theoretical models are exploited in order to investigate the origin of these phenomena and link them either to atomistic or bulk characteristics.

Kurzfassung

Bimetallische Systeme im Größenbereich weniger Nanometer haben aufgrund ihrer hohen Anzahl an Oberflächen- und Grenzflächenatomen sowie aufgrund gewisser synergetischer Effekte bei ausgewählten Materialkombinationen in den letzten Jahren erhöhtes Interesse erfahren. Ihre Eigenschaften können sich stark von den jeweiligen Festkörpereigenschaften unterscheiden, wodurch sich zahlreiche Anwendungsmöglichkeiten in Gebieten wie der heterogenen Katalyse, der Optik, Mikroelektronik oder der Biomedizin für diese Teilchen ergeben.

Im Unterschied zu Festkörpern kann in Nanopartikeln die Positionierung einzelner Atome die Stabilität und Anwendbarkeit dieser Teilchen entschiedend beeinflussen. Im Bereich magnetischer Teilchen ist besonders die Schalenstruktur eine interessante Konfiguration. Hier kann beispielsweise ein sonst oxidierendes magnetisches Material von einer Schutzschicht aus inerten Atomen umgeben sein. Damit wird einerseits verhindert, dass der magnetische Kern oxidiert und andererseits kann der sonst unter Umständen für biologische Systeme toxische Kern mit einer unbedenklicheren Schicht umgeben werden. Damit eignen sich diese Partikel auch für etwaige medizinische Anwendungen wie in der Krebstherapie. Allerdings sind die meisten bimetallischen Schalenstrukturen metastabil, weswegen ihre strukturelle Integrität bei erhöhten Temperaturen verloren geht. Information über thermische Stabilität ist daher essentiell für zukünftige Anwendungen.

In dieser Doktorarbeit wurden bimetallische Nanopartikel erzeugt und in zahlreichen Experimenten untersucht. Die Methode der Wahl war die sogenannte Helium-Tröpfchen-Strahl-Methode, welche eine extrem kalte und zugleich inerte Umgebung für die Synthese von Nanopartikeln in Zwiebelschalenstruktur darstellt. Besonderes Augenmerk wurde auf die Kombination von Fe, Co und Ni mit Au gelegt, da hier der erhöhte Gitterabstand interessante Verhaltensmuster der Partikel bei erhöhten Temperaturen induziert. Diese Phänomene entstehen durch den verstärkten Einfluss von kurzreichweitigen Wechselwirkungen im Unterschied zu Festkörpern. Mithilfe von Flugzeit-Massen-Spektrometrie,

Elektronenmikroskopie und Röntgen-Absorptionsspektroskopie wurden die Partikel untersucht und deren thermische Eigenschaften studiert. Die experimentelle Arbeit wurde ergänzt durch die Verwendung von zahlreichen computerbasierten Simulationen, welche einen Einblick in die beobachteten Prozesse lieferten.

Articles Related to this Work

1. **Synthesis of nanoparticles in helium droplets - a characterization comparing mass-spectra and electron microscopy data**
   Philipp Thaler, Alexander Volk, Daniel Knez, Florian Lackner, Georg Haberfehlner, Johannes Steurer, **Martin Schnedlitz** and Wolfgang E. Ernst
   J. Chem. Phys., **143(13)**, 134201 (2015)

2. **Thermally induced breakup of metallic nanowires: experiment and theory**
   Martin Schnedlitz, Maximilian Lasserus, Daniel Knez, Andreas W Hauser, Ferdinand Hofer and Wolfgang E Ernst
   Physical Chemistry Chemical Physics, **19 (14)**, 9402-9408 (2017)

3. **A coarse-grained Monte Carlo approach to diffusion processes in metallic nanoparticles**
   Andreas W Hauser, **Martin Schnedlitz** and Wolfgang E Ernst
   The European Physical Journal D, **71 (6)**, 150 (2017)

4. **Thermally induced alloying processes in a bimetallic system at the nanoscale: AgAu sub-5 nm core–shell particles studied at atomic resolution**
   Maximilian Lasserus, **Martin Schnedlitz**, Daniel Knez, Roman Messner, Alexander Schiffmann, Florian Lackner, Andreas W Hauser, Ferdinand Hofer and Wolfgang E Ernst
   Nanoscale, **10 (4)**, 2017-2024 (2018)

5. **Stability of core–shell nanoparticles for catalysis at elevated temperatures: Structural inversion in the Ni–Au system observed at atomic resolution**
   Martin Schnedlitz, Maximilian Lasserus, Ralf Meyer, Daniel Knez, Ferdinand Hofer, Wolfgang E Ernst and Andreas W Hauser
   Chemistry of Materials, **30 (3)**, 1113-1120 (2018)

6. **Spectroscopy of gold atoms and gold oligomers in helium nanodroplets**
   Roman Messner, Alexander Schiffmann, Johann V Pototschnig, Maximilian Lasserus, **Martin Schnedlitz**, Florian Lackner and Wolfgang E Ernst
   The Journal of chemical physics, **149 (2)**, 024305 (2018)

7. **Modelling electron beam induced dynamics in metallic nanoclusters**
   Daniel Knez, **Martin Schnedlitz**, Maximilian Lasserus, Alexander Schiffmann, Wolfgang E Ernst and Ferdinand Hofer
   Ultramicroscopy, **192**, 69-79 (2018)

8. **Vanadium (V) oxide clusters synthesized by sublimation from bulk under fully inert conditions**
   Maximilian Lasserus, **Martin Schnedlitz**, Roman Messner, Florian Lackner, Wolfgang E Ernst and Andreas W Hauser
   Chemical science, **10 (12)**, 3473-3480 (2019)

9. **On the passivation of iron particles at the nanoscale**
   Maximilian Lasserus, Daniel Knez, **Martin Schnedlitz**, Andreas W Hauser, Ferdinand Hofer and Wolfgang E Ernst
   Nanoscale Advances, **1 (6)**, 2276-2283 (2019)

10. **Synthesis of nanosized vanadium (v) oxide clusters below 10 nm**
    Maximilian Lasserus, Daniel Knez, Florian Lackner, **Martin Schnedlitz**, Roman Messner, Daniel Schennach, Gerald Kothleitner, Ferdinand Hofer, Andreas W Hauser and Wolfgang E Ernst

Physical Chemistry Chemical Physics, **21 (37)**, 21104-21108 (2019)

11. **Ultra-thin h-BN substrates for nanoscale plasmon spectroscopy**
Alexander Schiffmann, Daniel Knez, Florian Lackner, Maximilian Lasserus, Roman Messner, **Martin Schnedlitz**, Gerald Kothleitner, Ferdinand Hofer and Wolfgang E Ernst
Journal of Applied Physics, **125 (2)**, 023104 (2019)

12. **Helium nanodroplet assisted synthesis of bimetallic Ag@Au nanoparticles with tunable localized surface plasmon resonance**
Florian Lackner, Alexander Schiffmann, Maximillian Lasserus, Roman Messner, **Martin Schnedlitz**, Harald Fitzek, Peter Pölt, Daniel Knez, Gerald Kothleitner and Wolfgang E Ernst
The European Physical Journal D, **73 (5)**, 104 (2019)

13. **Effects of the Core Location on the Structural Stability of Ni–Au Core–Shell Nanoparticles**
Martin Schnedlitz, Ricardo Fernandez-Perea, Daniel Knez, Maximilian Lasserus, Alexander Schiffmann, Ferdinand Hofer, Andreas W Hauser, Maria Pilar de Lara-Castells and Wolfgang E Ernst
The Journal of Physical Chemistry C, **123 (32)**, 20037-20043 (2019)

14. **The impact of swift electrons on the segregation of Ni-Au nanoalloys**
Daniel Knez, **Martin Schnedlitz**, Maximilian Lasserus, Andreas W Hauser, Wolfgang E Ernst, Ferdinand Hofer and Gerald Kothleitner
Applied Physics Letters, **115 (12)**, 123103 (2019)

15. **Thermally induced diffusion and restructuring of iron triade (Fe, Co, Ni) nanoparticles passivated by several layers of gold**
Martin Schnedlitz, Daniel Knez, Maximilian Lasserus, Ferdinand Hofer, Ricardo Fernandez-Perea, Maria Pilar de Lara-Castells, Wolfgang E Ernst and Andreas W Hauser

Submitted, January 2020

Note: The articles (5), (13) and (15) are part of this work. The fundamentals of nanoparticle synthesis via helium droplets in article (1) are part of the PhD thesis of Philipp Thaler. Surface diffusion of nanowires at elevated temperatures (2, 3) are covered in the master's thesis of Martin Schnedlitz as well as the Habilitation of Andreas W. Hauser. A first study on the alloying of core-shell nanoparticles and studies on vanadium clusters relate to the articles (4), (8), (9) and (10) which are part of the PhD thesis of Maximilian Lasserus. The interested reader is referred to the PhD thesis of Roman Messner containing the article (6) about the spectroscopy of Au oligomers in helium droplets. A deeper insight into the impact of electron beam damage is found in the work of Daniel Knez referring to the articles (7) and (14). A more elaborate discussion of the nanoscale plasmonics can be found in articles (11) and (12), which are part of the PhD thesis of Alexander Schiffmann.

Contents

Chapter 1

Introduction

The great potential of miniaturization has triggered significant leaps in the advance of information technology since the 1960s. Gordon Moore already described in 1965 that the number of components in integrated circuits would double every year.[100] Not only did the amount of research in this field go skyrocketing, but nanotechnology had become such a dominant branch that it shaped the modern world in vast parts. Nanotechnology is nowadays not only limited to applications in information technology. There are numerous applications such as drug delivery,[127] cancer treatment,[35] small scale processors, lubricants, surface coatings, UV protection in sun creams or waterproof textile. Even nature has discovered and managed to enter the 'nanoworld' with self cleaning Lotus leaves or moth's eyes which can see in the night due to nanometre patterned receptors.

At the nanoscale, however, miniaturization and application development is not straight forward, as atomic properties start to interfere with bulk characteristics. This is not only challenging, but can also pave the way for synergistic effects. A great example is gold, which is considered a noble metal, but at the nanoscale gold turns out to become a very effective catalyst, which was first described by Valden *et al.* in 1998.[137] Furthermore, multicomponent nanoparticles or nanoalloys widen the possibilities, but at the cost of an increased complexity as composition and structure are adding additional parameters. The interplay between different species can though result in an even greater field of applications. This increase in complexity often overstretches the limits of exact quantum mechanical treatment. Therefore, experimental investigations are crucial as well as large scale computational approaches to fully understand the physical principles dominating the nanometre regime. For both monometallic and alloyed nanoparticles there are numerous synthesis techniques which can be divided broadly into two different classes: physical and chemical methods. The first one is free of any chemical reactions

in order to obtain nanoparticles, but only small quantities are produced. In the latter methods, a chemical reaction itself is responsible for producing the desired nanoparticles, often in larger quantities but at the cost of possible contaminations. The different methods as well as their benefits and drawbacks has been described in several review articles.[6, 37, 148, 149] The probably oldest but still used physical methods are mechanical techniques. Macroscopic particles are further fragmented into a small powder using a so-called ball mill.[22] This top-down approach has the advantage of being solvent-free and producing large quantities of nanoparticles larger than 10 nm. Formation in the gas phase is another widely used technique, also used in this thesis. Within this technique the desired metals are brought into gas phase inside a vacuum and further condensation results in the formation of nanoparticles. There are numerous ways to vaporize the desired metal species, ranging from evaporation in hot ovens, laser vaporization [97] to ion sputtering.[122] These techniques offer a high degree of interaction-free synthesis, but in contrast to other techniques only small quantities of clusters are produced. Aggregation and growth on a solid substrate is another very common technique in which single atoms or small clusters aggregate at the surface of a substrate and coalesce with other atoms previously deposited on the substrate.[110] The interactions between the deposited material with each other and the substrate as well as the deposition time determine the final form of the cluster. Wet-chemical methods on the other hand use solutions of the desired species which are mixed together. The size of the particles is adjusted by variation of the added reactants, the temperature of the solution as well as the addition of inert agents.[17] Afterwards, the particles are separated from the solution using centrifugation or evaporation. Wet-chemical methods can control very easily the composition of the particles as well as their size, but contaminations are often unavoidable. However, these techniques are often used in industrial applications as large quantities of clusters can be produced.

Within this thesis superfluid helium nanoparticles (more frequently referred to as helium droplets) are extensively used to synthesize (bi-)metallic nanoparticles in arbitrary combinations and compositions. This technique offers a fundamental advantage as it provides an ultracold, interaction free synthesis route in contrast to most other techniques mentioned above. Droplet size and pickup scheme determine the shape and core-shell(-shell) ordering of metallic clusters. Although the amount of clusters synthesized in a specific time is comparably small to other techniques, the pure, solvent-free way of synthesis is perfectly suited for fundamental research on mixed-metallic nanoparticles.

Remark: *In this thesis, 'nanoclusters' are referred to metallic compounds with sizes of a few nanometres. The term 'nanoparticle' is used more generally for every nanometre sized system. Due to their superfluid character He nanoparticles are referred to as 'nanodroplets' or only 'droplets' to clearly distinguish them from the metallic compounds synthesized within them.*

Similar to the experimental synthesis techniques there are numerous computational methods for the determination of energy landscapes, reaction dynamics, energetic minima search, etc. which can be divided in bottom-up and top-down approaches. Density functional theory (DFT) is one prominent example of a bottom-up ab initio approach which is used to calculate the energy of small systems (up to a few hundred atoms, see e.g. [89]). Larger systems are often described using a force-field ansatz in which the electronic interaction is modelled via a distance-dependent potential (see e.g. [106]). This is by orders of magnitude faster than DFT, with which larger nanometre sized systems can be calculated. However, the method relies on the quality of the interaction potentials. Molecular dynamics or Monte Carlo simulations are frequently used (see e.g. [84, 151] or [66])to model the dynamics at elevated temperatures, such as alloying or migration. For even larger systems cellular automata provide a scalable solution to describe dynamics on a grid via a set of physically motivated update rules. Especially for nanoalloys the CALculation of PHAse Diagrams (short CALPHAD [67]) is a widely used top-down technique to calculate the phase diagrams of metallic nanoparticles. [55, 75] It is based on a size-corrected calculation of phase diagrams via molar Gibbs free energies and is a very powerful tool to estimate the change of transition temperatures in finite sized systems. This method is reliable down to 10 nm, depending on the typ of system and the empirically determined Gibbs free energies.

In this thesis, the properties of nanoparticles and their relation to either bulk or atomic characteristics is studied. Initially, it started with a focus on the experimental investigation of (bi-)metallic nanoparticles, but over the course of the work, computational approaches became an evermore dominant part. Therefore, this work is not limited to either experimental observations or theoretical model description but rather tries to explain experimentally measured results with the help of different computational techniques.

This thesis is written in a cumulative manner. It is built around three peer-reviewed articles, where each one is printed in an individual chapter (see chapters 4-6). Except for different formatting, the articles are presented in the way they have been published. At the beginning of each chapter the contribution of each author is listed. The articles deal with the behaviour of bimetallic core-shell particles at elevated temperatures and aim to deepen the understanding of locally favourable configurations, restructuring processes as well as the impact of oxygen. The first article, "Thermally induced diffusion and restructuring of iron triade (Fe, Co, Ni) nanoparticles passivated by several layers of gold", describes the different restructuring processes from centralized Fe, Co and Ni core-clusters embedded in a Au matrix at elevated temperatures. The effect of decentralization and alloying is discussed and a theoretical explanation of the phenomena observed within the electron microscope is given. This article is followed by a more detailed study on the different intermixing processes of centralised and decentralised Ni-Au clusters "Effects of the Core Location on the Structural Stability of Ni–Au Core–Shell Nanoparticles". Large scale molecular dynamics simulations are combined with transmission electron microscopy scans at various temperatures. Finally, the effect of external factors on the restructuring processes is demonstrated in the last article "Stability of Core–Shell Nanoparticles for Catalysis at Elevated Temperatures: Structural Inversion in the Ni–Au System Observed at Atomic Resolution", which describes the phenomenon of a complete core-shell inversion triggered by the pure presence of oxygen.

Two introductive chapters are included, which are concerned with the experimental and theoretical basics and challenges of the related articles. Chapter 2 is devoted to the experimental part, where a short introduction about the helium synthesis is followed by how transmission electron microscopy as well as extended X-ray absorption fine structure is used to characterize the size, shape and properties of the metallic clusters. In contrast to previous works in this group, this chapter focuses on the link between the synthesis and more advanced observation techniques. The second introductory chapter focuses on the fundamentals of the applied computational techniques, where it lays out the benefits and limits of cellular automata, large scale molecular dynamic simulations and the calculation of phase diagrams. After the three main chapters, a short summary and overview is given at the end of the thesis, followed by an appendix which includes an extended section about transmission electron microscopy observations as well as explanatory input codes and printed files containing structural information.

Chapter 2

Experimental Setup and Methods

Starting with a general description of the synthesis of metallic nanoclusters via superfluid helium droplets, this chapter is devoted to the experimental part of this thesis. It lays out how metallic clusters are synthesized within the Helium environment for Nanoparticle Assembly (short HelENA) and which parameters influence the size, shape and composition of the particles. Furthermore, the in-chamber characterization tools are presented, which are used to monitor the synthesis and deposition of metallic clusters. The apparatus was constructed in September 2011, and the first experiments were performed after a two-year construction phase by Philipp Thaler and Alexander Volk. As it is typical for experimental setups, it has always been subjected to various extensions, add-ons and upgrades by several PhD and master students. A first manual was presented in the theses of Philipp Thaler [131] and Alexander Volk [139]which provide a convenient introduction to the whole apparatus and its application.

In this thesis, a focus is set on the conjunction between the He-droplet-mediated synthesis of metallic particles and their further investigation with other techniques. Therefore, this chapter will be covering three major parts, namely the helium mediated synthesis, the observation via electron microscopy, and the ongoing expansion of our experimental possibilities towards X-ray absorption near edge fine structure, short XAFS. Details of the He-droplet technique for the synthesis of metallic clusters are covered in Refs.[50, 132]

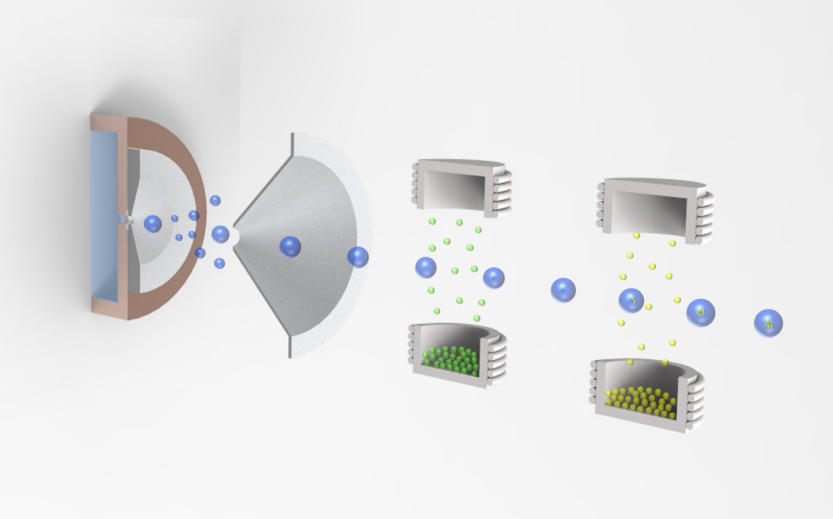

Figure 2.1: Sketch of the helium mediated synthesis of nanoclusters. The expansion of helium at cryogenic temperatures results in the formation of a beam of droplets which are used to pickup metal atoms. Those metal atoms agglomerate inside the beam, which results in the formation of clusters.

1 Helium Mediated Synthesis

The helium mediated synthesis of nanoclusters is based upon the outstanding properties of helium, which are utilized to create inert and nearly interactionless droplets, serving as 'nanolabs' for the synthesis of metallic nanoparticles. The expansion and further collimation of helium into a vacuum chamber results in the formation of a beam of helium droplets. Those droplets can be doped by arbitrary species of metal atoms which agglomerate to clusters inside the helium environment. Adding more pickup cells results in the formation of onion-type clusters. The order in which the droplets are doped is determined by their sequence of installation. A schematic of this technique is presented in Fig. 2.1.

1 .1 Helium and Helium Droplets

Helium is exceptional among all elements due to its unique properties. Its thermodynamic phase diagram shows that helium may never reach its solid phase at normal pressure independent of temperature and it also does not feature a triple point (equilibrium point of liquid, solid and gas phase). Instead, helium exhibits superfluidity below 2.17 K (see Fig. 2.2),[19] respectively 2.6 mK for ^{3}He. These effects are a consequence of the weak van der Waals interaction between individual atoms. A typical model employed

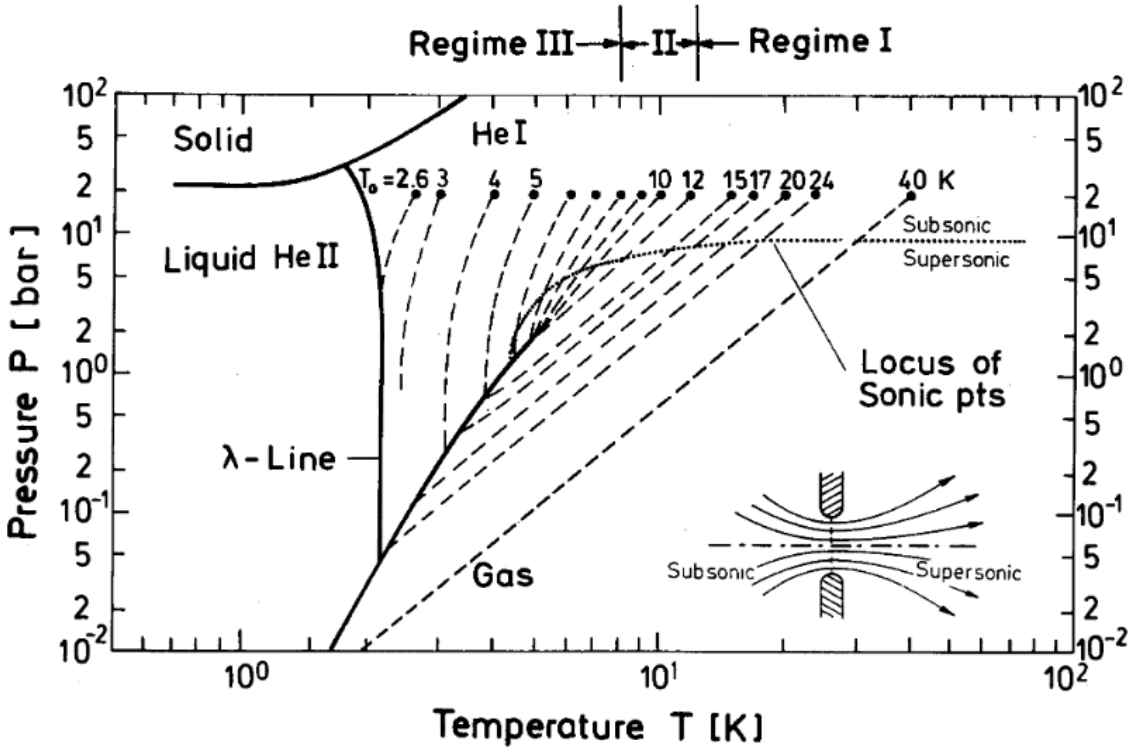

Figure 2.2: Phase diagram of ^{4}He, showing its four most prominent phases. Besides the gaseous and solid phase helium exhibits a transition from liquid He I to superfluid He II at temperatures below the λ-line. This graph depicts also the isentropes for supersonic and subsonic expansion through a nozzle. (Taken from [19])

is based on the Bose-Einstein condensation and describes the origin of superfluidity as a consequence of increased overlap of atomic wave functions at decreasing temperatures. The onset of superfluidity is denoted as the λ-line in the phase diagram. Below this line, He II represents the superfluid phase. Above the line, liquid He, referred to He I, represents the thermodynamically most stable phase. This unusual behaviour triggered intense studies on the superfluidity as well as on the behaviour and synthesis of helium clusters, which are referred in this thesis as helium droplets to distinguish them clearly from metallic nanoparticle clusters.

Helium Droplet Synthesis

A detailed understanding of the helium droplet synthesis which takes place during beam expansion is indispensable for a correct adjustment of the 'nanolab' size to be employed in

the subsequent synthesis of metallic clusters. By evaporation into vacuum, the droplets cool and reach a temperature of T ≈0.4 K.[21] Throughout this thesis, the droplets were synthesized using high purity grade 6 helium (99.9999% purity). The gaseous helium expanded through a 5 μm nozzle at a stagnation pressure of 20 bar into the first chamber. A variable nozzle temperature T_{CH} between 4 K and 12 K was used to adjust the droplet size. Below 7 K, quantum vortices are induced inside the helium droplet, which favour the growth of elongated metallic nanowires when doped with metal atoms. Spherical clusters, consisting of several thousand atoms, are best synthesized using an intermediate temperature T_{CH} between 7 K and 9 K in which vortices are not present. Three different regimes of helium expansion and further agglomeration of droplets are typically distinguished. For high temperatures the condensation out of gas phase occurs, for intermediate temperatures the fragmentation of a liquid is observed and for low temperatures Rayleigh breakup of a jet represents the dominating formation mechanism.[62, 71, 135]

1 .2 Synthesis of Metallic Clusters

Particles with sizes of a nanometres span the gap between atomistic and bulk characteristics. They have been studied with great interest to learn on the one hand about the link between atoms and solids and on the other hand to use them for potential applications in a variety of different fields, including bio-medical applications, [35, 92, 117, 125, 145] optics,[13, 64, 147, 156] heterogeneous catalysis,[20, 46, 143, 146] electrochemistry[126] and electronics.[126, 128]

The extremely low temperature of helium droplets and their superfluidity makes helium-mediated synthesis an interesting alternative to chemical growth. The droplets can pickup metal atoms, which are then located inside or outside the droplet. Typically, the actual behaviour is well described by the so-called Ancilotto-parameter.[9], which determines the relative stability of the surface and solvated states. Alkaline and alkaline-earth atoms usually favour to be placed on the droplets surface in contrast to other elements, which mainly agglomerate inside the droplet. The agglomeration of atoms inside a helium matrix does not only exclude any external interactions, but it also enables the possibility to synthesize onion-type structures with elemental and geometrical arrangements far from the global energetic minimum and protected from gas phase reactions. Finally, during the cluster growth the excess energy released from the formation of bonds

is dissipated via the evaporation of helium atoms.

The growth process was monitored using both a quadrupole mass spectrometer (Balzer QMA 200/ QME 200) as well as a quartz crystal scale, or microbalance. The first technique is ideal for measurements of the partial pressure of residual gases up to masses of 200 amu. Recording the partial pressure of helium provides information about the droplet size and attenuation as a function of T_{CH} and the metal atom doping rate. The latter technique determines the nanocluster deposition rate dm/dt as well as the total mass deposited as a function of deposition time $m(t)$. The quartz crystal is stimulated via an electric circuit and based on the relation between resonance frequency and deposited mass, it can measure deposition rates up to 1 pgcm^{-2}s^{-1}.

2 Transmission Electron Microscopy

It is crucial for the investigation of nanometre sized systems to use a technique which is capable to monitor their shape and local composition at various stages e.g. of a thermal treatment. A technique which is suited nearly ideally is transmission electron microscopy (TEM), which was used to characterize the thermally induced restructuring events of nanoparticles. A probe-corrected FEI Titan^3 G2 60-300 was used to record High Angular Annular Dark-Field (HAADF) images of the temperature-dependent diffusion and alloying processes. This electron microscope has a maximum resolution of 80 pm and is also equipped with composition sensitive sensors, namely a four-quadrant Energy-Dispersive X-ray spectroscopy detector (EDX, in German also referred as EDS) and a Gatan Quantum energy filter for Electron Energy Loss Spectroscopy (EELS). The liaison of all three techniques combines high resolution with information of spatial elemental distribution.

In order to investigate the nanoclusters and distinguish them from any support, it was essential to use TEM grids made up of ultra thin layers of either amorphous carbon or SiN (DENSsolutions Nano-Chip XT carbon and Ted Pella, Inc., Prod. No. 01824). Those materials show little interaction with the nanoclusters and support also high temperatures. The chip consists of a heating wire with small windows (size of a few μm), where the clusters can be monitored at various temperatures up to 1300°C. Due to the vanishingly small thickness the average temperature variation is smaller than 5%.
After nanocluster synthesis and subsequent deposition on TEM grids, they were trans-

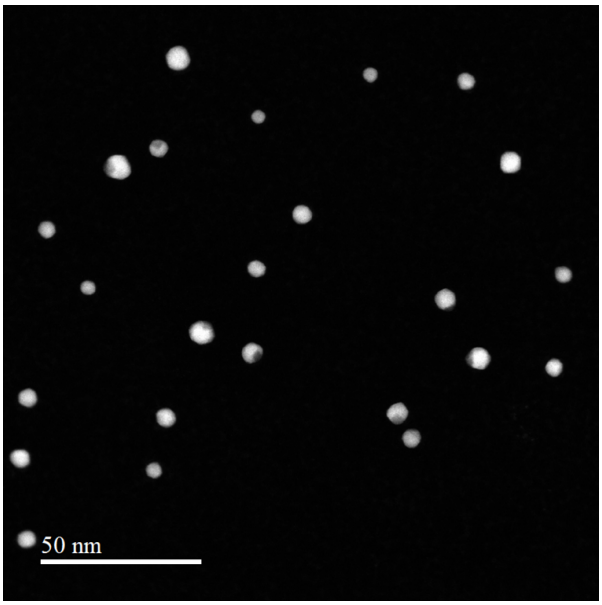

Figure 2.3: Exemplary overview of HAADF recording of Ni-Au clusters deposited on a SiN heatable TEM grid. Surface coverage Γ was choosen to be small in order to study the individual clusters separately from each other.

ferred to the electron microscope either at ambient conditions or immersed in liquid nitrogen. Transport at ambient conditions can be considered a first test of cluster stability outside of the ideal helium and in chamber UHV environment. Of all possible influences, oxidation is the most challenging, as several metals tend to oxidise as soon as the partial pressure of oxygen is high enough, resulting not only in the formation of metal-oxides, but also in possible overall structural changes.

In Fig. 2.3, an illustrative example of a HAADF recording is shown. The overall (surface) coverage of the grids Γ was chosen to be small enough to exclude any interactions between neighbouring clusters, but as large as possible to obtain meaningful statistics in a reasonable time. Therefore, it is important to understand the connection between the deposited mass per unit area m, respectively the deposition rate $\dot{m} = dm/dt$, and the total coverage Γ. During cluster deposition, the increase of $d\Gamma$ over time dt can be written according to Fick's second law as

$$\frac{d\Gamma}{dt} = \beta f(\Gamma), \tag{2.1}$$

where β is a fitting constant, describing the deposition rate coefficient, and $f(\Gamma)$ is a function acounting for the possible overlapping of clusters. In its simplest form it be-

comes the Langmuir blocking function of spherical particles $f(\Gamma) = 1 - \Gamma/\Gamma_0$,[3] which limits the coverage to be at maximum Γ_0.

To good approximation, the deposition rate $\dot{m}$ can be assumed to be constant during the TEM grid preparation. As a result, we can substitute $\Gamma(t)$ by $\Gamma(m)$. In addition, we have observed the partial coalescence of clusters in contact with each other, which can finally lead to a complete coverage with one monolayer of clusters. Putting all this assumptions together, we obtain

$$\Gamma(m) = 1 - e^{-bm}, \tag{2.2}$$

which describes a convergence towards a complete saturation with $\Gamma(m) = 1$, where the slope is determined via the fit parameter b. This expression is used to fit pairs of m and Γ for various experiments with different elements. The results are presented in Fig. 2.4, showing that the overall trend is following Eqn. 2.2. Larger deviations may stem from not perfectly aligned TEM grids during deposition (e.g. 04/12/2017) or from the formation of oxides which increase, a posteriori, the coverage (see results for Co).

The different slopes b_i for individual elements/elemental compositions are caused by the difference in the corresponding densities ρ_i, respectively atomic masses M_i. From the comparison between Ag-Au and Au a direct link between ρ_i and b_i can be found. Motivated by the expression of $\Gamma(m)$ in Eqn. 2.2, the product of b and m has to be constant when replacing the element i with element j ($M_i \rightarrow M_j$).

$$\rho_i \cdot b_i = \text{const} \approx 2490 \pm 60 \left[\text{m}^{-1}\right] \tag{2.3}$$

This value is determined with 95% confidence intervals. It is important to mention that there might be deviations for other elements due to oxidation or agglomeration effects. Therefore, Eqn. 2.3 only serves as a rule of thumb which can be improved if more data for different elements are taken into account. However, it is possible to estimate the time required to form a monolayer or multilayer of a certain species i, as $\Gamma(m)$ is in the first approximation linear proportional to $b \cdot m$. Given a deposition rate $\dot{m}_i$, the number of monolayers $N_{ML,i}$ for a species i is given by:

$$N_{\text{ML},i} = \frac{(2490 \pm 60)\,[\text{m}^{-1}]}{\rho_i \left[\frac{\text{g}}{\text{cm}^3}\right]} \dot{m} \left[\frac{\mu\text{g}}{\text{cm}^2\text{s}}\right] t\,[\text{s}] \cdot 10^{-3} \left[\frac{\text{g} \cdot \text{m}}{\mu\text{g} \cdot \text{cm}}\right]. \tag{2.4}$$

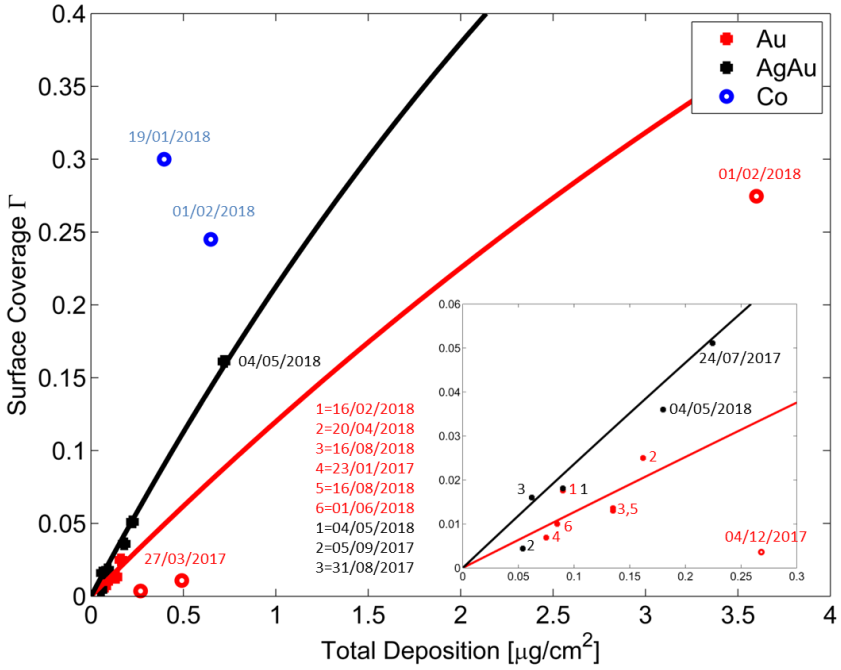

Figure 2.4: Overview of experiments connecting the total mass deposited with the surface coverage Γ. The total deposition was measured via the micro balance, the surface coverage is derived from HAADF scans in the transmission electron microscope. Red represents experiments containing Au particles or bimetallic particles with a large (>70%) fraction of Au atoms. Black outlines the same relation for Ag-Au core-shell particles and blue are two experiments with Co nanowires. In the lower right corner a detailed view on the region with low m and Γ is given.

According to Eqn. 2.2, only at infinitely large m a complete monolayer will be achieved. Therefore, when $N_{\mathrm{ML},i} = 1$ there has been sufficiently large deposition to form one layer of clusters, but some spots on the surface are free of clusters, whereas at other spots cluster stacking can be observed. Finally, for oxidizable species, the results from Eqn. 2.4 have to be customized to account for the element-specific increase in volume.

3 XAFS

Although transmission electron microscopy is a powerful tool for the investigation of nanoparticles it does have its caveats. On one hand, atomic resolution is ideal to investigate particle shapes, but it is always limited to its two-dimensional projection. On the other hand, the differences in Z-contrast from lighter core elements are at first glance

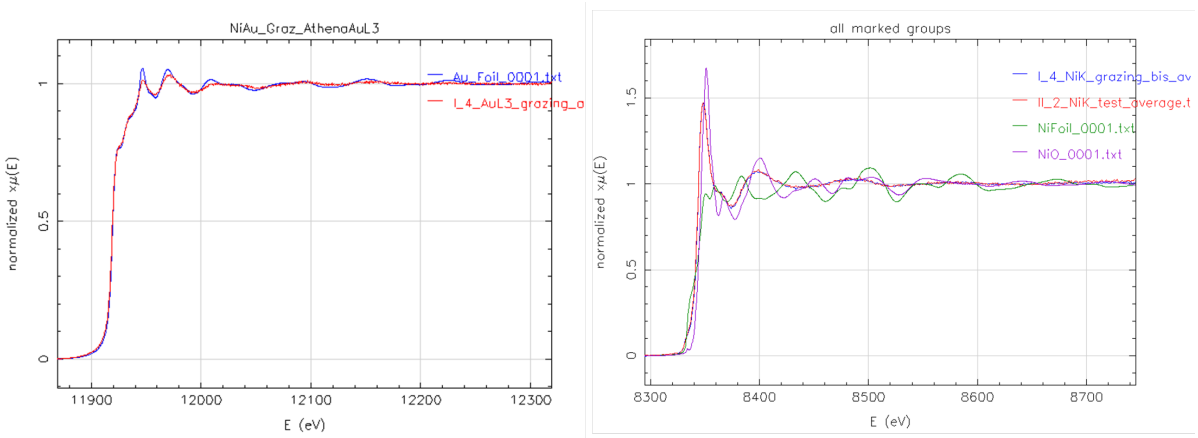

Figure 2.5: Preliminary XAFS measurements of Ni-Au nanoparticles. On the left hand side the fluorescence signal from Au-L_3 is plotted and compared to a signal from a Au foil. On the right hand side the Ni-K edge is plotted and compared to results from a Ni foil and Ni-oxide.

optimal to determine the elemental positioning, but any information about the structural arrangement of the inner atoms is suppressed by the larger signal stemming from the shell elements. Furthermore, it requires a long time to get sufficiently large statistics, as one single scan is taking approximately 30 seconds (20 nm×20 nm with 0.02 nm resolution).

An approach complementary to TEM is X-ray Absorption Fine Structure (XAFS). It uses the information about how x-rays are absorbed by atoms at energies close or above the core-level bond energy. The modulation of those energies depends on the actual elements, but also on its bonding situation in the local neighbourhood (i.e. its state of oxidation). The measurement of x-rays is straight forward, however, they require a large and energy-tunable source of x-rays is required. Therefore, these experiments have simultaneously evolved with the emergence of synchrotrons.

XAFS spectra (see Fig. 2.5)are typically divided into two regimes, Near-Edge Spectroscopy (XANES or NEXAFS) and Extended X-ray Absorption Fine Structure (EXAFS). NEXAFS signals are used to determine the coordination chemistry and from the EXAFS spectral information about the short range ordering is obtained. In Fig. 2.5 the NEXAFS signal for Ni-Au core-shell clusters show that close to the absorption edge one can already determine a possible oxidation of the particles when comparing the results to pure or oxidized samples. Rather challenging is the interpretation of the fine struc-

ture EXAFS, as more elaborate theoretical models have to be used to obtain information about the short range ordering from the form of the signal. In general, the first challenge is to isolate the signal from any instrumental or noise background. After a transformation of variables to wave numbers followed by a subsequent Fourier transformation, the typical radial dependence of the XAFS signal is obtained. This signal has a real as well as an imaginary part containing information on the local neighbourhood.

As this technique appears very promising, further investigations, beyond or complementary to TEM, are currently planned. At the writing time of this thesis (June 2020), first investigations of Ni-Au core-shell particles have been undertaken in cooperation with LCPMR ("Systèmes fortement corrélés - Matériaux magnétiques") at Sorbonne Université at the SOLEIL synchrotron in Paris. Ni-Au has been chosen in these studies as it is an intriguing system with large lattice mismatch between the two metals (13%). In ultrasmall phase-separated particles, the creation of an interface due to phase separation can thus give rise to a large increase of free energy due to deformation. Mixing of the species could be an efficient strategy to release strain.[25] In addition, the high temperature phase of Ni-Au has been predicted to display Short Range Ordering (SRO) tendencies,[86] indicating a possible additional impact of vibrational degrees of freedom on the phase diagram.

In this ongoing research project, we thus intend to gather data allowing an in-depth, atomic-scale understanding of the HRTEM measurements and MC simulations. The main goals of the project are to a) confirm the stability of the metallic Ni core with regard to oxidation, b) to analyse the segregation, mixing and possible high temperature SRO of the two metallic species as a function of temperature, c) to gain exhaustive information on the evolution of interatomic distances linked to local constraints, and finally d) to gain a better understanding of the vibrational properties of the present system.

Chapter 3

Theory and Simulations

The following section covers the computational methods used within this thesis in greater detail. The intention behind the computational approaches employed was to support and better understand the phenomena observed in the transmission electron microscopy experiments. Therefore, the first computations focused on the study of surface diffusion, namely the breakup of metallic nanowires which was described by the implementation of a cellular automaton. However, in the course of this PhD project the focus shifted slowly towards the prediction of thermally induced phenomena. This section follows the chronology of the performed simulations. It covers surface diffusion, molecular dynamics for large scale systems, and force-field predictions of structural stabilities. The last chapter is devoted to the prediction of phase diagrams with the so-called CALPHAD approach. It elaborates the usability as well as the limitations of thermodynamic approaches which are often seen as complementary to bottom-up techniques for the prediction of bimetallic nano phase diagrams.

1 Cellular Automata

Surface diffusion is a paradigmatic case of multi-scale dynamics. Although atomistic in essence, molecular dynamic approaches are only rarely used for the description of these phenomena since they emerge only in sufficiently large systems. There are numerous examples, such as surface wetting, capillarity, Rayleigh breakup, etc., which are usually described by continuous models. In a previous work, we tackled the problem of surface migration with simulations based on the Mullins equation.[140] This first approach aimed to simulate the thermally induced grooving at grain boundaries, however, on inconveniently fine discretization of time and the tendency towards instabilities at breakup events gave the motivation for the development of more advanced approaches. Such an

alternative approach of the simulation of diffusive behaviour can be employed by the usage of a cellular automaton (CA). The information obtained by the two-dimensional TEM data are converted into a three-dimensional reconstruction via a 3D logical grid. This way, the simulation takes the data observed via the electron microscope as a starting structure and tries to predict the thermally induced restructuring of the nanowires. The observed nanoparticles or nanowires are assumed to have a spherical cross section, which is an intrinsic feature of the growth process in helium droplets. At a TEM resolution of 0.95 nm, each element of the CA grid contains 40 atoms. On this set of descrete voxels, dynamics is now introduced by a set of update rules. For each time step the updates are simultaneously executed for all cells. The effect of thermally induced surface migration/diffusion is implemented via update rules based on the hopping probability of particles on the grid. These probabilities depend on the local neighbourhood of each cell. One has to first consider the stochastic character of diffusion, and second, to favour hoppings of voxels towards a cell containing an increased number of neighbours. Similar phenomena, e.g. reaction kinetics, are widely dealt with the usage of the Eyring[34] equation. In direct analogy, the jump or 'transition' rate of a voxel k can be defined as

$$k = \frac{k_B T}{h} \exp\left(-\frac{\Delta F\left(E_{\text{bond}}, d_{\text{bond}}, n\right)}{RT}\right) \tag{3.1}$$

where ΔF is the energy barrier to overcome, which is dependent on the number of neighbouring voxels n, the bond energy E_{bond} as well as the atomic bond distance d_{bond}. The reaction rate k is strongly dependent on the temperature T, which indicates that once a certain temperature is surpassed, surface migration is enabled. As soon as this temperature is reached, the voxel try to maximize the number of nearest neighbours (see Fig.3.1).

The overall trend of migration in a large scale system such as a nanowire is to reduce the number of surface voxels. However, as soon as one dimension becomes much larger than the others (the wire is about 10 times as long as it is thick), it is likely that patternization occurs, which resembles the transition towards a local minimum. In a previous article of our group [119] the patternization of Cu, Ni, Au and Ag nanowires has been presented both experimentally and with a cellular automaton. In Fig. 3.2, a direct comparison between the experimentally observed breakups and the prediction of evolution from the CA is shown. Not only does the CA correctly predict the final configuration of the nanowire, it also reproduces the correct series and location of breakup events.

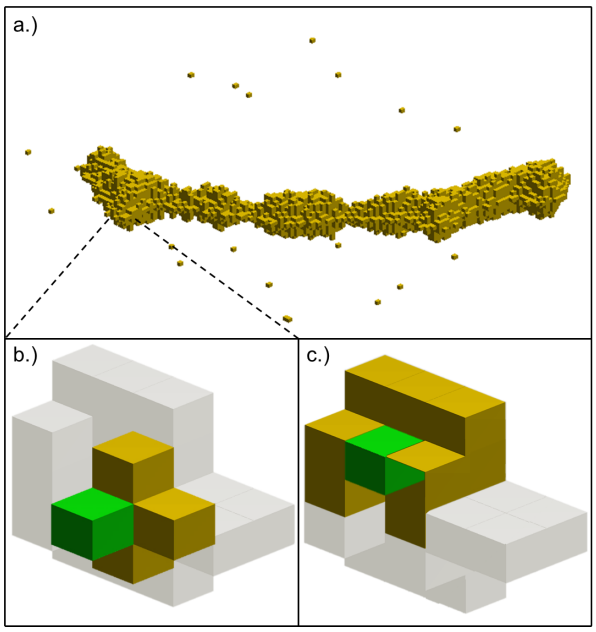

Figure 3.1: Basic principle of the CA approach, showing an example transition of a voxel (green) from its previous neighbourhood (b) towards a cell containing a larger number of voxels in its local neighbourhood (c). An overview of the nanowire as a whole is given in (a).

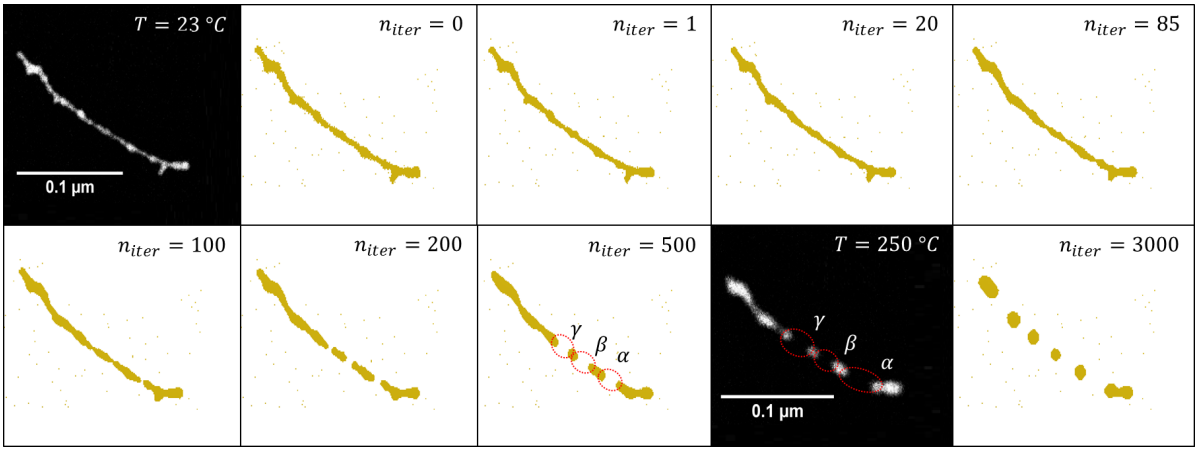

Figure 3.2: Breakup of a Au nanowire at elevated temperatures. The starting geometry at 23°C is used for the initial seed of the CA. After 500 iterations, the CA resembles the experimentally observed breakup points in the correct order (α first, β second and γ third). Furthermore, the CA provides an estimate of the subsequent structural evolution.

The phenoma observed here are not only limited to nanowires. In fact, it is typical

for a particle of any shape to reduce the number of surface atoms, resulting in the formation of spherical structures. In a spherical geometry the number of surface atoms to the number of total atoms is at a minimum. In contrast to atomistic techniques, the migration dynamics of very large systems can be calculated using a CA. A more elaborated discussion on CAs can be found in Refs.[59, 119]

2 Molecular Dynamics Simulations

In the thermally induced diffusion studies it became obvious that localized, atomic features can dictate the overall diffusive behaviour of nanoparticles. For Fe, Co and Ni embedded in a Au shell, a geometry featuring a de-centralized cores show larger thermal stability than its centralized counterpart. This fascinating phenomenon of localized motivated us to reproduce experimental observations with large-scale atomistic simulations relying on the embedded atom method (EAM) to describe interatomic interactions. All molecular dynamics simulations were performed using the LAMMPS (Large-scale Atomic/Molecular Massively Parallel Simulation) package.[112] Newton's equations of motion were solved through numerical integration via the velocity Verlet algorithm.[138]

On the computer, the nanoparticles are constructed in a way to mimic the helium-mediated synthesis in the experiments,[57, 60] leading to particles with geometries similar to experimentally obtained clusters. First, a core consisting of N atoms are allowed to fully relax, followed by the addition of M shell atoms which are again allowed to relax while keeping the position of the previously relaxed core atoms fixed. The relaxation processes start at temperatures close to the melting point and decrease down to 0.4 K. This stepwise coating procedure takes into account that during the synthesis inside a He droplet the core has been fully formed and occupies a minimum energy configuration at the point where the shell atoms are added.

Diffusion processes, and in particular diffusion processes for large system sizes, require often time scales exceeding computational capabilities. A possible solution is to further increase the simulation temperature in order to accelerate the diffusion processes. We found that for Ni-Au a simulation temperature of 900 K is already sufficient to study the nanoscale alloying of a solid cluster via MD simulations. Calculations for centralised as well as decentralised clusters were performed and are presented in greater detail in Chapter 5. It is found that, while a cluster with decentralized core has a higher overall

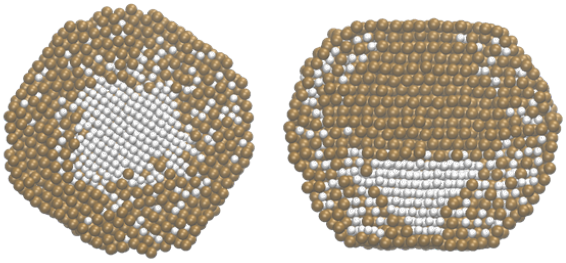

Figure 3.3: Large scale molecular dynamics simulation of two Ni-Au nanoparticles, one with a centralised core, the other with a decentralised core. Ni atoms are plotted in silver.

diffusion, a cluster featuring a centralised core exhibits a larger radial diffusion towards a fully intermixed state. An illustration showing the diffusive behaviour of a centralised an a decentralised cluster is depicted in Fig. 3.3.

3 Bimetallic phase diagrams via CALPHAD

Despite the same composition of elements, the behaviour of a macro-meter sized system to a system at the nanoscale may significantly differ. The fundamental reason for this difference is due to the large fraction of atoms placed at or close to the surface in a nanometre sized system. With decreasing size of a system the relative number of atoms at the surface increases evermore. For example, in a icosahedral structure the total number of atoms N as a function of the number of shells n is given by[91]

$$N(n) = \frac{10}{3}n^3 + 5n^2 + \frac{11}{3}n + 1. \tag{3.2}$$

Using this expression, the fraction α of surface atoms can be written as a function of the number of shells as:

$$\alpha(n) = \frac{N_{\text{surf}}}{N_{\text{tot}}} = \frac{N(n) - N(n-1)}{N(n)} = \frac{10n^2 + 2}{\frac{10}{3}n^3 + 5n^2 + \frac{11}{3}n + 1} \tag{3.3}$$

This indicates that for nanometre sized systems the fraction of surface atoms is relatively high even above 10 nm. In Fig. 3.4, which show the ratio α as a function of n, it is clearly visible that even with 20 shells the fraction of atoms located at an icosahedral surface is still 14%.

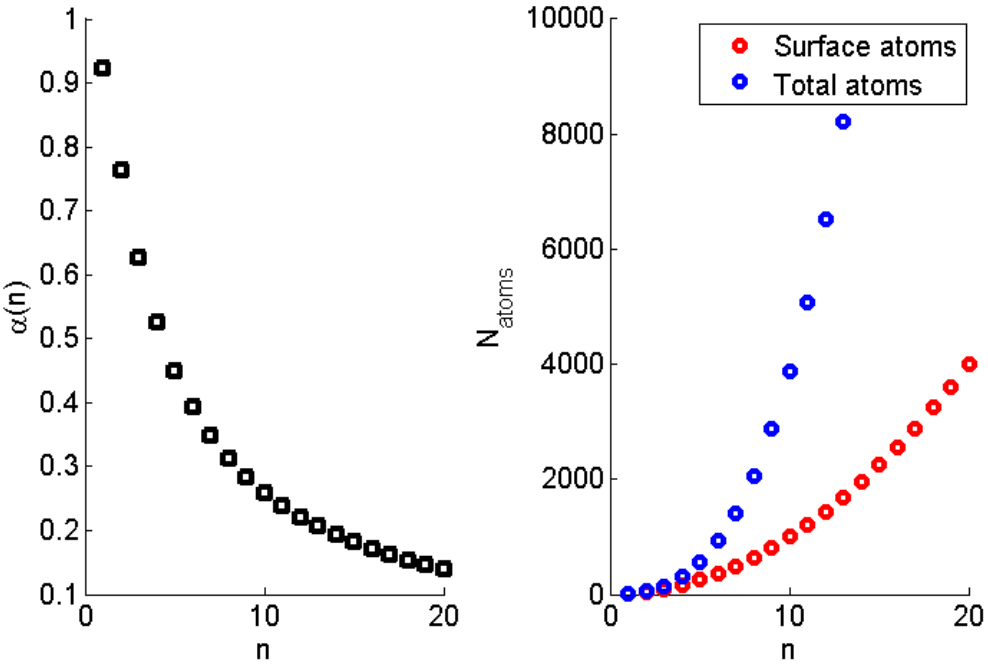

Figure 3.4: Left: Fraction of surface atoms $\alpha(n)$ as a function of the number of shells n. Right: Number of surface and total atoms also as a function of n.

A well-known top down approach to describe the characteristics as well as the miscibility of finite sized systems was found by Wang et al. in 2005 using a sized-corrected CALculation of PHAse Diagrams (CALPHAD).[144] This approach tries to correct the Gibbs energy of all phases by taking into account the number of surface atoms in relation to the total number of atoms. Therefore, the Gibbs energy is split into two parts,

$$G^{tot} = G^{\text{bulk}} + G^{\text{surface}}, \tag{3.4}$$

where G^{bulk} is the Gibbs energy of the bulk and G^{surface} is Gibbs energy stemming from the surface atoms. The latter one can be approximated by the surface energy of an isotropic spherical particle[124],

$$G^{\text{surface}} \propto \frac{\sigma V}{r}, \tag{3.5}$$

which is in good agreement with the inverse proportionality of $\alpha(n)$ with the number of atoms. σ represents the surface tension of the material, V the molar volume and r is the particles radius. Note that this approach is not only limited to one species of atoms,

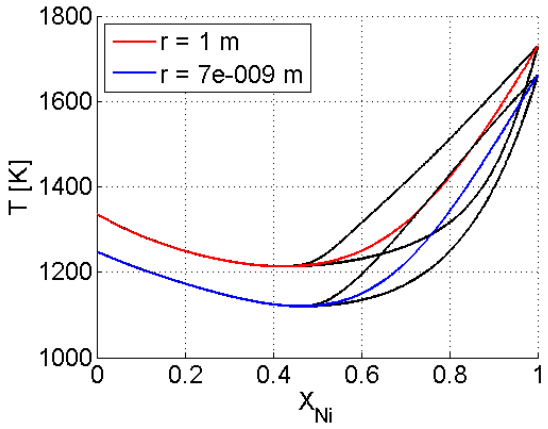

Figure 3.5: Solidus and liquidus line of the Ni-Au phase diagram for the bulk as well as a particle of the size of 7 nm. This diagram was created using the corrected CALPHAD method taking into account the finite size of the particle.

also binary systems and their corresponding phase diagrams can be calculated. For a binary system consisting of atoms of type A and B G^{bulk} can be written as

$$G^{\text{bulk}} = x_A G_A^0 + x_B G_B^0 + RT(x_A \log x_A + x_B \log x_B) + G^{ex}, \tag{3.6}$$

with x_A and x_B as molar fractions and G_A^0 and G_B^0 representing the standard Gibbs energies. G^{ex} is the excess Gibbs energy which is dependent on a parameter set empirically determined set of constants. Given the set of parameters for G^{ex}, it is possible to calculate phase transitions as well as whole phase diagrams for binary systems. The implementation of the $1/r$ correction results in the reduction of melting temperatures as well as phase transition temperatures. This correlates well with the experimentally determined increased mobility of finite systems (see also the following chapters). It is observed that nanometre sized systems start to alloy or melt at lower temperatures as their corresponding bulk counterparts. In Fig.3.5 a reduced melting temperature for the Ni-Au system is visible. This reduction is in agreement with the experiment. However, this approach gets less accurate the smaller the system becomes and below particles of an average size of 10 nm (radii below 5 nm) the $1/r$ approach underestimates the transition temperatures considerably. Therefore, it is recommended to use this approach only for particles with diameters larger than 10 nm. It is also important to mention that the general form and order of the phases are not changed, rather an overall decrease of transition temperatures is produced by this type of correction.

Chapter 4

Thermally induced diffusion of Fe-/Co-/Ni-Au core-shell particles

This chapter corresponds to the publication
"Thermally induced diffusion and restructuring of iron triade (Fe, Co, Ni) nanoparticles passivated by several layers of gold" by **Martin Schnedlitz**, Daniel Knez, Maximilian Lasserus, Ferdinand Hofer, Ricardo Fernandez-Perea, Maria Pilar de Lara-Castells, Wolfgang E. Ernst and Andreas W. Hauser, *submitted to the Journal of Physical Chemistry C*, (2020).

The author of this thesis was responsible for:

- performing the nanoparticle synthesis
- performing the MD simulations
- performing the force-field calculations
- evaluation of the results
- interpretation of the results
- author of the publication

The contributions of the co-authors are listed below:

- D. Knez: operating the transmission electron microscope and interpretation of the results

- M. Lasserus: assistance in the synthesis of the nanoparticles
- F. Hofer: microscopy supervision
- R. Fernandez-Perea: interpretation of the results and supporting information
- M. de Lara-Castells: interpretation of the results and supporting information
- W. E. Ernst: supervision, editing
- A. W. Hauser: supervision, editing, interpretation, funding

1 Abstract

The temperature-induced structural changes of Fe-, Co- and Ni-Au core-shell nanoparticles with diameters around 5 nm are studied via atomically resolved transmission electron microscopy. We observe structural transitions from local towards global energy minima induced by elevated temperatures. The experimental observations are accompanied by a computational modelling of all core-shell particles with either centralised or decentralised core positions. The embedded atom model is employed and further supported by density functional theory calculations. We provide a detailed comparison of vacancy formation energies obtained for all materials involved in order to explain the variations in the restructuring processes which we observe in temperature-programmed TEM studies of the particles.

2 Introduction

Bimetallic systems at the nanoscale have recently received increased attention as the combination of inter-metallic interactions and surface size effects can trigger unexpected physical behaviour and new phenomena. Potential applications cover a wide range of different fields, including bio-medical applications, [35, 92, 117, 125, 145] optics,[13, 64, 147, 156] heterogeneous catalysis,[20, 46, 143, 146] electrochemistry[126] and electronics.[126, 128] Additionally, magnetic core nanoparticles have been suggested for the activation of stem cells,[44, 93] as enhancers of supercapacitors[82] or for the optomagnetic finetuning of semiconductors.[42]

Due to their synergistic effects, bimetallic nanoparticles formed by a combination of magnetic and noble metals are particularly interesting for various physico-chemical ap-

plications such as bifunctional catalysis.[30, 45] Understanding the features of structural stability and metastability in local energetic minima within this novel class of materials would provide us with new possibilities in material design, but necessitates an adequate modelling of metallic interactions in large, yet finite systems where surface and interface effects play an equally important role as atomic diffusion.[40, 101] Metastable off-equilibrium structures are particularly strongly affected by thermal rearrangement processes such as surface diffusion, which makes them very interesting for the investigation of thermodynamically induced structural changes, but renders their behaviour also rather challenging to predict. Recently, the phenomenon of metastability in metallic nanowires has been addressed via cellular automata and molecular-dynamics simulations on a coarse grid.[59, 119] However, diffusion processes in mixed-metallic structures can not be treated on such a macroscopic level due to their intrinsic atomistic character. In this article, our experimental findings are therefore accompanied by atomic structure calculations, followed by a detailed investigation of vacancy formation energies in order to explain the striking structural differences observed in the experiment. In recent articles we have discussed the oxygen-induced rearrangement of centralised core-shell Ni-Au nanoparticles[80, 120], the oxidation of Ni-Au nanoparticles,[79] as well as the core location-dependent diffusion dynamics of Ni-Au nanoparticles at elevated temperatures[118]. The current extension of our ongoing work on bimetallic structures now focuses on the metastability of centralised magnetic cores embedded in a protective Au shell. Although Fe, Co and Ni are rather similar to each other in their interaction energies as well as their bond lengths, the slight deviations result in a substantially different thermodynamic behaviour.

This article is structured as follows. First, the experimental observations of restructuring of Fe/Co/Ni-Au core-shell clusters at elevated temperatures are presented. Then, vacancy formation energies are calculated from a force field approximation in order to gain insights into the various energy barriers which determine the processes of intermixing or structural rearrangement. For the sake of reliability, parts of our results are benchmarked against periodic electronic structure calculations employing density functional theory. Finally, we investigate the impact of temperature and entropy on the onset of restructuring via large-scale static calculations on a mixed-metallic system containing 6266 atoms at various levels of intermixing.

3 Material and Methods

3 .1 Nanoparticle Synthesis

The Fe/Co/Ni-Au core-shell particles are synthesised inside of droplets of superfluid helium, generated in a molecular beam setup which employs an adiabatic expansion of cooled helium into vacuum. The produced nanodroplets serve as 'nanolabs' which can be doped with the desired metals by a sequential pickup of metal atoms from the gas phase. A short summary of the process is provided below; for a more elaborate description of our setup we recommend reading of our previous publications on this subject.[132, 142]

High purity He (99.9999%) is expanded through a 5 ¯m nozzle at 7 K with a pressure of 20 bar into vacuum. A supersonic expansion process leads to the formation of He clusters with an average number of 10^7 He atoms and an internal temperature of 0.38 K, which are widely referred as He droplets due to their superfluid character.[136] After the formation, the droplets are exposed to a sequence of metal vapours generated by resistively heated 'pickup' cells. In the current setup, the first cell contains either Fe, Co or Ni, while the second cell is filled with Au. As a result, spherical Fe/Co/Ni core clusters are formed in the droplet which then get surrounded by a protective layer of Au. Although rather laborious and limited in the amount of produced material, this technique allows the convenient synthesis of any combination of core-shell or even onion-type structure. Particle sizes and stoichiometric ratios can be adjusted by simply varying the individual vapour pressures in the cells. Note, however, the stochastic character of the pickup process, which leads to an inevitable log-normal distribution of cluster sizes. For this experiment, an average diameter of $d = 6 \pm 2$ nm and a Fe/Co/Ni:Au ratio of 3:7 has been chosen in order to obtain perfect conditions for a complete coating of the Fe/Co/Ni core with a protective layer of Au. The release of binding energy during metal cluster formation results in the partial evaporation of the droplet. This loss of He can be measured via a residual gas analyser (Balzer QMA 200/QME 200) and allows the monitoring of the core-shell ratio. The doped He droplet beam is finally terminated on a heatable TEM grid (DENSsolutions Nano-Chip XT SiN). The clusters are deposited on suitable supports in a soft-landing process without significant structural changes, while the excess helium is vaporised upon impact.[4, 27, 38, 134]

3 .2 Electron Microscopy Characterization

A probe corrected FEI Titan^3 G2 60-300 is used to record high angle annular dark-field (HAADF) images of the temperature-induced restructuring processes *in situ*. Elemental analysis is provided by a four-quadrant EDX spectroscopy detector and a Gatan Quantum energy filter for electron energy loss spectroscopy (EELS). The *in situ* heating experiments are carried out in a DENSsolutions Wildfire D5 holder.

3 .3 Computational Modelling

Our experimental efforts are accompanied by computational studies employing the LAMMPS (Large-scale Atomic/Molecular Massively Parallel Simulation) package.[112] All pairwise intermetallic interactions (Fe/Co/Ni-Au) used in our theoretical studies are based on the embedded atom method (EAM).[155] It includes the pair energy between atoms i and j as well as contributions due to the embedding of each metal atom i into its local environment described by the electron density ρ_i. Therefore, it is expected to be more suitable for metal-compound formation as well as for the treatment of surface effects than other pairwise interatomic potentials.

In order to provide estimates of the vacancy energies we employ a periodic setup with supercells comprising $10\times10\times10$ *fcc* unit cells to investigate intermetallic diffusion in the bulk and $10\times10\times30$ *fcc* unit cells to study surface energies (i.e. including an extra layer of vacuum). The grids are relaxed before and after the formation of a vacancy with an energy threshold of 10^{-10} eV.

Periodic electronic structure calculations are performed with the Vienna *Ab initio* Simulation Package (`VASP` 5.4.4), [73, 74] following a similar computational approach to that reported in previous work on Ag_5-, and Cu_5-TiO_2(110) interactions.[28] Specifically, we employ a dispersion-corrected DFT-D3 *ansatz*,[53, 54] given its excellent performance in describing the adsorption of subnanometer silver and copper clusters on oxide surfaces.[28, 83] Structural optimizations and the calculation of interaction energies are carried out with the Perdew-Burke-Ernzerhof (PBE) density functional[108] and the Becke-Johnson (BJ) damping[54] for the D3 dispersion correction. Minor energy differences and the same trends were found when replacing the PBE functional by the PBEsol[109] counterpart in the DFT-D3 *ansatz*.
The bulk of the considered materials is modelled by employing supercells comprising

5×5×5 and 4×4×4 face-centered-cubic (*fcc*) unit cells of 500 and 256 atoms, respectively. The surface of the materials is simulated through the introduction of a vacuum region 4 times larger than the width of the 4×4×4 supercell, which effectively decouples the latter from interactions with periodic images in the direction perpendicular to the surface.

Electron-ion interactions are described by the projector augmented-wave method,[73, 94] using PAW-PBE pseudopotentials as implemented in the program. The electrons of the Fe($3d$,$4s$), Co($3d$,$4s$), Ni($3d$,$4s$), and Au($5d$,$6s$) are treated explicitly as valence electrons. A plane-wave basis set with a kinetic energy cutoff of 270 eV is used. The first-order Methfessel and Paxton scheme is employed to account for partial orbital occupations, with a smearing width of 0.2–0.5 (0.2) eV in energy calculations of the bulk (surface) of the considered materials. Within a testing window of the smearing width ranging from 0.2 to 0.5 eV the vacancy formation energies in bulk vary by 2% only. The Brillouin zone is sampled at the Γ point. Relative energies using a 2×2×2 Monkhorst-Pack[99] k-point mesh differed by less than 0.1 eV to those calculated at the Γ point. The convergence criterion is fixed to values from 10^{-4} to 10^{-6} eV for the self-consistent electronic minimization. Unless noted otherwise, all the atoms from the supercells are relaxed with a force threshold of 0.02 eV/Å. All calculations are spin-polarized.

The impact of intermixing on the Helmholtz free energy for the Ni-Au as well as the Co-Au system is determined by comparing a centralised with a decentralised core-shell *fcc* truncated octahedron containing 6266 atoms.[1] A core:shell ratio of 3:7 is chosen for the simulations, in accordance with the approximate mixing ratios in the experimental setup. The exchange of core and shell atoms is performed in steps of 50 atoms. After each step, the cluster is allowed to fully relax in order to obtain its minimum energy, and the total energy as a function of the number of exchanges is obtained. The number of particle exchanges can be further related to the entropy of the system. This way, estimates of the Helmholtz free energy at various temperatures are obtained, which can be used to study the onset of metallic intermixing.

4 Results and Discussion

We start with the presentation of our experimental findings regarding the structural behaviour of the core-shell clusters as observed during temperature-programmed treatments.

4 .1 Experimental Observations

Initially, all bimetallic clusters feature a fully centralised core-shell structure due to their identical synthesis as described in Section 3 . With a He nozzle temperature of 7 K, and an approximate metal gas vapour pressure between 10^{-6} mbar and 10^{-5} mbar, an average particle diameter of 6 ± 2 nm is obtained for all three core-shell systems.

A surface coverage of $1.1 \pm 0.2\%$ was chosen in order to avoid contact between individual clusters on the substrate. The temperature of the latter was increased in steps of 50°C, starting at room temperature, and HAADF images were taken at each step. To guarantee an oxygen-free restructuring process, EELS measurements are performed as well in order to check for traces of oxygen. In the following, the TEM observations of the three bimetallic systems are described in detail.

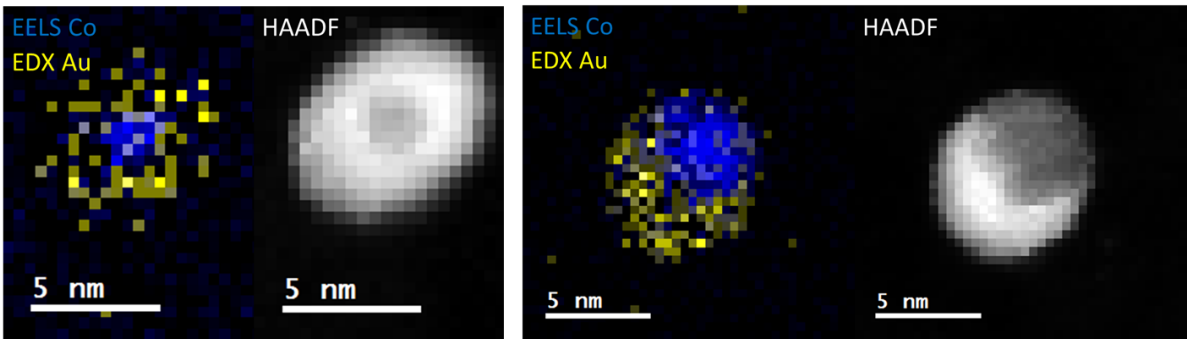

Figure 4.1: EELS Co observations and EDX Au observations as well as complementary HAADF scans of temperature induced structural transition from centralised (left) to decentralised (right) Co-Au clusters. The temperatures correspond to 25 °C (left) and 400 °C (right).

4 .1.1 Co-Au

Starting from a centralised core-shell configuration, Co-Au clusters undergo a transition towards a decentralised Co core underneath a single protective layer of Au at 400 °C. At this temperature, the surface mobility is high enough to enable the cluster to undergo a transition towards an energetically preferred configuration. This transition to a decentralised Co core has been predicted by Palomares *et al.*,[106] having its origin in the reduced overall stress inside the cluster, as originated from the lattice mismatch between layers of Co and Au. In Fig. 4.1, EELS, EDX elemental maps and HAADF recordings illustrate the transition from a centralised cluster towards a decentralised cluster at 400 °C. The Co core remains intact throughout the whole solid regime, without

any tendency towards alloying. This configuration is stable up to melting temperature (1100 °C). As soon as melting starts, the decentralised cluster undergoes a transition towards the mixed phase.

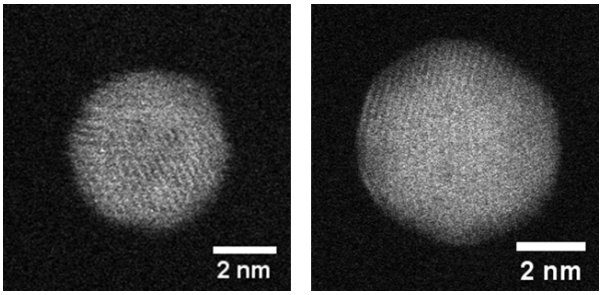

Figure 4.2: HAADF observation of temperature-induced rearrangements within a Fe-Au cluster. At 25 °C the cluster remains in its centralised state (left), whereas a temperature increase to 400 °C results in the rearrangement towards a fractured Fe core located underneath the Au surface.

4 .1.2 Fe-Au

The Fe-Au system behaves similarly to the Co-Au system in its preference for a decentralisation of the core as soon as atomic mobility becomes high enough. However, the process of decentralisation is rather different from the previous: At a temperature of 400 °C, the centralised Fe core fractures into several decentralised Fe pieces, but these fragments remain underneath one protective layer of Au (see Fig. 4.2). This remarkable behaviour makes the Fe-Au combination stand out among the three systems of this study. However, similar effects of an energetically preferred ring-like aggregation of material near the surface have been predicted for related systems (e.g. the Co/Ni-Ag system).[11]

4 .1.3 Ni-Au

In contrast to the decentralisation tendencies observed for Co-Au and Fe-Au, the Ni-Au system undergoes a phase transition towards full alloying even before reaching the melting temperature (see Fig. 4.3). The temperature regime for this transition seems to overlap with that corresponding to a transition towards a decentralised Ni-core. The latter structure has been found to be more stable.[118] Note that the formation of a Ni-Au alloy is in agreement with the phase diagram for the bulk material, which predicts an alloyed solid phase at temperatures above 300 °C. A transition from a centralised

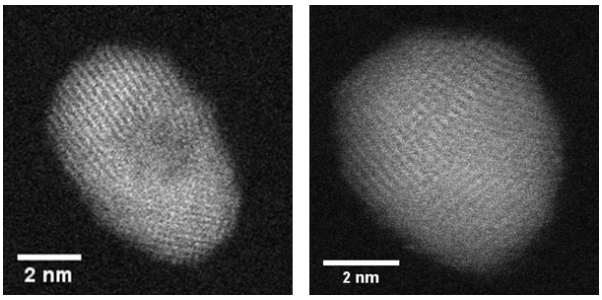

Figure 4.3: HAADF observation of temperature induced rearrangements within a Ni-Au cluster. The cluster is embedded centrally inside a Au shell. At 300 to 400 °C the Ni and Au atoms start to form an alloy, still exhibiting a lattice structure.

cluster towards a decentralised cluster at temperatures below the alloying threshold of 300−400 °C can only be observed if excess energy is introduced to the system via electron beam damage (see Ref. 69). We note further that an oxidation of Ni atoms can trigger core-shell inversions, as has been demonstrated in a recent article [120]. Therefore, the chosen heating ramps have to be fast enough to prevent any potential oxidation stemming from surface water presence below 400 °C.

4 .1.4 Similarities between the systems

Although in different ways, all three systems undergo a transition from their initial centralised core-shell arrangement towards an energetically more stable configuration at temperatures around 400 °C. Furthermore, it is found that for all three types of bimetallic nanoclusters the bulk phase diagram is correctly predicting whether alloying can occur or not. However, the actual temperature for such a phase transition is lower than predicted due to surface effects. This experimentally observed diversity of the various restructuring processes as described above is most likely related to differences in surface mobilities and interfacial energies.

4 .2 Diffusion and Intermixing via Vacancy Formation

As diffusion and intermixing are driven by the formation of vacancies in general, the energy necessary to form vacancies, E_f, is a key element to understand these differences in the experimental observations. An estimation of E_f is obtained from force field calculations with the `LAMMPS` programme package as described in Section 3 . E_f is obtained by comparing the energy of the full periodic supercell before (E_b) and after

(E_v) removal of one of its N atoms, according to[77]

$$E_f = E_v - \frac{N-1}{N} E_b. \tag{4.1}$$

The force field contains interaction energies only; therefore, cohesive energies E_c can be obtained by simply dividing the total energy of the slab by the number of atoms. Our results are summarized in Table 4.1. According to Ref. 95, vacancy formation energies are approximately proportional to their corresponding cohesive energies E_c, as expressed by the empirical relation $E_f = 1/3E_c$. However, the Fe/Co/Ni energies in our calculations show a diametrical behaviour, with Ni having the highest E_c and the lowest E_f in comparison to Co and Fe.

Table 4.1: Vacancy formation energies E_f and cohesive energies E_c for Au, Ni, Co and Fe, together with the energy differences when replacing an atom of type B (column) in a lattice of B atoms with an 'intruding' atom of type A (row).

E [eV]	Au	Ni	Co	Fe
E_f	1.01	1.70	1.83	1.95
E_c	3.93	4.45	4.40	4.20
Au_{int}	0.00	0.58	0.41	0.76
Ni_{int}	−0.52	0.00		
Co_{int}	−0.48		0.00	
Fe_{int}	−1.06			0.00

Table 4.1 reveals that E_f as well as E_c are the lowest for Au by far, which indicates that vacancies in gold are formed first upon heating. From this follows that, while the core is still free of vacancies, the shell is already affected by structural changes via the migration of vacancies. As soon as vacancies start to appear in the core, the Au atoms diffuse into the core region as well, leading to the onset of intermixing. When comparing the vacancy energies among the iron triade, it can be seen that E_f is smallest for Ni, followed by Co and Fe. This energetic comparison implies that Au can intermix with Ni at lower temperatures, while higher temperatures are needed for Co and Fe, respectively. Depending on the particle size, the necessary temperature might already exceed the actual melting temperature of the system.

Table 4.1 also contains the exchange energies for atomic replacements in the bulk, i.e. for the replacement of atom B from a lattice of type B atoms (element in column) with an atom of type A (element in row). For clarity, the 'intruding' atom is denoted by a subscript 'int'. When comparing Co and Fe, Co has not only a higher E_c, but also a less

favourable exchange energy when placed within a lattice of Au atoms. These findings agree with the experimental observation of a much higher core stability in the case of Co.

4 .2.1 Surface Vacancy Formation

Of further interest is the dependence of the vacancy formation energy on the actual position of the vacancy. Obviously, the effort to create such a defect is minimal on the surface. Even at interfaces, the emergence of vacancies is more likely at places with a large lattice mismatch or sufficient 'room' between the two metals. Therefore, surface vacancies can be considered as estimates for neutral comparisons between the various systems. We note that an actual calculation of interface energies is possible, but extremely tedious due to the many possibilities created by lattice mismatch and the many combinations of Miller indices. Even if available, the final effect would be an average of all of these, but mostly dictated by low-energy processes, i.e. those closest to the surface vacancy formation energies.

The determination of the corresponding energy, $E_{f,s}$, is carried out in the same manner as mentioned above, but with the restriction that the removed element must stem from the surface layer of the material. This energy is then used to calculate the vacancy formation energy according to Eq. 4.1. We use the same number of *fcc* unit cells as for the studies on intermetallic vacancies, but assume periodicity only in the x and y dimension. This is achieved by an extension of the unit cell in the z direction by an additional vacuum layer comprising the volume of $10\times10\times20$ *fcc* unit cells, resulting in a total supercell size of $10\times10\times30$ unit cells. The largest relative reduction in comparison to the bulk vacancy, $E_{f,s}/E_f$, appears for Fe (reduced by 76 %), followed by Co and Ni with almost identical ratios (reduced by 66 %), and Au (reduced by 56 %). This pronounced compliance of Fe to accept surface defects and restructuring is particularly interesting in the light of the experimentally observed core fragmentation which occurs for the Fe-Au system only. Together with the results for atomic exchange energies obtained in the previous section, the energy ratios $E_{f,s}/E_f$ also provide an explanation to why the Co core remains intact in the heating experiment and migrates towards a subsurface position.

We further extend this analysis of vacancy formation energies to the two subsurface layers in order to investigate the impact of finiteness also in the underlying layers of a given material. The results are summarised in Table 4.2. For Ni, Co and Fe, the creation of vacancies in the first or the second layer below the surface is already fully equivalent

Table 4.2: Absolute and relative vacancy formation energies at the surface and the first two sub-surface layers of Au, Ni, Co and Fe, calculated at the EAM level of theory.

	Au	Ni	Co	Fe
$E_{f,s}$ [eV]	0.44	0.57	0.61	0.47
$E_{f,s}/E_f$	0.44	0.34	0.34	0.24
$E_{f,s-1}/E_f$	0.80	1.00	1.00	1.04
$E_{f,s-2}/E_f$	1.00	1.00	1.00	1.04

Table 4.3: Vacancy formation E_f energies for Au, Ni, Co and Fe, obtained with density functional theory, evaluated for the bulk and for the surface.

E	Au	Ni	Co	Fe
E_f [eV]	0.67	1.63	2.26	2.02
$E_{f,s}$ [eV]	0.52	0.89	1.13	0.62
$E_{f,s}/E_f$	0.78	0.55	0.50	0.31

to a vacancy creation in the bulk (i.e. the energy differences lie below the accuracy of the method). However, for Au, an intermediate value between bulk and surface energy is obtained for the first subsurface layer, which suggests an increased mobility of vacancies also in the vicinity of surfaces and interfaces. Regarding the vacancy formation energies on the surface, it is interesting to see that the same relative energies $E_{f,s}/E_f$ are obtained for Ni and Co, while an even smaller value is obtained for Fe.

4 .2.2 DFT Results for Bulk Vacancies

In this section we provide complementary periodic density functional theory calculations of the vacancy formation energies, starting with the results for the bulk materials, and presented in a similar fashion as for the EAM approach discussed above. Note that these results are obtained at a higher level of theory, but for smaller (4×4×4) fcc supercells due to the otherwise too high computational effort. Our results are summarised in Table 4.3.

The estimated vacancy formation energies agree well with recently reported DFT-based values[152]. When compared to our results obtained at the EAM level of theory, we find reasonable agreement for the formation energies of Fe, Co, and Ni, which are reproduced in the same energetic order and with relative deviations of less than 10 % on average. However, for Au a larger deviation is noticeable. We note that even larger deviations between EAM and DFT occur if the inclusion of dispersion correction in the last steps of the DFT geometry relaxation (which is our standard approach throughout

the article) is skipped. A tentative increase to (5×5×5) supercells yields differences in the range of 10 % percent, indicating an acceptable remaining slab size effect.

Atomic exchange energies have been recalculated with DFT as well, but are less straight forward to compare since DFT energies are absolute energies, which has to be taken into consideration when taking differences before and after the insertion of atom A in lattice of atoms B. Using single atom energies obtained with the same method and slab size, and employing the formula

$$\Delta E = E_{\mathrm{A\,in\,B\,slab}} + E_{\mathrm{B\,atom}} - E_{\mathrm{B\,slab}} - E_{\mathrm{A\,atom}} \tag{4.2}$$

to calculate the exchange energies, the overall tendencies of the EAM table are confirmed, but the values are off by a factor 3 on average, even if the slab size is increased to $5 \times 5 \times 5$, and differences in the detailed energetic order become apparent. In particular, the insertion of the large Au atom into a smaller lattice is prone to bias due to the computationally inevitable slab size limitations, and is much more problematic than the formation of vacancies in a finite slab of feasible size.

4 .2.3 DFT-based Surface Vacancy Formation Energies

We also revisit the surface vacancy formation energies at the DFT level of theory.[2] Our results have been added to Table 4.3.

As reported in Ref. 32 for vacancies at the surfaces of *fcc* Au and Ni surfaces [(111), (100), and (110) facets], the vacancy formation energies at the first layer lie below 1 eV. Specifically, values between 0.15 [(110) facet] and 0.54 eV [(111) facet] have been reported for iron surfaces, while for nickel values between 0.34 ([110] facet) and 0.82 eV ([111] facet) can be found in the literature.[32] We notice that the magnitude of the dispersion-free DFT E_f value for the Fe(001) surface (0.72 eV) is close to that reported in Ref. 23 (0.9 eV). For cobalt, the dispersion-corrected vacancy formation energy in the first layer (1.13 eV) is slightly smaller than reported in Ref. 81 (1.4 eV).

In agreement with the EAM calculations, the formation of surface vacancies requires much less energy than in the bulk, in particular for Fe. The same holds true when analysing the dependence of the vacancy formation energy on the layer position for Au and Ni.

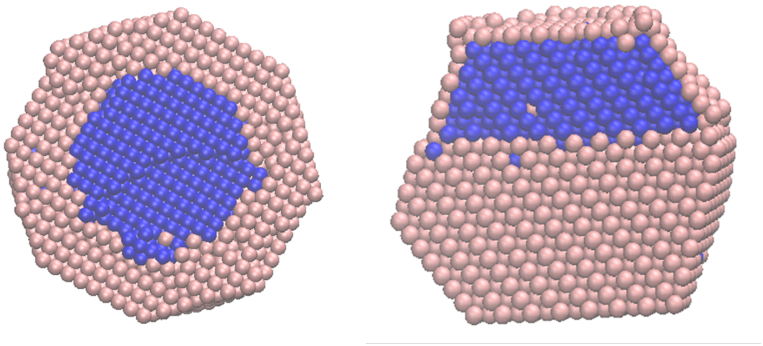

Figure 4.4: Cuts through the atomic models of a centralised and a decentralised Ni-Au cluster after the first intermixing step (comprising 50 swaps between core and shell atoms).

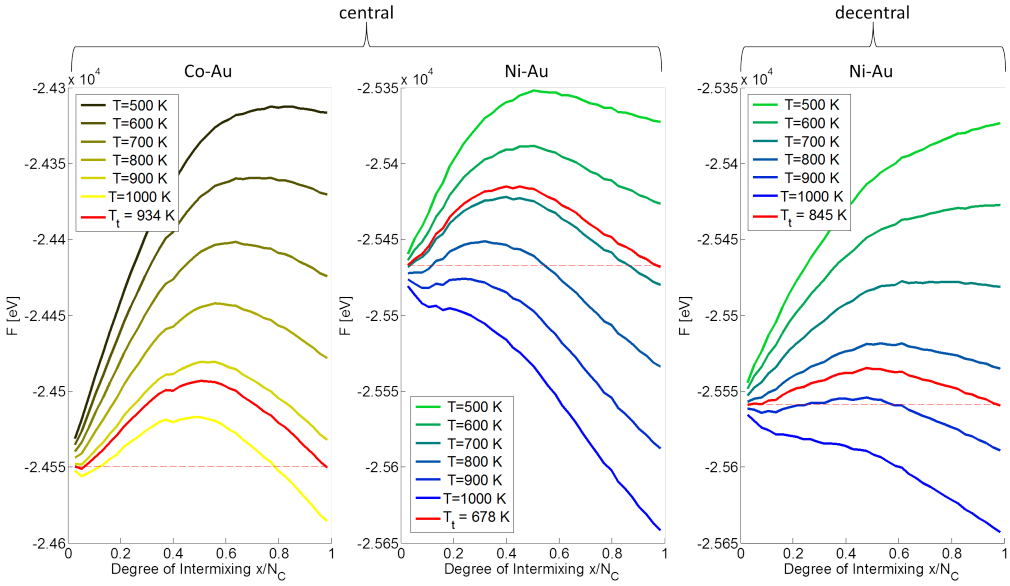

Figure 4.5: Helmholtz free energies of three bimetallic clusters, plotted as a function of the relative intermixing x/N_{C}. Zero mixing corresponds to a perfect core-shell structure with a minimum of intermetallic bonds. Left: Co-Au cluster with centralised Co core. Center: Ni-Au cluster with centralised Ni cluster. Right: Ni-Au cluster with decentralised Ni cluster. Intermixed phases become favourable at 914 K, 662 K and 830 K, respectively (red curves). Note the slightly increased resistance against mixing in case of a decentralised core positioning for Ni-Au.

4 .3 Computational intermixing

The comparison of vacancy energies provides only limited information on diffusion tendencies. Therefore, we extend our computational investigation towards the inclusion of entropy effects to obtain estimates of the Helmholtz free energy as a function of the temperature. This way, it should be possible to predict the energetically preferred structural arrangement of each bimetallic nanoparticle at a given temperature in the experiment. At zero Kelvin we find that a decentralised core is the energetically most favourable configuration for the Co-Au and Ni-Au systems. However, for Fe-Au we do not see a significant energy difference between a centralised and a fully decentralised core, which might be due to a more favourable fractured decentralised core. The impact of temperature is modelled as follows.

Starting from centralised as well as decentralised core-shell structures for the Fe-, Co- or Ni-Au systems, we perform a series of exchanges between atoms of the core region with Au atoms of the surrounding Au shell, allowing a stepwise increase of the mixing entropy with each exchange of two atoms. A truncated octahedron *fcc* cluster, containing 6266 atoms in total and a core:shell atomic ratio of 3:7, is adopted in the simulations, which corresponds to $N_C = 1880$ core and $N_S = 4386$ shell atoms. The exchanges are performed in steps comprising 50 swaps of atomic positions. Each of these steps (50 swaps in the first, 100 in the second and so on) is repeated 150 times and the mean value of the energy E is calculated. As an example, the structures of a centralised and de-centralised Co-Au cluster after the first 50 atomic swaps are depicted in Figure 4.4. At each step, the Helmholtz free energy is obtained via

$$F(x,T) = E(x) - T \cdot S_{\mathrm{mix}}(x), \tag{4.3}$$

with $E(x)$ as the inner energy at 0 K and $S_{\mathrm{mix}}(x)$ as the mixing entropy, both written as a function of the degree of mixing, expressed by x, the number of 'mobilized' core atoms. With this term we refer to a subgroup of core atoms which are allowed to be placed anywhere in the cluster (including shell as well as core positions, except for those core places occupied by the $N_{\mathrm{C}} - x$ yet 'immobilized' core atoms). In each exchange step, x core atoms change places with any of the allowed atoms, followed by a relaxation of the whole system. We obtain the following expression for the mixing entropy as a function of x:

$$S_{\mathrm{mix}}(x,N_{\mathrm{S}},N_{\mathrm{C}}) = \mathrm{k_B} \ln \left[\sum_{j=0}^{x} \binom{N_{\mathrm{S}}}{j} \binom{N_{\mathrm{C}}}{j} \right] \tag{4.4}$$

In this formula, j is denoting the number of core atoms which have swapped their position with shell atoms, which is obviously identical with the number of shell atoms now placed inside the core, and $\mathrm{k_B}$ as the Boltzmann constant. Note the difference between j and x in this context: j goes from 0 to x in a summation over products of binomial coefficients, yielding the correct number of possible structures for the current state of intermixing described by x. This allows us to calculate the impact of entropy effects for each starting geometry. For $x \to N_{\mathrm{C}}$, this expression converges towards

$$S_{\mathrm{max}}(N_{\mathrm{C}},N_{\mathrm{S}},N_{\mathrm{C}}) = \mathrm{k_B} \ln \left[\binom{N_{\mathrm{S}}+N_{\mathrm{C}}}{N_{\mathrm{C}}} \right], \tag{4.5}$$

which can be proven by Vandermonde's theorem. In this case, the maximum number of possible mixing states is obtained since all intermixing constraints are removed.

Using the expression for S_{mix} of Equation 4.4, we can calculate the Helmholtz free energy at various temperatures for all partially intermixed states. We note that our approach is neglecting vibrational contributions to the entropy, but their influence is known to be marginal[106]. For graphical illustration, it is most convenient to plot the Helmholtz free energy as a function of x/N_c. This way, a relative degree of intermixing is obtained for the x-axis, with values between 0 (corresponding to a perfect core-shell structure) and 1 (corresponding to a fully mixed structure). As can be seen in Fig. 4.5, the formation of an alloy in the Ni-Au system, starting from a centralised Ni core, becomes feasible at a temperature of 662 K. This value can be derived from the figure by observing the temperature at which the free energy value for an intermixed geometry (right end of each curve) becomes lower than the value for an unmixed core-shell geometry (left end of the curve). This is indicated by a dashed horizontal line for the red curve belonging to the threshold temperature. The value obtained for Ni-Au is in good agreement with the experimentally determined intermixing temperature of 570...670 K (300...400°C).It indicates that intermixing via Ni mobility is taking place even in the solid phase, as it is predicted by the bimetallic phase diagram for bulk Ni-Au. In contrast, a centralised Co core (left panel of Figure 4.5) is stable up to a temperature of 914 K, which lies above the experimentally observed temperature (670 K) for core migration from a centralised to a decentralised position. Co and Fe do not undergo a transition towards an intermixed cluster, as predicted by their corresponding phase diagrams (Co-Au[103],

Fe-Au[104]), which is due to the energetically more favourable unmixed configuration. Restructuring of the bimetallic cluster is enabled by the increased mobility of surface atoms, as described in Section 4 .2. Furthermore, it is found that a decentralised core (right graph in Fig. 4.5) requires even higher temperatures for intermixing than a centralised core. This confirms the findings of our previous study[118] that a decentralised Ni core requires more energy to form an alloy than a centralised Ni core. We note that a similar graph for the Fe-Au system has been omitted here since its corresponding Helmholtz free energies are fully dominated by the energy contributions from increased intermixing. For the Fe-Au potential used in this study, the curves do not show a local minimum at the mixed state within the experimentally relevant range of temperatures.

5 Conclusions

Centralised Fe-Au, Co-Au and Ni-Au core-shell nanoparticles are synthesised in He nanodroplets and deposited on heatable TEM grids. We then study the structural stability of their cores, which are initially fully embedded in a protective outer layer of Au, via transmission electron microscopy while heating the support. We find that even though the three elements of the iron triade are only varying minimally in their respective cohesive energies and bond lengths, entirely different structural behaviour is observed upon thermal treatment. The interpretation of our experimental findings is supported by a theoretical comparison of vacancy energies at the EAM and the DFT level, calculated for the four metals, and by studies of Helmholtz free energies of the bimetallic systems at various degrees of intermixing.

The Co core shows a transition towards a decentralised position at 400°C, which we explain as the result of lattice strain reduction. The Fe core behaves in a similar way, but instead of remaining a single cohesive mass, it disintegrates into several fragments at 400°C, also located at decentralised positions. We attribute this behaviour to the reduced surface vacancy formation energy of Fe in comparison to Co. The Ni-Au cluster, on the other hand, undergoes a transition towards full intermixing already between 300°C and 400°C. Here, the smaller vacancy formation energy required for the formation of Ni vacancies enables Au atoms to migrate into the core at even lower temperatures than in the Fe-Au and Co-Au systems.

6 Acknowledgement

This research have been supported by the Austrian Science Fund (FWF) under Grants P 29893-N36 and FWF PIR8-N34, the Horizon 2020 research program of the European Union under Grant No. 823717-ESTEEM3, and the Spanish Agencia Estatal de Investigación (AEI) and the Fondo Europeo de Desarrollo Regional (FEDER, UE) under Grant No. MAT2016-75354-P. The authors would like to acknowledge the use of HPC resources provided by the ZID of Graz University of Technology and by the Vienna Scientific Cluster (VSC). Further support by NAWI Graz is gratefully acknowledged. The CESGA super-computer center (Spain) is also acknowledged for having provided computational resources.

Chapter 5

Effects of the Core Location on Structural Stability

This chapter corresponds to the publication
"Effects of the Core Location on the Structural Stability of Ni–Au Core–Shell Nanoparticles" by **Martin Schnedlitz**, Ricardo Fernandez-Perea, Daniel Knez, Maximilian Lasserus, Alexander Schiffmann, Ferdinand Hofer, Andreas W. Hauser, Maria Pilar de Lara-Castells and Wolfgang E. Ernst *Journal of Physical Chemistry C*, **123 (32)**, 20037-20043 (2019).

The author of this thesis was responsible for:

- performing the nanoparticle synthesis
- performing the MD simulations
- evaluation of the results
- interpretation of the results
- author of the publication

The contributions of the co-authors are listed below:

- R. Fernandez-Perea: developement of the MD code and interpretation of the results
- D. Knez: operating the transmission electron microscope and interpretation of the results

- M. Lasserus: assistance in the synthesis of the nanoparticles
- A. Schiffmann: assistance in the synthesis of the nanoparticles
- F. Hofer: microscopy supervision
- M. de Lara-Castells: idea and developement of the MD code
- A. W. Hauser: supervision, editing, interpretation, funding
- W. E. Ernst: supervision, editing

1 Abstract

Structural changes of Ni-Au core-shell nanoparticles with increasing temperature are studied at atomic resolution. The bimetallic clusters, synthesized in superfluid helium droplets, show a centralized Ni core, which is an intrinsic feature of the growth process inside helium. After deposition on SiN_x, the nanoparticles undergo a programmed temperature treatment in vacuum, combined with an *in situ* transmission electron microscopy study of structural changes. We observe not only full alloying far below the actual melting temperature, but also a significantly higher stability of core-shell structures with de-centralized Ni cores. Explanations are provided by large-scale molecular dynamics simulations on model structures consisting of up to 3000 metal atoms. Two entirely different diffusion processes can be identified for both types of core-shell structures, strikingly illustrating how localized, atomic features can still dictate the overall behaviour of a nanometer-sized particle.

2 Introduction

Bimetallic systems at the nanoscale have recently received increased attention as the combination of inter-metallic interactions and surface size effects can trigger unexpected physical behaviour and new phenomena (see, e.g., Ref. 47 for a recent review). Potential applications cover a wide range of different fields, including bio-medical applications,[35, 92, 117, 125, 145] optics,[13, 64, 147, 156] heterogeneous catalysis,[20, 46, 143, 146] electrochemistry[126] and electronics.[126, 128] Additionally, magnetic core nanoparticles have been suggested for the activation of stem cells,[44, 93] as enhancers of supercapacitors[82] or for the optomagnetic finetuning of semiconductors.[42]

Bimetallic nanoparticles which combine magnetic and noble metals are particularly interesting for special physicochemical applications.[30] Our research on the Ni-Au system is partly motivated by the fact that optical, catalytic and photocatalytic properties of gold nanoparticles can be tuned via the insertion of a magnetic Ni core, e.g. for a magnetic-field-induced synthesis of wire-like structures.[72]. An additional handle on positional control could also become relevant for the 3D-printing of nanostructures.[36] Magnetic nanoparticles and external fields have further been used to target biomolecules, and multifunctional plasmonic-shell magnetic-core nanoparticles are being successfully applied for diagnosis, isolation, and photothermal destruction of cancer cells[35]. Sensitive sensing devices in human serum have been built using Ni-Au core-shell nanoparticles.[92]

However, the specific activity of a core-shell nanoparticle is related to the actual position of its core, and its structural integrity is compromised at elevated temperatures due to the onset of diffusion/alloying processes. Therefore, it is necessary to understand the correlation between the magnetic core location and the structural stability of the particle upon heating.

For the synthesis of nanoparticles a variety of methods are currently being exploited. Among them, wet chemistry methods are the most common, but also techniques such as laser ablation synthesis[7] are applied in some cases. An interesting alternative to these standard methods is the usage of superfluid helium nanodroplets as containers for a fully inert, controlled synthesis of mixed-metallic nanoparticles. This is achieved via a sequential pickup of metallic atoms by helium droplets created in the process of a supersonic expansion of helium through a cooled nozzle. Due to the extremely low helium temperature of 0.37 K[58] and the practically inert environment provided by the droplets it is possible to synthesize metallic nanoparticles with arbitrary core-shell or onion-type structures. The low temperature of the droplets even enables the synthesis of particles in metastable structures, as metallic systems can be trapped in the desired local minimum during growth. Recently, we took advantage of this feature and produced Ni-Au core-shell particles where the highly reactive Ni core is protected by a few layers of gold.[120] While this previous work had its focus set on the avoidance of Ni oxidation by a protective layer of gold, the current study investigates the structural behaviour of a bimetallic system at the nanoscale in greater detail.

We demonstrate that it is indeed possible to synthesize bimetallic nanoparticles in a local minimum structure, deposit them on a substrate, and watch their relaxation to the global minimum structure *in situ*. In terms of experimental effort, this objective is rather challenging: Any presence of oxygen during heating after deposition must be avoided at all cost as it would lead to an inevitable chemical reaction of diffusing Ni atoms with oxygen on the particle surface.[120] We will show that for Ni-Au core-shell particles in the nanometer range a fully centered position of the Ni core within a gold shell, a structure intrinsic to the pickup-mediated growth process inside the helium nanodroplets, will experience a faster transition towards a fully alloyed or mixed state than their decentralised counterparts. We also demonstrate that in contrast to surface studies of island growth at room temperature[111] the nanoparticles remain intact until the alloying temperature is reached.

Concerning the theoretical treatment of structural changes in nanoparticles two diametrically opposed approaches can be distinguished. One is to employ top down models

such as the CALPHAD method,[124] which extends well-known bulk models by additional surface terms in order to handle the increasingly important surface size effects emerging at small scales. Very recently, a bond-centric model has been developed specifically for the description of monometallic and bimetallic nanoparticles, addressing the energetics in massive nanoalloy structures.[150] The alternative are bottom-up approaches, which aim for a basic understanding at the atomic level via molecular dynamics (MD) simulations.[15, 39, 76, 106, 114] In this article, we employ a force field-based bottom-up approach in order to interpret and understand the results of our *in situ* heating experiments.

3 Materials and Methods

Nanoparticle synthesis Superfluid He nanodroplets serving as 'nanolabs' are used to synthesize the desired Ni-Au particles via sequential pickup of different metal atom species. For a more detailed description we refer to previous publications[132, 142].

High purity He (99.9999%) at a pressure of 20 bar is expanded through a 5 ¯m nozzle at 7 K into vacuum. This expansion process results in the formation of superfluid He droplets containing an average number of 10^7 He atoms.[136] These droplets are then sequentially doped when passing through two resistively heated pickup cells, containing Ni and Au. Via variation of the individual vapor pressures, the amount of doped metal atoms can be adjusted. This way, the droplet gets first doped with Ni, resulting in the formation of a spherical Ni cluster, which is then coated by layers of gold atoms while passing through the second pickup cell. Using this technique it is possible to synthesize any desired core-shell combination in the core-shell configuration requested. The cluster sizes are log-normally distributed with an average diameter of $d = 6.2$ nm and a log-normal standard deviation of 1.3 nm. A Ni:Au ratio of 3:7 has been chosen for the experiment in order to obtain perfect conditions for a complete coating in the particle size regime between 2 and 10 nm. More than 90 percent of the synthesized structures show the desired Ni-Au core-shell structure. The rest is formed by Au clusters, most likely with traces of Ni below our detection efficiency. Note that our method of production in helium does not emphasize the appearance of "magical" numbers as there is no selective mechanism with regard to stability involved. The release of binding and kinetic energy from the metal atoms throughout the cluster formation process results in the partial evaporation of the helium droplet. This loss in droplet size is monitored via a residual gas analyzer (Balzer QMA 200/QME 200). Finally, the beam is terminated

on a heatable TEM grid (DENSsolutions Nano-Chip XT SiN), where the clusters are deposited in a soft-landing process in which the excess helium is vaporized.[4, 27, 38, 134]

Electron Microscopy Characterization A probe corrected FEI Titan^3 G2 60-300 is used to record high angle annular dark-field (HAADF) images of temperature induced restructuring processes. Elemental analysis was carried out with a four-quadrant EDX spectroscopy detector and a Gatan Quantum energy filter for electron energy loss spectroscopy (EELS).

Computational Details All molecular dynamics (MD) simulations have been performed using the LAMMPS (Large-scale Atomic/Molecular Massively Parallel Simulation) package.[112] Newton's equations of motion have been solved through numeric integration via the velocity Verlet algorithm,[138] with time steps ranging from 1.0 to 3.0 fs.

A potential based on the embedded atom method (EAM) of Zhou et al.[155] for Ni-Au alloys has been used to describe all pair interactions. The EAM potential includes contributions for the embedding of each metal atom in the surrounding metal atoms. Therefore, it is expected to be more sensitive to surface nanoparticle effects than other additive pairwise interatomic potentials.

The dynamic range of solid Au and Ni indicates that a time step within the range of 3-5 fs would be acceptable. However, it is recommended that a smaller time step of about 1 fs is used instead when surface effects and initial instabilities are expected to appear, in particular at the initial steps of the simulation. For comparison, very recent state-of-the-art MD simulations on nickel and gold nanoparticles used a time step of 2 fs.[102, 113]

4 Results and Discussion

In Ref. 120 we discussed the interplay between oxygen presence and enhanced, temperature-induced, atomistic diffusion of Ni-Au core-shell clusters. We could demonstrate that even small traces of oxygen can completely dominate the outcome of the experiment, resulting in the core-shell inversion in Ni-Au to Au-NiO. As a consequence, studies of the unperturbed Ni-Au phase diagram at the nanoscale require entirely oxygen-free atmospheres throughout all measurements. We start with a description of the experimental observations under these conditions in our attempt to cover alloying, spinodal decomposition and demixing effects at high temperatures. In the second part, we use the LAMMPS suite of programs for MD simulations of the alloying process in solid phase by looking at mixing rates and as a function of initial composition at elevated temperatures.

4 .1 Experimental Observations

An overview of all reversible and irreversible processes covered in this article is provided in Fig. 5.1, together with the corresponding STEM images taken at various temperatures. For the sake of completeness we have also added results from our previous studies on Ni-Au oxidation Ref. 120 to further illustrate the impact of oxygen.

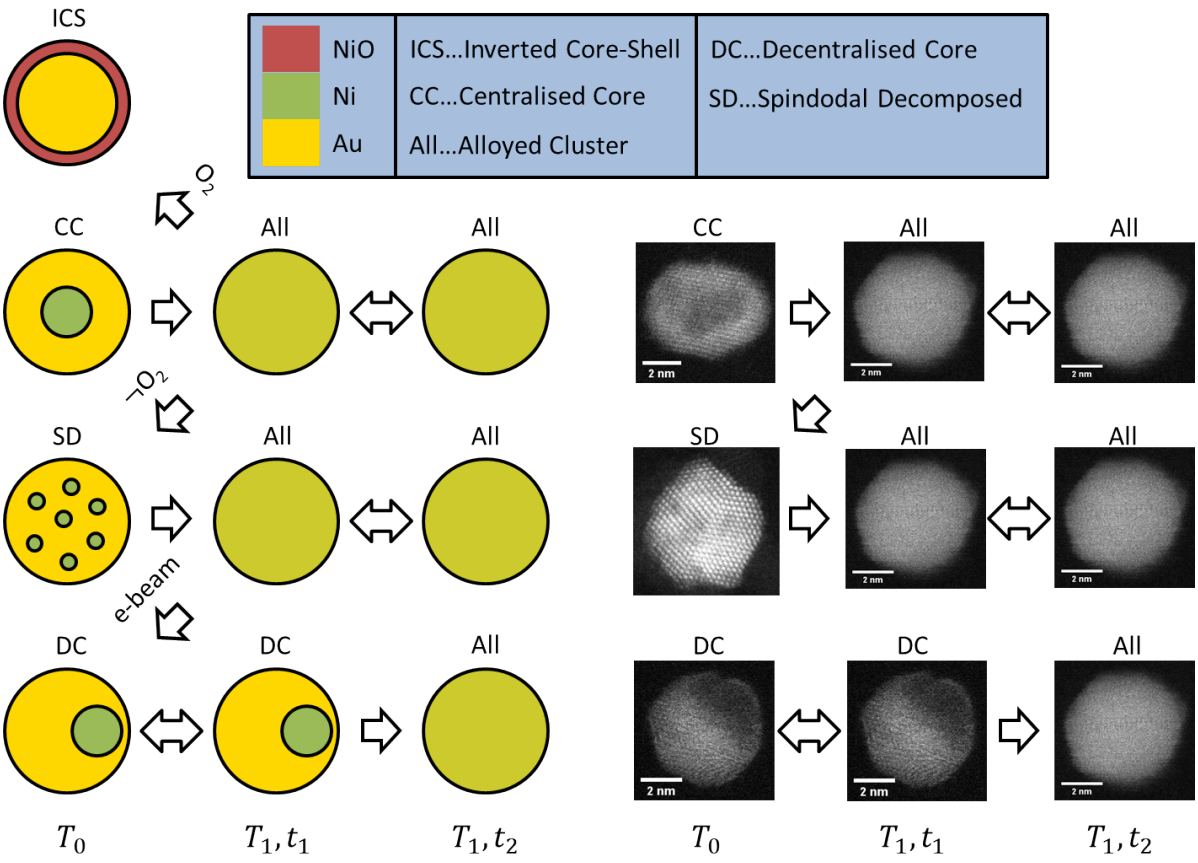

Figure 5.1: Temperature-induced structural transitions in Ni-Au core-shell nanoparticles with diameters in the nanometer range in symbolic representation (left) and as visualized by STEM imaging (right). The temperatures T_0, T_1 correspond to 25 and 400 °C and t_1 and t_2 correspond to 10 minutes and 12 hours, respectively. Note that even in clusters with a decentralized arrangement the Ni core remains protected by a layer of Au.

Starting from centralized core-shell structures (CC) in the upper left corner, synthesized as described in Section 3 , several pathways are possible regarding structural conversion. Within 4 s the temperature of the grid was increased from room temperature to 400 °C. At this temperature the system forms an alloy (All) within the scanning times of approximately one minute. This alloyed structure remains alloyed and no traces of

oxidation are found over the following observation time of 4 h. To prevent Ni oxidation, we use SiN_x grids as an alternative to the widely used amorphous carbon supports in order to reduce the amount of molecular oxygen adsorption and operate with steep heating ramps to quickly reach temperatures where the adsorption of oxygen from the microscope vacuum is decreased. However, if a sufficiently large electron beam dose is applied to the cluster, a spontaneous demixing occurs due to a selective enhancement of Au atomic mobility inside the cluster. The necessary dosage is inversely proportional to the actual cluster temperature; a separate study has been dedicated to analyze this effect.[69]. At a temperature of 400°C an electron dose of $2 \cdot 10^{10}$ electrons is required to trigger such a phase separation which leads to a decentralised Ni-Au core-shell cluster (DC). In the latter, the Ni core is typically residing in a sub-surface position, still embedded underneath a protective layer of Au atoms. This configuration seems to be a more stable minimum energy structure of the NiAu system, as neither continued heating up to melting temperature nor a cooling of the particles down to room temperature again is affecting the decentralized core-shell structure within observation times of about one hour. Note that all of these structural changes appear in the solid phase, as can be derived from the clearly visible lattice structures in the STEM images in Figure 5.1.

A different pathway is observed if an alloyed structure (All), obtained by heating of a centralized core-shell particle to 400 °C, is allowed to cool down to room temperature directly. In this case, spinodal decomposition (SD) is observed, which leads to the aggregation of small Ni particles inside the Au cluster. This interesting structure also seems to represent a local minimum of the total energy at room temperature, which is, analogous to the centralized Ni core structure, also unstable upon heating as it turns into a fully alloyed particle at 400 °C.

Transitions between three completely different solid phase structures can be observed for NiAu clusters under UHV conditions ($5 \cdot 10^{-10}$ mbar).In order to provide representative statistics we investigate the phase transitions of more than 100 randomly chosen clusters with either centralized core-shell arrangement or a spinodally decomposed structure. Long-time observations are performed for 28 decentralized clusters. The clusters are log-normally distributed with an average diameter of $d = 6.2 \pm 1.3$ nm. The following subsections are dedicated to the temperature behaviour of each corresponding structural motive.

Centralized Core-Shell Clusters. Centralized Ni cores are the standard configuration in which the clusters are synthesized due to the sequential pickup technique, where exposure to Ni vapor is followed by exposure to Au vapor. The synthesis conditions

(droplet size, vapor pressure of metals) are set to single-center growth; see Section 3 for further details. The Ni core is fully encapsulated in a shell of Au, which would prevent it from oxidation even if exposed to ambient air. The structural rearrangements of the deposited clusters at elevated temperature are illustrated in Figure 5.2. Upon increasing the temperature, the mobility also increases, resulting in the intermixing of the two metal species at temperatures around 400°C. We note that in this temperature range the danger of undesired oxidation is largest due to the thermally enhanced mobility of the Ni atoms and the inevitable traces of oxygen produced during electron microscopy scans. In order to minimize the risk of Ni oxidation we use SiN_x chips as supports, which reduces the hydrocarbon background drastically in comparison to substrates based on amorphous carbon. Additionally, we employ a very steep heating ramp (see Supplementary Information) from room temperature to 400°C in 4 s in order to minimize the exposure time of the clusters to any oxygen present in the microscope vacuum (10^{-8} mbar) or adsorbed at the grid. After alloy formation, the cluster remains in this mixed, solid structure until it undergoes a first order phase transition into the liquid state.

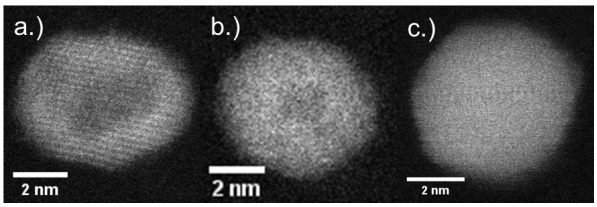

Figure 5.2: Thermal evolution of an initially centralized core-shell cluster. a) room temperature, b) 400°C, c) 700°C.

Spinodally Decomposed Clusters. Spinodal decomposition becomes visible when performing an in-chamber heating to temperatures above 300°C, keeping this temperature constant for about 30 min, followed by a final cooling of the sample back to room temperature. Reduced mobility in this final step typically results in the formation of several smaller Ni agglomerates embedded in a Au matrix (see Fig. 5.3). It can be assumed that the system gets trapped in local minimum structures with energies above that of the decentralized Ni core. However, the experiment does not answer whether the multi-centered structure is lower or higher in energy than a centralized Ni core. Upon increasing the temperature, spinodally decomposed NiAu structures undergo the same pathway as the initially centralized core-shell clusters by forming an alloy at about 400°C.

Decentralized Core-Shell Clusters. Our experiments indicate that a decentralized

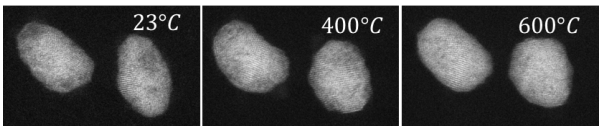

Figure 5.3: Evolution of spinodally decomposed clusters at elevated temperatures. Similar to centralized clusters, they form an alloy at 400°C.

position of the Ni core corresponds to a thermally more stable structure for nanometer-sized NiAu clusters in the solid phase. A closer investigation of the typical Ni core positions and shapes in this 'final' configuration suggests that a single agglomeration of Ni directly under a facet of the Au shell is the most feasible structural motive. While a centralized core structure becomes mixed within a minute at 400 °C, a decentralized cluster is observed to be stable for several hours, exceeding the standard measurement time. In order to determine whether entropy or inner energy dominates the final configuration, we synthesized a total number of 28 decentralized clusters "on the fly" by electron beam exposure at 700°C, where the intrinsic electron dosage applied by the STEM is sufficient to induce the desired structural changes almost immediately, and keep them at 450°C for 12 hours without further manipulation. After that, a final STEM examination is performed. This final investigation confirms that also decentralized clusters are metastable as they end up in a mixed state with entropy at its maximum. From this outcome we conclude that, independent of the initial configuration, alloying takes place at temperatures above 300°C. However, the time required for this transition to take place is strongly dependent on the initial configuration of the bimetallic cluster. In Fig. 5.4, a random group of three initially de-centralised core-shell clusters is kept at 450°C for 12 hours.

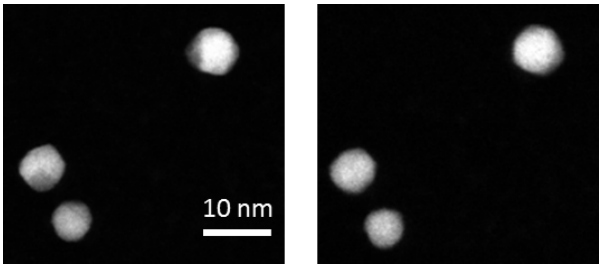

Figure 5.4: Example transformations from decentralized core-shell structures to mixed clusters, visualised by a comparison of STEM images taken before and after 12 hours at 450°C.

4 .2 Molecular Dynamics Simulations

To reproduce realistic experimental conditions we have performed large-scale atomistic simulations relying on the embedded atom method (EAM)[155] to describe inter-atomic interactions. As a reasonable representative of the experimental cluster size distribution (2 to 10 nm) and metal dotation ratio (3:7) we build a core-shell model system from 900 Ni and 2100 Au atoms, which yields a nanoparticle with a diameter of about 5 nm. An even larger nanoparticle composed of 6266 atoms has been simulated as well in order to test for size dependencies.

4 .2.1 Synthesis of model nanoparticles

In order to obtain nanoparticles with geometries as close as possible to the outcome of the assumed growth process inside the helium matrix[57, 60] we proceed in a two-step fashion: First, a Ni core of 900 atoms is allowed to fully relax. Then, a shell of Au atoms is added to the system and allowed to structurally relax while the Ni structure is kept frozen. This procedure takes into account that the actual synthesis inside the He droplet is considered to take place 'atom by atom'. In other words, at the time when the droplet arrives the second pickup and starts to collect Au atoms, a Ni core in a minimum energy configuration can be assumed inside the He droplet.

In our 'virtual' synthesis, 900 Ni atoms are randomly located inside a sphere with a radius of 14.0 Å and cooled down using a Berendsen thermostat at 0.001 K, allowing a maximum atomic displacement of 0.01 Å. The value of 14 Å is consistent with an estimate of the Ni core diameter d following the relationship d [nm] = 31.72 - 282.85 $N^{-1/3}$ as suggested in Ref. 102, resulting in a value of about 24 Å for a structure containing 900 Ni atoms. Next, an annealing procedure is applied, where the Ni nanoparticle is heated up to 900 K and kept at this temperature for 5 ns. Then, the nanoparticle was cooled down again to 0.4 K, resulting in its crystallization. The addition of the 2100 Au atoms follows a similar approach. First, they are randomly localized in a spherical shell with an internal (external) radius of 14 Å (24 Å) around the Ni core. Second, the same heating and annealing procedure described is performed as above, allowing the Au_{2100} shell to crystallize as well, while the geometry of the Ni core is kept frozen.

4 .2.2 Dynamics at elevated temperatures

Both the centralised as well as the decentralised $Ni_{900}Au_{2100}$ nanoparticles were heated to 300 K in 0.5 ns (i.e., applying a heating rate $\Delta T/\Delta t$ of 6×10^{10} K s^{-1}). Using a Langevin thermostat, the temperature of 300 K was kept for 5 ns. Next, the nanoparticles were heated by increasing the temperature in steps of 50 K within 0.5 ns (i.e., with a heating rate of 5×10^{9} K s^{-1}). Each value of the temperature was then kept fixed for 5 ns before further heating, until a final value of 750 K was reached. The first signal of the diffusion of Ni atoms was observed at 550 K.
Next, the nanoparticle was heated up to 900 K in 0.5 ns, keeping this value of the temperature during 5 ns. Then, the time step of the simulation was set to 2 fs for 245.5 ns. Finally, the time step was increased to 3 fs, and the temperature of the nanoparticle was kept at 900 K for 186.5 ns. This procedure allowed us to test if the time step of 3 fs was still small enough to avoid the appearance of instabilities or abrupt changes in the behaviour of the nanoparticle. After confirming that a time step of 3 fs can be applied, this value was used in the last steps of the simulation, allowing us to study long-time diffusion processes on timescales of several hundred ns.

4 .2.3 Comparison between CC and DC dynamics

At 900 K, the diffusion process is fast enough to be studied via MD simulations. To analyze this behaviour, we found the average Ni atom radial distance from the center-of-mass to be the most suitable parameter for modelling. The simulations were carried out for both model particles, consisting of 3000 and 6266 atoms, respectively. Both cluster models show the same interesting behaviour: while a decentralized Ni cluster has a higher overall diffusion, a centralized cluster exhibits a larger radial diffusion towards a fully intermixed state. As can be seen in Figure 5.5 (see also Figure 10 of the Supporting Information), the diffusion of decentralized Ni cores is mainly limited to subsurface positions, which leaves the remaining Au cluster intact, resulting in a slower convergence towards a fully intermixed bimetallic cluster. In contrast, for the centralized Ni cores, the nickel atoms diffuse radially through the gold shell towards the subsurface region in the centralized nanoparticle.

To try to understand this remarkable behaviour we have calculated the average dis-

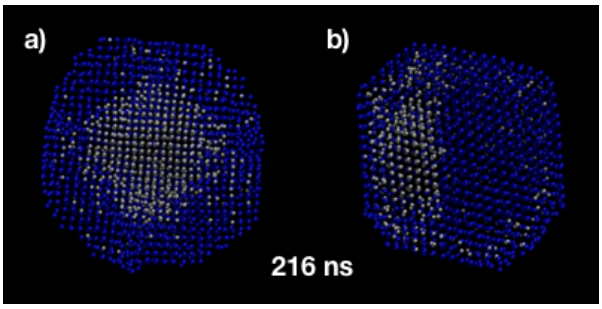

Figure 5.5: Simulation snapshots of a nanoparticle consisting of 6266 atoms, showing the different diffusion processes of Ni atoms through the Au shell observed in centralized (a) and decentralized (b) nanoparticles at 900 K, taken after 216 ns (see also Figure 10 of the Supporting Information).

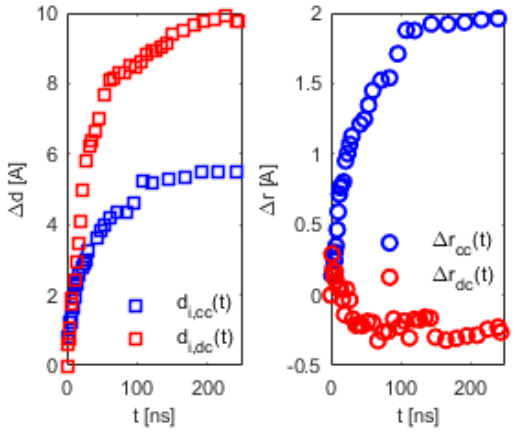

Figure 5.6: Average overall diffusion distance Δd (left) and radial diffusion distance Δr (right) of Ni atoms in a decentralized (red) and centralized (blue) cluster, plotted as a function of time.

placement distance $\Delta d(t)$,

$$\Delta d(t) = \frac{1}{N_{Ni}} \sum_{j=1}^{N_{\mathrm{Ni}}} |\vec{r}_j^{\,\mathrm{Ni}}(t) - \vec{r}_j^{\,\mathrm{Ni}}(t=0)| \tag{5.1}$$

as well as the radial displacement $\Delta r(t)$:

$$\Delta r(t) = \frac{1}{N_{\mathrm{Ni}}} \sum_{j=1}^{N_{\mathrm{Ni}}} \left(\vec{r}_j^{\,\mathrm{Ni}}(t) - \vec{r}_j^{\,\mathrm{Ni}}(t=0)\right) \cdot \vec{e}_r \tag{5.2}$$

with $\vec{r}_j^{\,\mathrm{Ni}}(t)$ being the position of the jth Ni atom j at time t. It is found that the radial diffusion (see right graph in Figure 5.6) for a centralized cluster behaves exponentially,

as expected, and on average the Ni atoms changed their radial position by 2 Å after 250 ns. For a decentralized cluster it can be seen that the change in the radial distance after 250 ns hardly happens at all.

In addition, we found that the diffusion of Ni atoms in decentralised clusters is mostly limited to the positions below the surface. This phenomenon is caused by the reduced lattice mismatch underneath the surface. The average change in absolute distance Δd after 250 ns for the decentralized cluster is 10 Å in comparison to 5.5 Å for a centralized core (see left graph in Figure 5.6). Furthermore we observed that the energetic 'cost' of placing Ni atoms at the surface is rather high in comparison with placing a Au atom at the surface. The energetic 'gain' of exchanging one Ni atom from the surface to a subsurface position is about 0.2 eV higher than the energetic 'gain' when transferring a Au atom from the surface to a subsurface position. This is analyzed in greater detail in the Supporting Information. A similar interplay between bulk, surface, and strain effects and their impact on the morphology of a bimetallic nanoparticle has recently been discussed for the closely related CuAg system.[114] In this theoretical study of Rahm and Erhart, the segregation of the two metals is strongly influenced by local lattice strain. Agglomerations of Cu are preferred at regions of high lattice strain in the Ag matrix. Depending on the shape of the nanoparticle, this can be either in the center of the metal cluster or at a subsurface position. Our findings regarding Ni diffusion in a Au matrix fit nicely to these predicted lattice strain tendencies.

Another scenario may be the spinodal decomposition of the alloyed system. The earliest findings in this direction have been revealed by Nelli and Ferrando in a very recent work.[101] However, note that our systems are about 10 times larger than those treated in Ref. 101. Due to the computational effort, which increases with the 2nd power of system size at least, combined with the necessity of even smaller timesteps due to the lower temperature, a simulation of spinodal demixing is currently beyond our reach.

5 Conclusions

Irrespective of the future usage of bimetallic core-shell nanoparticles e.g. for medical, optical or chemical purposes, it is clear that the structural integrity of the layers, also at higher temperatures, is a knockout criterion for any planned industrial application.

Taking advantage of the He-mediated synthesis of mixed-metallic structures in combination with meticulously controlled electron beam dosage after particle deposition, we were able to prepare NiAu core-shell samples in different geometries for a follow-up study

of their structural stability at higher temperatures. Comparing centralised Ni-cores, decentralised Ni-cores as well as spinodally decomposed Ni-cores, we found that these differences in the initial geometries have a tremendous impact on intermetallic diffusion behaviour and therefore affect the times for an inevitable alloying at higher temperatures. We were able to confirm that, starting at a temperature of 300°C, all initially separated structures undergo a transition towards a fully alloyed state. The lower alloying temperature for Ni-Au nanoparticles in comparison to the bulk materials confirms the predictions made via the CALPHAD approach (see Supporting Information).[124]. However, an analysis of structural changes via TEM imagery reveals that clusters featuring a decentralised core possess a pronounced structural integrity, which we link to a different diffusion behaviour. From computationally costly large-scale molecular dynamics simulations over several hundred nanoseconds we conclude that a decentralised core affects the overall structure of the particle in a way which promotes diffusion processes along the intermetallic interface, but quenches atomic intermixing along the radial coordinate. In the concrete case, this subtle change in the diffusion mechanism leads to an extension of the alloying times by two orders of magnitude. Depending on the actual position of the Ni core, lattice strain appears to be distributed differently: while a central position seems to increase Ni mobility throughout the cluster, a decentralised core position, where the Ni core is located at a subsurface position, shows less pronounced diffusion tendencies which also remain mostly within the subsurface region of the cluster. This indicates that the inclusion of Ni atoms near the surface (but not at the surface) allows for an effective compensation of lattice strain which stems from the finiteness of the nanoparticle.

6 Acknowledgement

The authors thank Florian Lackner and Roman Messner for many fruitful discussions. This research has been supported by the Austrian Science Fund (FWF) under Grant P 29893-N36 and FWF PIR8-N34, the Spanish Agencia Estatal de Investigación (AEI) and the Fondo Europeo de Desarrollo Regional (FEDER, UE) under Grant No. MAT2016-75354-P, and by the COST Action CM1405 “Molecules in Motion" (MOLIM). The authors would like to acknowledge the use of HPC resources provided by the ZID of Graz University of Technology and by the Vienna Scientific Cluster (VSC). The CESGA super-computer center (Spain) is also acknowledged for having provided computational resources. Further support by NAWI Graz is gratefully acknowledged.

7 Supporting Information

The supporting information includes an elaborated description of the molecular dynamics simulations (see section 7 .1) and provides further details about the decentralization of the clusters, induced via electron beam damage (see section 7 .4) as well as the modified Ni-Au phase diagram (see section 7 .5).

7 .1 Methods: Atomistic Molecular Dynamics Simulations

All molecular dynamic (MD) simulations have been performed using the LAMMPS (Large-scale Atomic/Molecular Massively Parallel Simulation) package.[112] The Newton's equations of motion have been solved through numeric integration by using the velocity Verlet algorithm,[138] with time steps ranging from 1.0 to 3.0 fs.

7 .1.1 Interatomic Interaction Forces: Pair Interaction Potentials

The potential obtained via the embedded atom method (EAM) of X. W. Zhou[155] for metal alloys has been used to describe all pair interaction. As indicated in the cited article "*These potentials are well fitted to basic material properties such as lattice constants, elastic constants, bulk module, vacancy formation energies, and sublimation energies, and they predict reasonably well the heats of solution*". The EAM potential includes contributions for the embedding of each metal atom in the surrounding metal atoms. Therefore, it is expected to be more sensitive to surface nanoparticle effects than other additive pairwise interatomic potentials. In fact, it is one of the most popular potentials in atomistic simulations on nanomaterial properties (see., e.g., Ref. 116 for a recent overview of the EAM method). During the last few years, however, other potentials sharing similar functional forms have been developed such as the GUPTA potential.[26, 56, 115] The *eam database tool* included in the LAMMPS package was used to derive the necessary alloy parameters (see appendix A of Ref. 155 for the details).

7 .1.2 Initial Nanoparticle Formation

The dynamic range of solid gold and nickel indicates that a time step within the range of 3−5 fs would be acceptable. However, it is recommended that a smaller time step of about 1 fs is used instead when surface effects and initial instabilities are expected to appear at the initial steps of the simulation. For comparison purposes, very recent

state-of-the-art MD simulations on nickel and gold nanoparticles used a time step of 2 fs.[102, 113]

To create the initial nanoparticle, 900 Ni atoms were randomly located inside a sphere with a radius of 14.0 Å, cooling it down using a Berendsen thermostat at 0.001 K and allowing a maximum atomic displacement of 0.01 Å (see left-hand panel of Figure 5.7). The value of 14 Å was consistent with an estimated diameter d of the nickel nanoparticle following the relationship d [nm] = 31.72 - 282.85 $N^{-1/3}$ from Ref. 102, resulting in a value of about 24 Å for a number of Ni atoms $N = 900$. Next, an annealing procedure was applied as follows: First, the Ni nanoparticle was heated up to 900 K and this temperature was kept during 5 ns. Second, the nanoparticle was cooled down to 0.4 K, resulting in the crystallization shown in the right-hand panel of Figure 5.7.

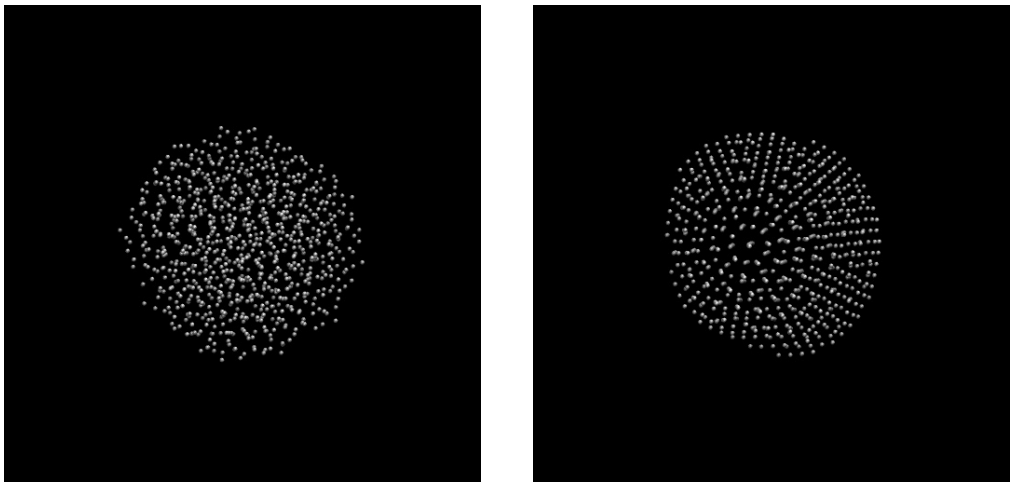

Figure 5.7: Left-hand panel: initial random configuration of the Ni_{900} nanoparticle. Right-hand panel: final configuration after applying our annealing procedure.

To include the 2100 Au atoms into the nanoparticle, they were randomly localized in a hollow sphere with an internal (external) radius of 14 Å (24 Å) around the core Ni_{900} nanoparticle. Keeping fixed the atoms of the Ni_{900} core, we applied the same annealing procedure described above (see Figure 5.8), allowing the Au_{2100} shell to crystallize as well.

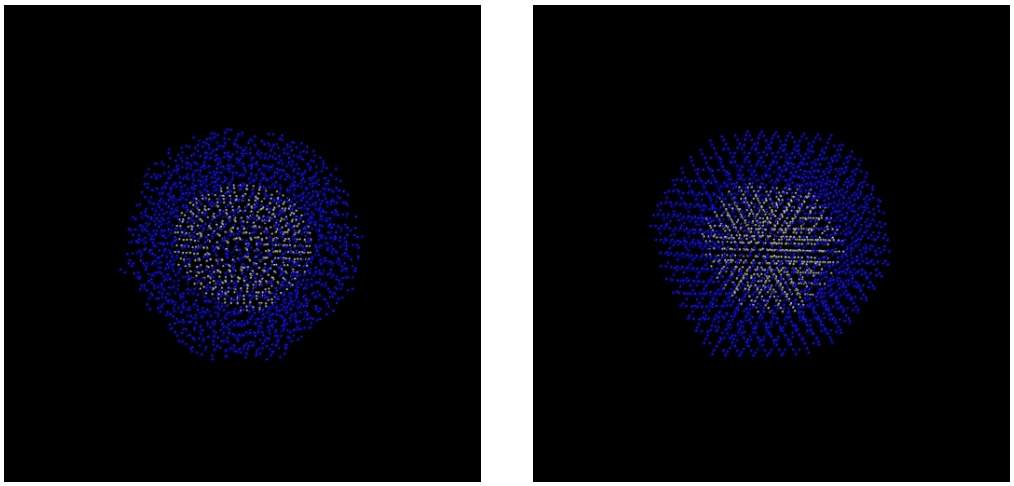

Figure 5.8: Left-hand panel: initial random configuration of the shell Au_{2100} nanoparticle. Right-hand panel: final configuration of the core-shell $Ni_{900}Au_{2100}$ nanoparticle after applying our annealing procedure.

7 .1.3 Diffusion of Ni Atoms into the Solid Nanoparticle

To analyze the diffusion at 900 K, Figure 5.9 presents the evolution vs. time of the average nickel concentration at a given radius from the center of the nanoparticle [referred to as C_{Ni}(r)]. The radius of the nanoparticle is 25 Å. For comparison purposes, the function C_{Ni}(r) is also presented at 300 and 750 K. From C_{Ni}(r) at 300 K (shown in red), it can be noticed that the Ni core is not a perfect sphere. The functions C_{Ni}(r) shown in dark-blue and dark-green correspond to temperatures of 750 and 900 K, respectively. It can be observed that they are very similar, reflecting both of them the exchange of a few atoms between the Ni core and the Au shell during the heating process. After reaching the temperature of 900 K, the diffusion of the Ni atoms over the nanoparticle is much more appreciable. Up to 20 ns, the effect is much more significant (the differences in C_{Ni}(r) are more pronounced). Then, the diffusion process slows down. This way, the functions C_{Ni}(r) at 50 and 90 ns (shown in black and violet) are very similar.

With the exception of the nanoparticle at $t = 15$ ns (curve shown in cyan), there is no significant concentration of Ni atoms close to the surface at 25 Å. However, it should be stressed that the concentration at the surface is never strictly zero. There is always a certain but small amount of Ni atoms exposed on the surface at any time.

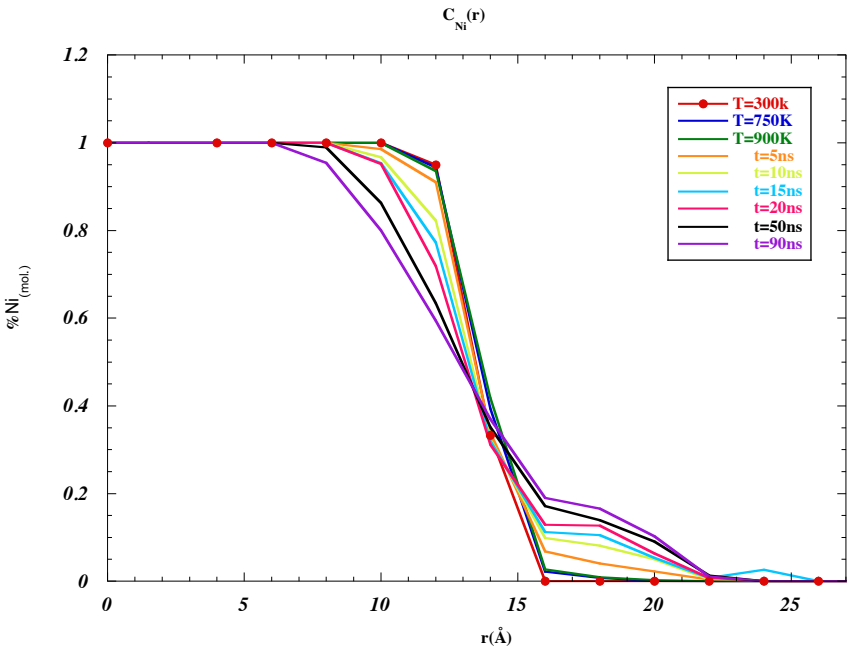

Figure 5.9: Scans of the average nickel concentration as a function of the radial distance from the center of the nanoparticle

7 .2 Melting Process

The nanoparticle was heated up to 1000 K, being still solid. However, an increase of the temperature to 1100 K lead to the melting of the particle. To estimate a more precise value of the melting temperature, the temperature was increased in steps of 1 K in 150 ps (i.e., with a heating rate of about 6.7×10^9 K s^{-1}). Each increased value of the temperature was kept during 7.5 ns repeatedly. Applying this fast heating process, the particle melted during the 7.5 ns of the simulation at a temperature of 1036 K. Aimed to study the phase transition while keeping reasonable simulation times, a new simulation at 1035 K was followed by starting from the previous one at 1036 K (after 7.5 ns of production run).

One way of visualizing the phase transitions is through the analysis of the time-dependent evolution of the pair function G(r) (i.e., the radial distribution function). This function

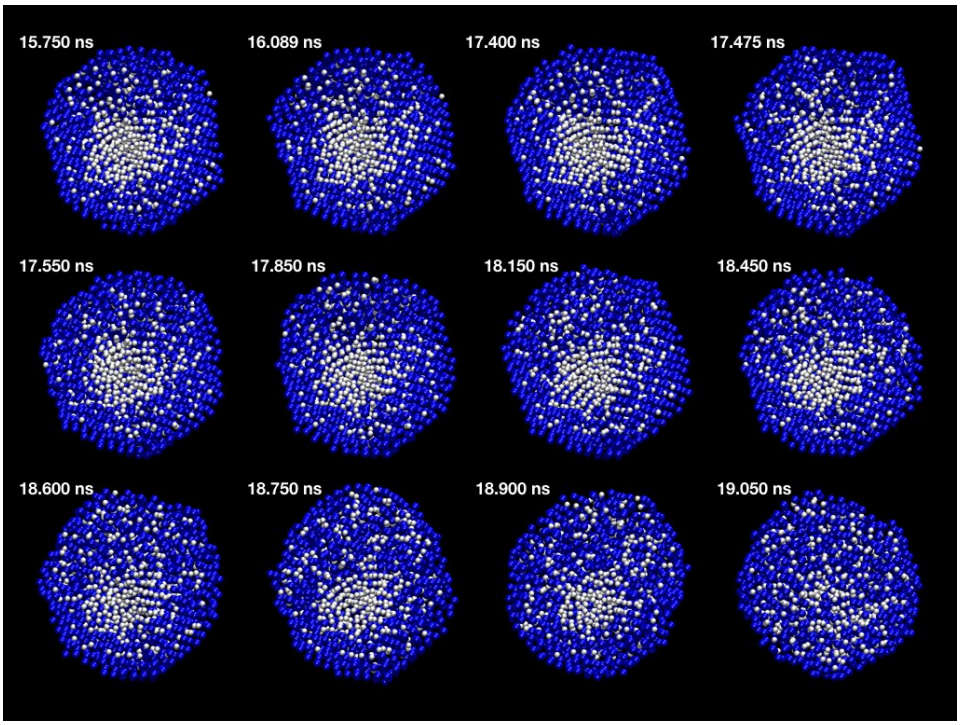

Figure 5.10: Snapshots of a core-shell Ni−Au nanoparticle at different times of the melting process at T=1035 K.

describes how density varies as a function of the distance between two particles. More

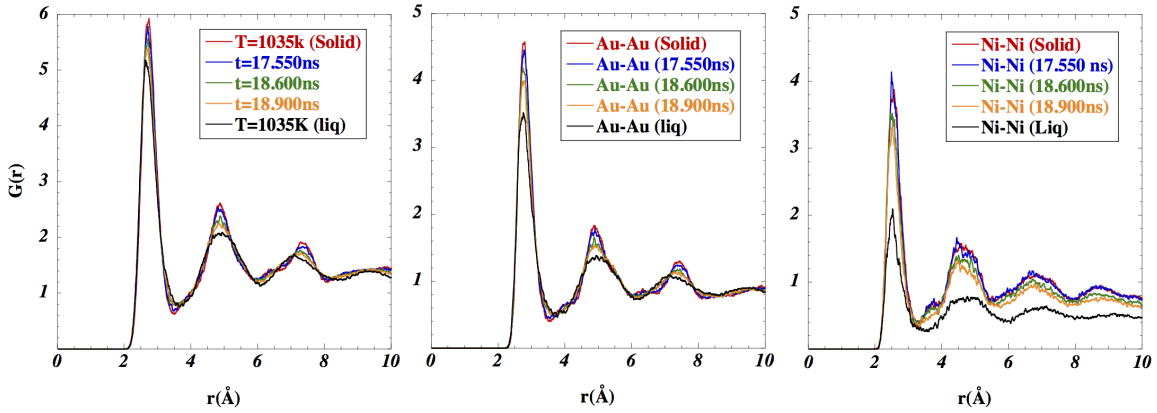

Figure 5.11: Evolution of the pair function G(r) as a function of time, corresponding to the same times considered in the snapshots of Figure 5.10. Left-hand panel (total), middle panel (Au-Au pairs), right-hand panel (Ni-Ni pairs).

specifically, it is defined as:

$$G(\mathbf{r}) = \frac{1}{\rho}\langle \sum_{i \neq 0} \delta(\mathbf{r} - \mathbf{r}_i) \rangle \tag{5.3}$$

where ρ is the average density of the system. As discussed below, the analysis of this function clearly shows that the gold and Ni melting processes are different, with the latter being much less gradual.

Let us focus in the picture showing the snapshots at different times of the melting process at 1035 K (Figure 5.10) along with the graphics (see Figure 5.11) presenting the pair functions, G(r): both total (left-hand panel) and those restricted to Au-Au (middle panel) and Ni-Ni pairs (right-hand panel). Figure 5.12 presents eights panels, extending Figure 5.11 to all possible pairs and including a second set of graphics (right-hand panels) in which the range of considered distances is larger.

The function G(r) shown in red in Figure 5.11 (referred to as “solid") corresponds to the snapshot taken at 15.75 ns in Figure 5.10. At $t = 16.089$ ns, notice that the Au phase at the left- upper region of the nanoparticle has started to melt. About 1.5 ns later, at $t = 17.55$ ns, the Au−Ni phase on top of the Ni core has just melted. After 18.9 ns, almost all the allowed Au−Ni phase has melted. However, only after 19.05 ns, the Ni core becomes completely melted, experiencing a very fast homogenization. This is clearly reflected in the pair function G(r) of Ni-Ni pairs (shown in black in the middle panel of Figure 5.11 and referred to as “liquid").

It is important to notice that the melting process is more evident from the G(r) function for the Ni-Ni pairs. It can be observed that, at $t = 17.55$ ns, the G(r) function is almost the same as for the solid phase. After 18.9 ns, the Ni core starts to destabilize so that the peak of the G(r) function located at about 4.75 Å disappears. However, the abrupt change takes place later, in between $t = 18.9$ and 19.05 ns (see the G(r) function shown in black and referred to as “liquid"): Notice that, due to the disappearance of the solid Ni core, the heights of the peaks of the G(r) function suddenly decrease and become shifted. While the distances between nearest and next-nearest neighbors are kept very similar, those to third-nearest neighbors (at about 7 Å) become significantly shifted, and the heights of the peaks abruptly decrease due to the transition to the liquid phase.

The sudden disappearance of the Ni core can also be observed in the G(r) function for Ni-Au pairs (see third panel from the top in Figure 5.12). Thus, from Figure 5.12, a sudden jump in the average height of the G(r) function is clearly discernible in between

18.9 and 19.05 ns along with an increase of the G(r) value at distances shorter than 10 Å. However, the modification in the position and width of the peaks in the G(r) function is happening more gradually than for the Ni-Ni pairs due to the more progressive nature of the melting process for the Ni-Au alloy. For instance, we can notice the disappearance of the shoulder in the G(r) function at 4.0 Å as well as a progressive regrouping of two peaks (at 6.5 and 7.5 Å, respectively) in just one peak localized at about 7 Å.

The progressive nature of the melting process for the Au-Ni alloy is also reflected in the time-dependent evolution of the G(r) function for Au-Au pairs (see middle panel in Figure 5.11). The only relatively abrupt change is the jump in the average values of G(r) for distances larger than 10 Å. Once again, such modification arises from the disappearance of the Ni core and the associated hole in the gold structure.

Altogether, the G(r) functions shown in Figures 5.11 and 5.12 are consistent with those reported for pure gold and nickel nanoparticles[102, 113] as well as for bulk gold.[113] In particular, the G(r) function for the gold shell of the nanoparticle shows there major peaks at 2.8, 5.1, and 7.6 Å, and two minor peaks at 4 and 6.5 Å. These peaks are very close to those reported for the G(r) function in bulk gold (FCC packing), with the three major peaks located at 2.8, 5.1 and 7.8 Å (see Ref. 113). Similarly, it has been shown that these major peaks in the G(r) function drop while the minor peaks disappear at the melting temperature (1350 K for bulk gold).

It is also interesting that the G(r) function for the nickel core of the solid nanoparticle reflects a multi-domain structuring, with a mixing of FCC and HPC phases. As discussed in Ref. 102 for a pure nickel nanoparticle, this can be deducted from the fact that secondary peaks are made of several overlapping maxima. The first major peak is located at a distance, 2.5 Å (see Figures 5.11 and 5.12), which is a distance very similar to that found in Ref. 102 for a pure Ni_{4000} particle (2.45 Å). The same holds true for the second and third maxima localized at 4.5 and 7.0 Å, as well as for the minor peak at about 3.8 Å. However, the heights and widths of the peaks are rather different: the Ni_{900} core has a higher mixing degree of FCC and HPC structures than the pure Ni_{4000} particle (see Figure 4 of Ref. 102). Work is in progress to study the relative weights of FCC and HPC structures in the Ni_{900} core using the common neighbor analysis (CNA) method.

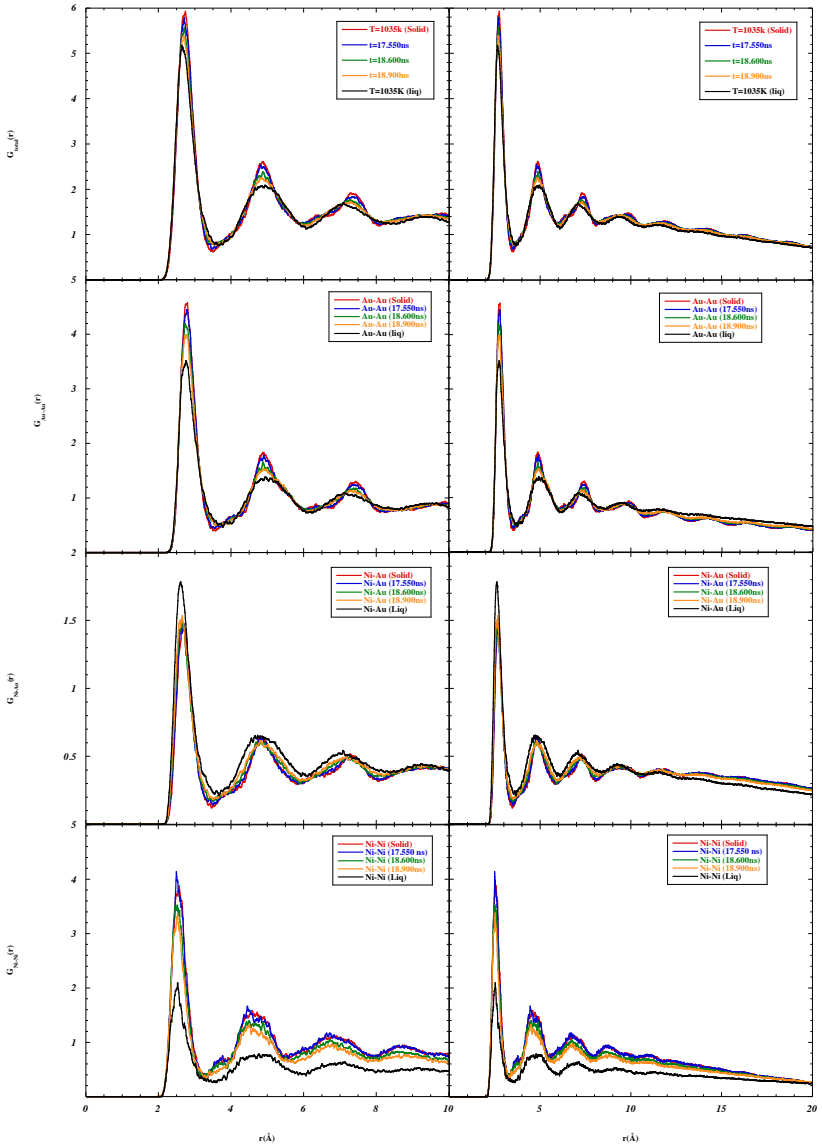

Figure 5.12: Evolution of the pair function G(r) as a function of time, corresponding to the same times as for the snapshots presented in Figure 5.10.

7 .2.1 Discussion

Although some diffusion can be observed over the solid nanoparticle at a temperature as low as 550 K, it is not significant enough to be studied within the time scales accessible in classic simulations up to a temperature of about 900 K. Initially (at 900 K and during 50 ns), the diffusion into the solid nanoparticle is a fast process. After 50 ns, however, the Ni concentration changes very slowly, with that located in the surface of the nanoparticle being negligible. The Ni core would be either kept almost unmodified or fully mixed at macroscopic time scales. The final outcome will depend on the size of the nanoparticle and thermal conditions (i.e., heating rates).

At 1000 K the core-shell $Ni_{900}Au_{2100}$ nanoparticle is still solid and, under very fast heating conditions (a heating rate of about 6.7×10^9 K s^{-1}), a melting temperature of 1035 K can be estimated. This melting temperature is much lower than that of either bulk gold (1336 K) or bulk nickel (1728 K). As previously shown in MD simulations of pure Ni nanoparticles,[102] the melting temperature increases with heating rate and decreases with nanoparticle size, scaling with the number of atoms as $N.^{-1/3}$ Melting temperatures in the range of 1460−1375 K have been reported for nickel nanoparticles containing from 4000 to 8788 nickel atoms, applying higher heating rates in the range from 2×10^{12} K s^{-1} to 4×10^{12} K s^{-1} (see Ref. 102). For comparison purposes, molecular dynamics simulations on gold nanoparticles (from 675 to 5425 atoms) indicated melting temperatures from 615 to 1115 K (see Ref. 113). For instance, a melting temperature of 1075 ± 5 K was reported for a gold nanoparticle having a diameter (4.89 nm) similar to that studied in our work (5.0 nm).

It should also be stressed that our estimation of the melting temperature (1035 K) is consistent with the phase diagram reported by Jopoušek et al.[124] using the CALPHAD method.[68] Thus, from Figure 2 of Ref. 124, melting temperatures of about 1150 and 1100 K can be estimated for AuNi nanoparticles with sizes of 20 and 13 nm, respectively (keeping a Ni to Au ratio of 3:7).

It is also interesting to note that the melting process starts from surface defects and, later, it is expanded through the Au-Ni alloy while keeping the Ni core almost intact. Of course, the melting process might depend on the particular heating procedure. For instance, if the heating is indirect through the nanoparticle support, the melting process would obviously start from the surface side closest to the support. Finally, the Ni core also experiences a very fast melting. The sudden nature of the melting for the Ni core

could be a signal of instability due to its small size. Therefore, it is possible that, for a larger nanoparticle having also a larger Ni core, it is kept stable while the Au-Ni alloy becomes melted.

7 .2.2 Decentralized core-shell Ni−Au nanoparticle

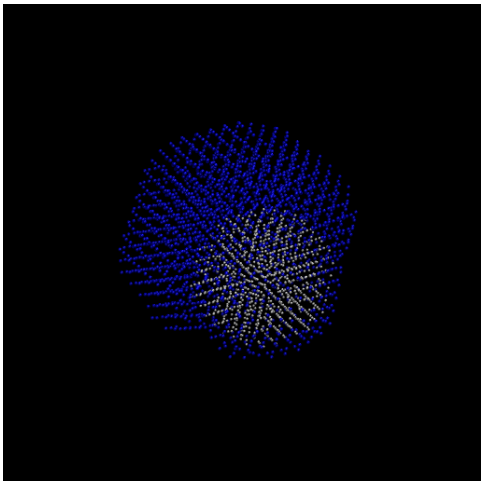

Figure 5.13: Picture illustrating the decentralized core-shell Ni−Au nanoparticle formed by applying our annealing procedure in MD simulations.

By applying the same procedure discussed above, we have also performed the simulations for the decentralized core-shell Ni−Au nanoparticle shown in Figure 5.13. The total energies of the centralized and decentralized nanoparticles were −11793.101 and −11694.488 eV, respectively. The estimated melting temperature is a little bit lower for the decentralized nanoparticle (in between 900 and 1000 K) for the centralized one. It should be also stressed that there are many possibilities of structuring for the decentralized nanoparticle.

Finally, Figure 5.14 illustrates how much the total energy is modified upon increasing the distance from the Ni core center-of-mass to the center-of-mass of the total core-shell NiAu nanoparticle. As indicated, the origin corresponds to the centralized NP (energy of −11793.101 eV) while, at the largest distance, the energy is that of the decentralized nanoparticle (energy of −11694.488 eV). The annealing procedure was applied as before but moving and constraining the distance between the center-of-mass of the Au shell and the Ni core. At any geometry, the atoms from the Au shell were allowed to relax but not those of the Ni core. Using Zhou's potential, the energy differences between centralized and decentralized structures are minimal (within 1%) and there is no barrier, with the

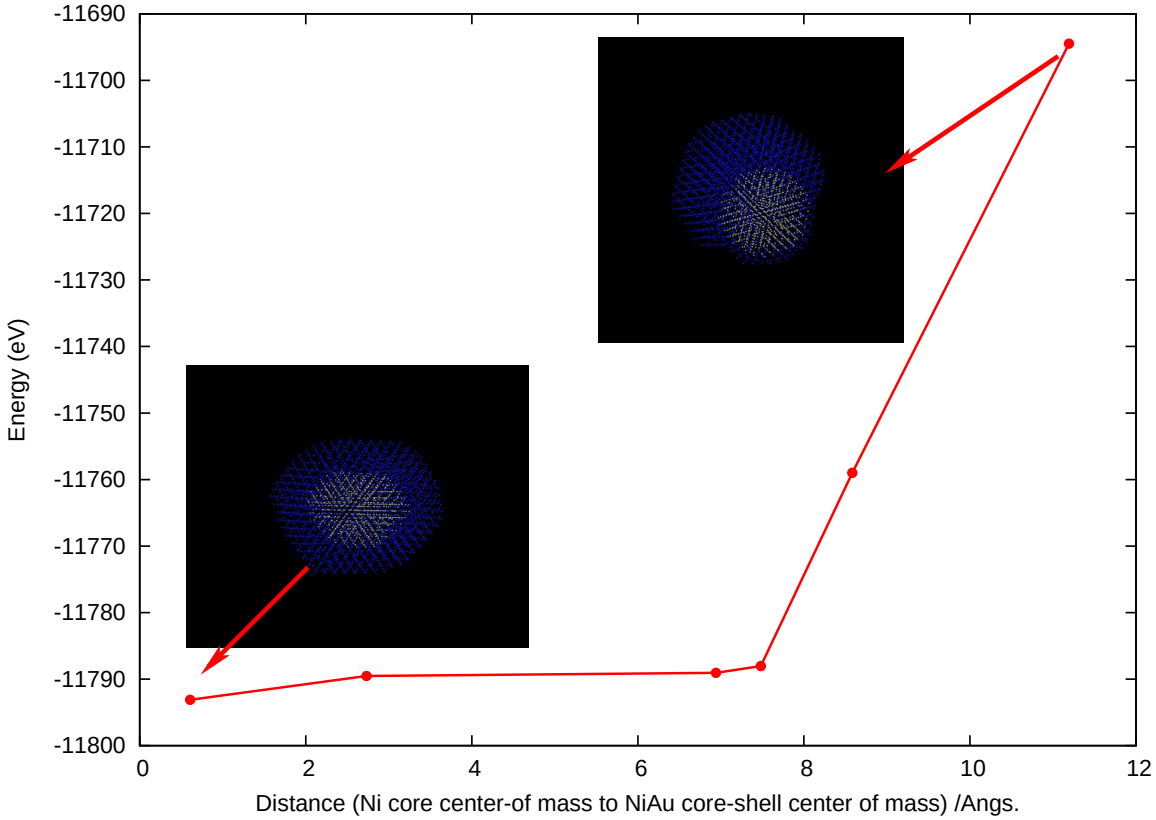

Figure 5.14: Picture illustrating how much the total energy is modified upon increasing the distance from the Ni core center-of-mass to the center-of-mass of the total core-shell NiAu nanoparticle.

energy increasing slowly up to ca. 8 Å and then rapidly up to ca. 11 Å. The sudden increase occurs at the distance for which the Ni core starts to deform the outer surface of the Au shell.

7 .2.3 Further Insights into the Reasons Why Ni Atoms Prefer Not to Go Further the Subsurface Region

Lastly, in order to get further insights into the reasons why Ni atoms prefer not to go further the subsurface region, we have represented the energy per atom as a function of the distance to the nanoparticle surface for both Ni (red line) and Au (blue line) cases. In general, for distances larger than 0.3 and smaller than 2 Å, the nickel location in the nanoparticle is favored. However, as can be clearly seen in Figure 5.15, the energy per atom of nickel goes down very rapidly up to about 5 Å from the surface but, then, it

stabilizes around −4.1 eV/atom (with some noise around that value). In stark contrast, for the gold case, the energy per atom continue to decrease further even at distances larger than 17 Å. It nicely shows the preferential gold (nickel) location on the surface (subsurface) region of the nanoparticle.

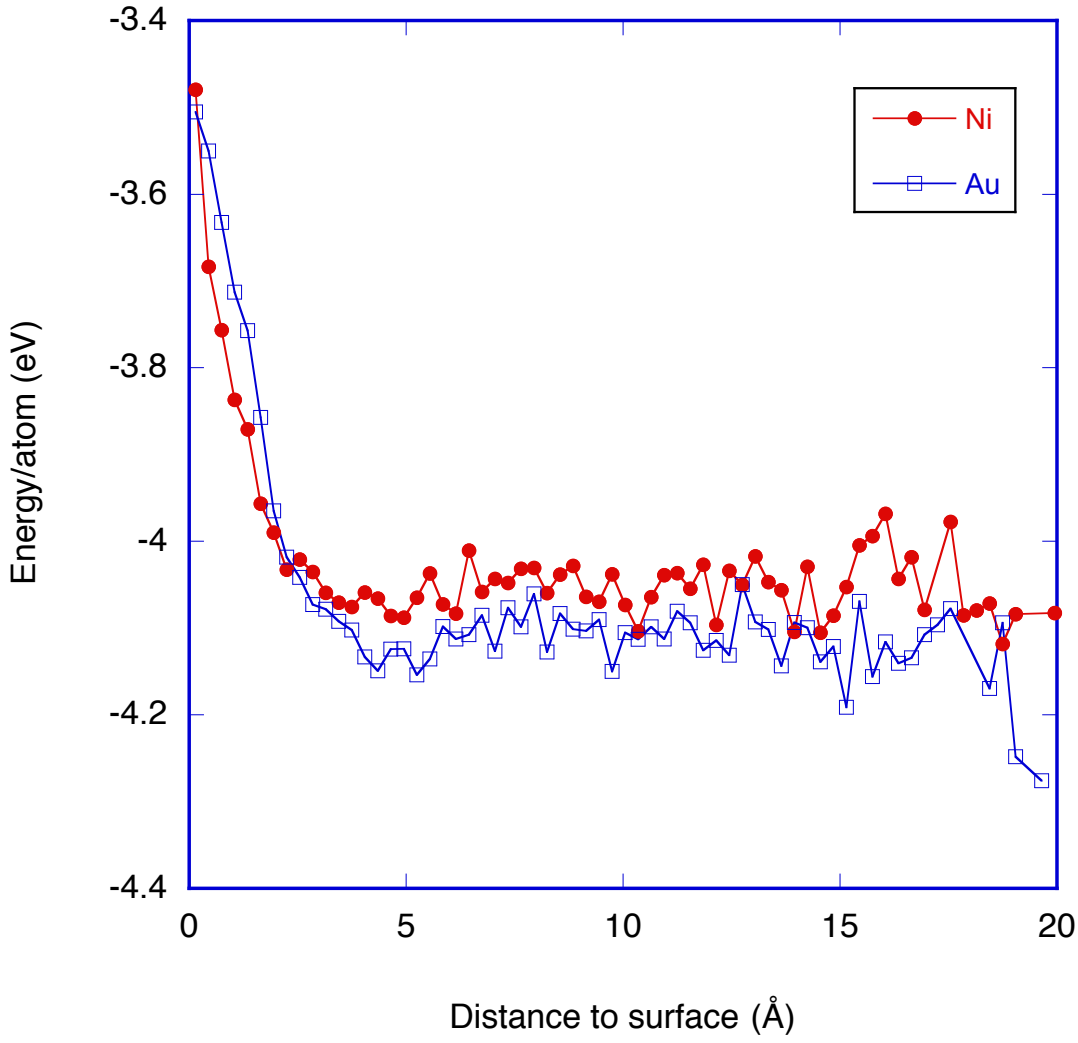

Figure 5.15: Energy per atom as a function of the distance to the nanoparticle surface for both Ni (red line) and Au (blue line) cases. A binning of 0.3 Å was used.

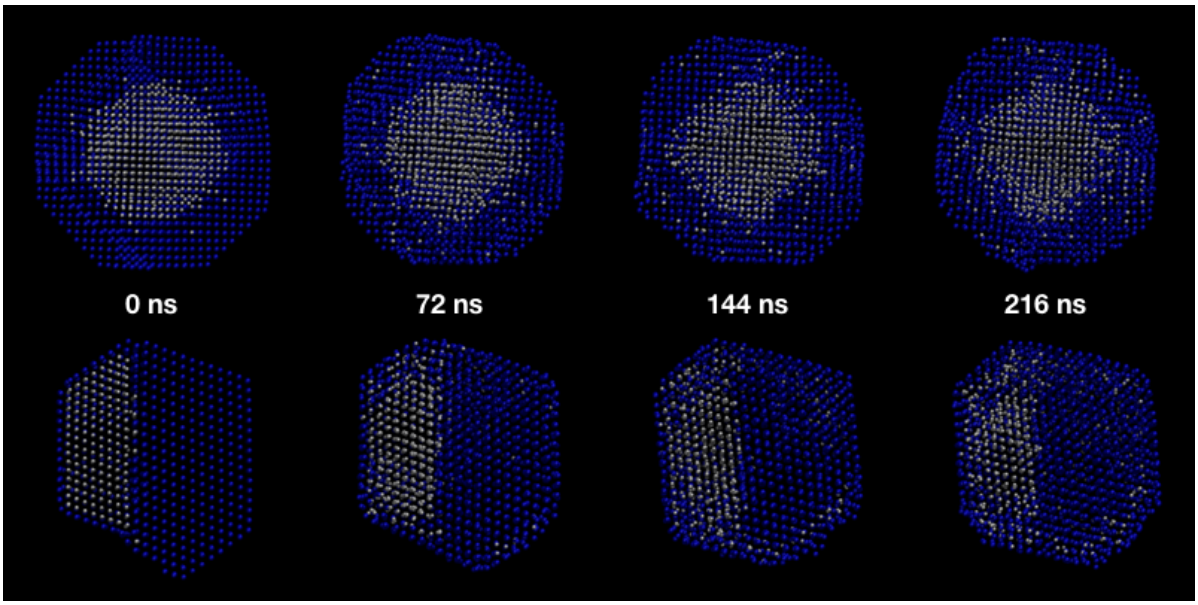

Figure 5.16: Snapshots showing the different diffusion process of Ni atoms through the solid for centralized (upper panels) and decentralized (lower panels) nanoparticles at 900 K.

7 .2.4 MD Simulations on Larger Centralized and Decentralized Nanoparticles

Finally, we have repeated the simulation using the nanoparticles composed by 6266 atoms. Our calculations provided values of −24849.154, −24847.141, and −24901.512 eV for random, centralized, and decentralized arrangements of the Ni core. Hence, agreeing well with experimental observations, the decentralized nanoparticle is the most stable. Analysing the behaviour of centralized and decentralized nanoparticles as a function of temperature, the most interesting different was found in the diffusion of Ni atoms trough the solid at a temperature of 900 K. As can be observed in Figure 5.16, the nickel atoms diffuse through the gold solid towards the subsurface region in the centralized nanoparticle but not in the decentralized one. In the latter case, the diffusion of Ni atoms is via the Ni core itself. The different behaviour can be understood by considering the tendency of the nickel atoms to be located in the subsurface region of the nanoparticle. For the case of the decentralized particle, the nickel atoms are already in contact with this sub-surface area and, then, they diffuse primarily throughout the area. Contrarily, the centralized nanoparticle needs to diffuse through the bulk of the gold phase to reach the sub-surface region. A similar phenomenon can be observed for the smaller nanoparticles considered in previous sections but it is less evident because

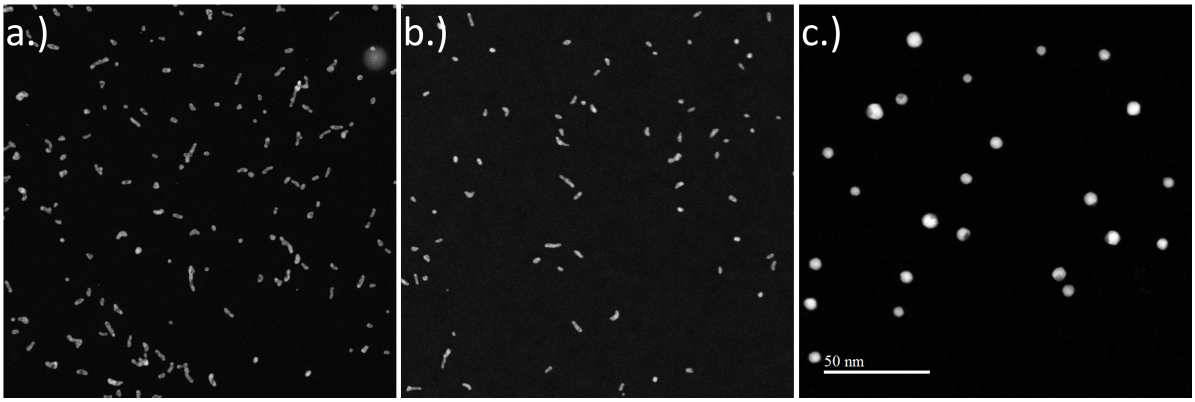

Figure 5.17: Overview of the three starting configurations at $T_0 = 300$ K. a.) centralized, b.) spinodal decomposed, c.) partially decentralized.

of the spherical shape of the particles and the larger ratio between the sub-surface area and the gold bulk phase.

7 .3 Particle Overview Scan

The particles synthesized with the helium droplet approach were log-normally distributed with an average diameter of 6.2 ± 1.3 nm. An overview at room temperature T_0 is depicted in Fig. 5.17.

7 .4 Electron Beam Damage - Decentralization

We note that demixing is not only limited to temperatures close to the melting point, but can be triggered also at lower temperatures already if longer electron beam exposure or higher electron energies are applied. Obviously, the TEM investigation itself can enhance the observed diffusion processes. Taking advantage of this influence, these intriguing demixing effects can be be studied at arbitrary time scales (see Fig. 5.18).

7 .5 Calphad

We observed, that starting at 300°C the clusters undergo a transition from separated to alloyed clusters. The temperature necessary to form an alloy is reduced in comparison the bulk alloying temperatures. One possible way to describe this phenomena of reduced alloying as well as melting temperature is the CALPHAD method. This method is based on the reduction of Gibbs free energy as a consequence of increasing surface to size effects.

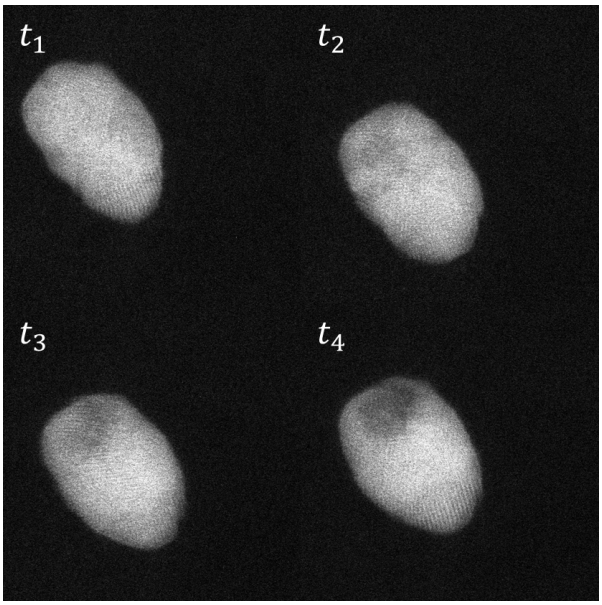

Figure 5.18: Electron beam induced dexmixing. A total dose dose of $1.5 \cdot 10^{0}$ electrons was necassary at 700 K to fully demix the cluster.

We also note that the reduced melting temperatures for NPs of various sizes in Figure 124 correlates very well with that calculated via MD simulations for one NP of diameter close to 5 nm (about 1035 K, see section 1.4 above).

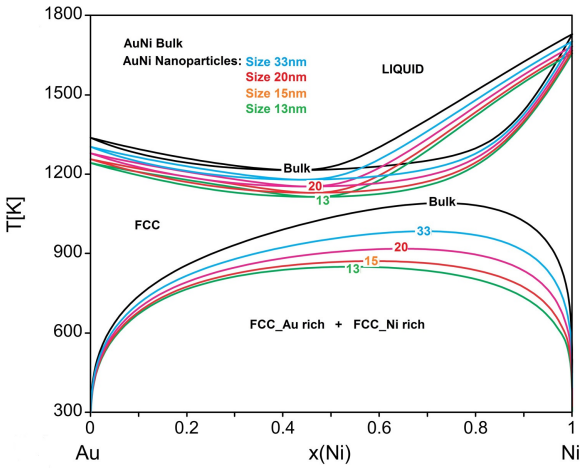

Figure 5.19: Diagram showing the reduced alloying and melting temperatures calculated with the CALPHAD method from Ref. 124.

Chapter 6

Oxygen Induced Structural Inversion of Ni–Au

This chapter corresponds to the publication
"Stability of Core–Shell Nanoparticles for Catalysis at Elevated Temperatures: Structural Inversion in the Ni–Au System Observed at Atomic Resolution"
by **Martin Schnedlitz**, Maximilian Lasserus, Ralf Meyer, Daniel Knez, Ferdinand Hofer, Wolfgang E. Ernst and Andreas W. Hauser; *Chemistry of Materials*, **30 (3)**, 1113-1120 (2018).

The author of this thesis was responsible for:

- performing the nanoparticle synthesis
- interpretation of the results
- author of the publication

The contributions of the co-authors are listed below:

- M. Lasserus: assistance in the synthesis of the nanoparticles
- R. Meyer: performing the DFT calculations
- D. Knez: operating the transmission electron microscope and interpretation of the results
- F. Hofer: microscopy supervision

- W. E. Ernst: supervision, editing
- A. W. Hauser: supervision, editing, interpretation, funding

1 Abstract

We present *in situ* transmission electron microscopy (TEM) studies of nanoscale Ni-Au core-shell particles on heatable TEM grids. The bimetallic clusters, grown fully inert within superfluid helium nanodroplets to avoid any template or solvent effects, are deposited on amorphous carbon, and monitored through a heating cycle from room temperature to 400 °C and subsequent cooling. Diffusion processes, known to impair the catalytic activities of core-shell structures, are studied as a function of the temperature and quantified through fits of a temperature-dependent diffusion constant directly derived from the experiment. After cooling, spatially resolved EDX and EELS measurements prove the inversion of the core-shell structure from Ni-Au to Au-Ni. Furthermore, a strong oxidation of the now exposed Ni shell is observed in the latter case. In combination with theoretical studies employing density functional theory, we analyze the influence of oxygen on the observed intermetallic diffusion.

2 Introduction

Bimetallic nanoclusters have received increased attention due to their unique physical properties and their additional degrees of freedom at the nanoscale: Besides the actual composition, the size, the morphology, and the ordering of the particles can be tuned. The potential applications for these materials cover a broad range from optics [13, 64, 147, 156] and catalysis[20, 46, 146] to electronics[126, 128] and medicine.[145] Magnetic noble metal core-shell particles are particularly interesting: The magnetic metal core provides a high magnetic moment suited for medical applications such as DNA separation, drug delivery[127] and magnetic resonance imaging enhancement.[43] However, small particles consisting of pure magnetic elements such as Fe, Co and Ni are easily oxidized due to the large ratio of surface to volume, a process which disables most of their magnetic properties. Oxidation can be avoided by an additional coating with a noble metal, leading to a core-shell type structure. Au stands out in this regard due to its unique optical properties[33] and its ability to adsorb biomolecules.[87] All these attributes make the core-shell system Ni-Au a good candidate for the development of biosensors.[63]

From a catalysis point of view, bimetallic nanoparticles offer tunable reactivities, bifunctional activity, and additional stabilization of sensitive catalysts via a co-metal partner.[5, 24, 90, 107] Ni-Au core-shell nanoparticles, also in combination with Pt,

have been recently suggested as catalysts for the hydrogen evolution[88] as well as the oxygen reduction reaction[8]. In general, special interest lies in the combination of metals with significantly different chemical properties. However, the expected flexibility in the adjustment of catalytically relevant parameters comes at the cost of a more difficult solution-based synthesis due to large differences in the reduction potentials and miscibility problems at low temperatures.[153, 154] Therefore, several synthesis methods for magnetic-noble bimetallic nanoparticles have been developed.

Broyer *et al.* utilize a non-equilibrium process for the synthesis of bimetallic particles from immiscible metals. The metals (Co and Au) formed core shell clusters after an annealing treatment with a femtosecond laser[16]. A solution-based synthesis via galvanic exchange has been presented by the group of O'Connor, where Fe-Au nanoparticles are created by the addition of $HAuCl_4$ solution to Fe colloids.[12] A similar principle has been used for other combinations as well,[85, 129] aiming at the production of yolk/shell nanospheres or nanorattles for medical applications such as biological sensing and gene delivery.

An alternative approach for synthesizing core-shell structures is presented in this paper. It is based on a controlled pickup of metal atoms from vapor via a beam of superfluid helium droplets. Helium nanodroplets (He_N) were extensively utilized as superfluid, inert environments for the spectroscopy of atoms, molecules and small clusters.[21, 135, 136] The extremely low temperature of 0.37 K [58] and the possibility of a sequential doping with different metals make helium nanodroplets a unique tool for the synthesis of mixed-metallic nanoparticles. Particularly interesting is the ability of this technique to synthesize core-shell structures in metastable geometries. Due to the low temperature of the droplets and their ability to effectively dissipate the binding energies released during the formation of metallic bonds, it is possible to synthesize cluster structures in geometries far from the global minimum, protected from gas phase reactions, and without templates or solvents affecting their growth.

In this article, we take advantage of the intrinsic inertness by synthesizing Ni-Au nanoparticles with a core-shell structure, which is the expected most stable configuration due to the higher Ni-Ni bond strength in comparison to the Au-Au interaction. Intriguingly, these clusters show a clear tendency to core-shell inversion after a full circle of heating and subsequent cooling. Therefore, we investigate the 'in situ' impact of oxygen, an inevitable trace gas the clusters are exposed to during transmission electron microscopy (TEM) measurements, on the phase transition from Ni-Au to Au-Ni core-shell clusters. Temperature-programmed, high resolution TEM studies are accompanied

by a computational modeling approach with the aim to identify the effect of O_2 adsorption on the observed phase transition. We further apply a recently developed imaging processing technique for the extraction of the temperature-dependent diffusion constant of a given metal combination directly from HAADF (High-angle annular dark-field) observations. Our experimental efforts are complemented by a series of density functional theory calculations on smaller, finite model systems.

The impact of oxygen or reactive oxygen species on the structure of bimetallic nanoparticles is highly relevant for their application as oxidation catalysts since oxygen adsorption and cleavage are important steps in the corresponding reaction pathways. For the oxidation of CO, special focus has been set on combinations of group 12 and 13 elements, where a significant influence of adsorbates onto local atomic composition and surface structure has been reported.[10, 154] Observed phenomena such as phase separation and adsorption-driven surface segregation have been suggested as additional tools for the synthesis of catalysts via dynamical engineering. It is our aim to shed more light on these processes induced by the adsorption of oxygen and their influence on the cluster structure at various temperatures.

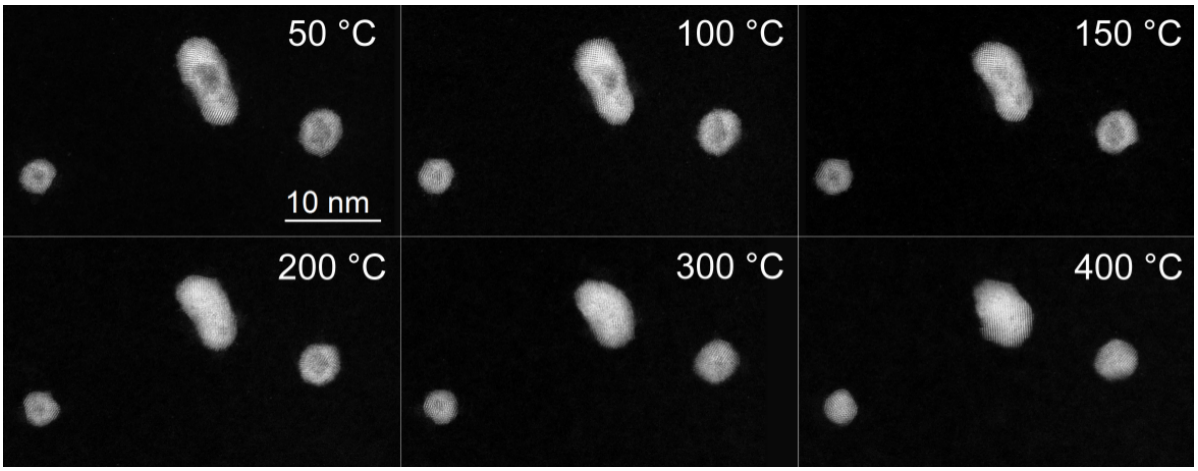

Figure 6.1: HAADF images Ni-Au core-shell clusters deposition on TEM grid for different temperatures. For room temperature the Nickel core is visible as a dark zone inside the clusters. Upon heating, the contrast between the inner cores and outer shells of all the three clusters disappears successively. At 400°C a complete mixing of Au and Ni is observed for all clusters.

3 Results and Discussion

Recently, we could demonstrate that Ni clusters oxidize during TEM measurements as a consequence of being exposed to small traces of oxygen produced by the electron beam.[119] This problem is intrinsic to any TEM treatment where a contamination with water cannot be avoided.[70] However, making the inevitable oxidation part of the actual experiment, we take advantage of this phenomenon to test the effectivity of a passivation of the reactive Ni particles by a protective shell of gold atoms. Details of our He-mediated synthesis of bimetallic Ni-Au core-shell nanoparticles are given in Section 5 . Choosing a dotation ratio of approximately 70 at.% Au and 30 at.% Ni, and under the parameter settings mentioned in Section 5 , we are able to produce nanoparticles in a size range of approximately 2 to 10 nm and a fully gold-covered nickel core. The nanoparticles are then deposited on heatable substrates of amorphous carbon. The initial configuration of these core-shell clusters is illustrated in Fig. 6.1. Due to the large difference in Z-contrast between nickel and gold the dark nickel core can be clearly distinguished from the protective bright gold shell in the HAADF images. Obviously, the passivating shell creates a barrier for a direct oxidation of the Ni core. On the other hand, the chemical properties of a gold shell will deviate from those of a pure gold nanoparticle of comparable size due to differences in the geometry and in the electronic structure, an aspect which is crucial to the idea of catalyst tuning: The physical and chemical properties of a given bimetallic nanoparticle will depend on its atomic structure as well as the ratio of metallic elements, which opens new routes for further catalyst design.

In order to obtain a detailed description of the geometry changes with temperature we employ a recently introduced image processing technique.[80] Details of the method are provided in the Supporting Information. In brief, a relation between spherically symmetric intensity profiles of the nanoparticles, taken directly from HAADF recordings at various temperatures, and the diffusion constant $D(T)$ as a function of temperature can be found. The initial, radial density distributions of both elements in a given bimetallic particle, $\rho_{\mathrm{Ni}}(r,t=0)$ and $\rho_{\mathrm{Au}}(r,t=0)$, can be derived from HAADF images taken at room temperature. Changes in these elemental density profiles over time are described by the spherical Einstein diffusion equation,

$$\frac{\partial \rho_i}{\partial t} = \frac{\partial D}{\partial r}\frac{\partial \rho_i}{\partial r} + \frac{2D}{r}\frac{\partial \rho_i}{\partial r} + D\frac{\partial^2 \rho_i}{\partial r^2}, \tag{6.1}$$

with D as a temperature-dependent diffusion constant for Ni in Au, a crucial parameter

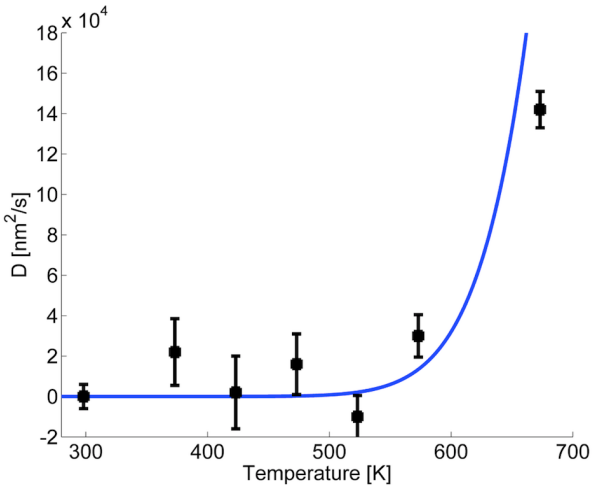

Figure 6.2: Diffusion constant of Ni-Au core-shell clusters as a function of the temperature. The black data points are derived from HAADF measurements, using a fit of the profile according to Equation 6.6. An exponential fit is plotted in blue.

for the overall diffusion progress. Equation 6.6 can be solved via a finite differences approach for any D, with the obtained solutions $\rho_i(r,t)$, $i = \{\text{Ni,Au}\}$ describing the diffusion progress of the core-shell clusters in time. However, since the real diffusion behavior is precisely known from our *in situ* heating experiments, the simulated diffusion progress can be brought to full agreement with the experimental observation via a temperature-dependent adjustment of the diffusion constant D. Therefore, inspired by the temperature behavior of the diffusion constant for the bulk, an exponential dependence of the form

$$D(T) = D_0 \exp\left(-\frac{E^\ddagger}{RT}\right) \tag{6.2}$$

is fitted to the data (see Fig. 6.2), with D_0 being the corresponding bulk diffusion constant for the Ni-Au system ($D_0 = 0.034$ cm^2/s)[31], R as the ideal gas constant, and the energy barrier $E^\ddagger$ as the only fitting parameter. From this fit we obtain a barrier height of $E^\ddagger = (0.96 \pm 0.12)$ eV for Ni atoms to migrate through the Au shell.

Structural rearrangements due to the impact of oxidation can be nicely tracked via element-specific measurements such as Electron Energy Loss Spectroscopy (EELS) and Energy-Dispersive X-ray spectroscopy (EDX). These techniques allow us to explore particle compositions before, during, and after a specific temperature-programmed treatment. Initially, at room temperature, all observed core-shell clusters show a Ni-core

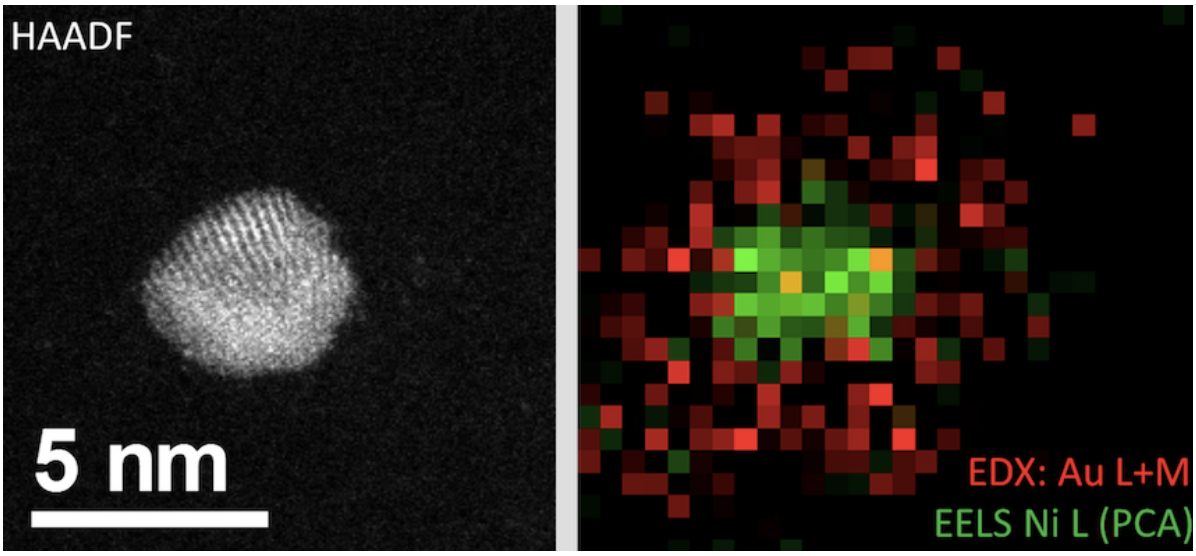

Figure 6.3: Ni-Au particle before heating. Left: HAADF scan. Right: Elemental mapping via a combination of EELS (for the detection of Ni) and EDX (for the mapping of Au). Approximately 400 Ni atoms are embedded in a shell containing roughly 1500 Au atoms.

embedded in a Au-shell (see Fig. 6.3). However, space resolved EELS and EDX measurements during heating reveal well-defined redistribution tendencies for the two elements. Fig. 6.4 shows the elemental distributions derived from spatially resolved mass spectra after a full cycle of heating and subsequent cooling. While simple HAADF contrast techniques would make the heated clusters look homogeneously mixed, an elemental analysis proves the migration of Ni atoms to the cluster surface. Furthermore, the spatial distribution of oxygen is in perfect agreement with the Ni signal. This suggests that the nickel atoms diffuse to the surface of the Ni-Au cluster and undergo an immediate oxidation as described within the framework of Cabrera-Mott oxidation theory.[70] However, no indication of oxidized Ni is measured as long as the Au shell is found intact, which supports the claim of an effective passivation of Ni for the chosen Ni to Au ratio of 3:7. Also, note that the signal of Ni and O is much stronger at particle boundaries, where larger amounts of NiO are exposed to the electron beam of the microscope due to the inevitable projective character of a two-dimensional measurement. As a consequence, the inversion of the shell structure seems to be triggered by an increased probability of finding Ni in regions near the surface, making this process dependent on the temperature but also on surface adsorbates and their impact on the surface diffusion of Ni. Besides this obvious inversion of the core-shell structure at higher temperatures, with NiO now covering an Au core, it is also visible that there is not enough Ni in the mixture to

provide a complete coverage of the core.

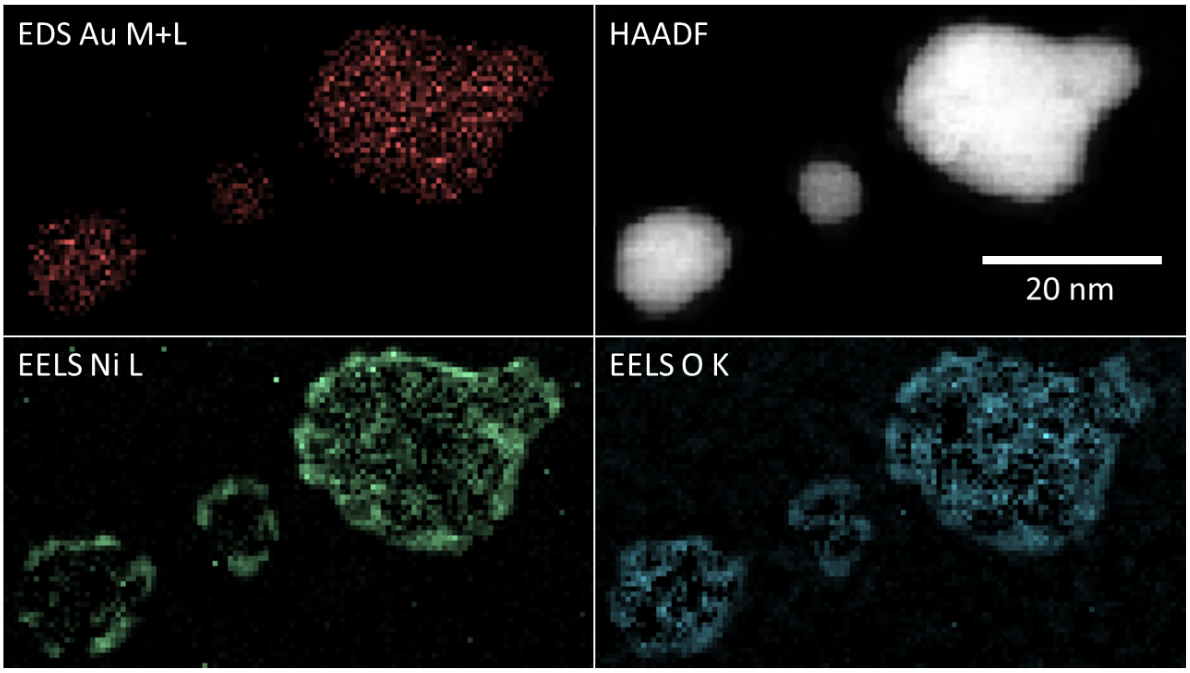

Figure 6.4: EELS and EDX measurements of the same Ni-Au metal particle after a full cycle of heating and subsequent cooling. The HAADF image is shown in the right upper corner. The left upper image shows an EDX spectrum for M+L-shell transitions of Au. The lower images present EELS data for elemental Ni and O, respectively. Note the spatial overlap of the Ni and O distribution, which gives a particularly strong signal at the contour lines of each particle, clearly indicating localization at the cluster surface.

In the next step, this interesting experimental finding of an inversion of the core-shell structure is investigated in more detail via density functional theory. A quantum-chemical approach has been favored over a force field ansatz in order to obtain a more realistic description of single-atom diffusion processes. According to the most abundant particle geometries in the TEM images, the calculations are focused on icosahedral and fcc clusters. The $NiAu_{54}$ system, composed of a single nickel atom surrounded by two icosahedral/fcc shells of gold atoms, is chosen for two reasons. First, it serves as a model system resembling the geometric structures found in the TEM images, with a nickel core of a few 100 atoms covered by a shell of approximately two layers of gold. Second, the inclusion of a single Ni atom only reduces the configurational space significantly that has to be covered by the calculations. The resulting fcc clusters are terminated by (100) and (111) faces. $NiAu_{12}$, the smallest possible icosahedral system, cannot be used as a model for larger core-shell clusters as surface effects completely dominate its behavior.

For example, it has been shown that this minimal system favors a flat geometry instead of a spherical shape. [130] The $NiAu_{54}$ system, on the other hand, is stable in its Ni-centered structure and allows to distinguish between a surface and subsurface position of the Ni atom. However, additional benchmark DFT calculations on larger systems ($NiAu_{146}$ and $Ni_{13}Au_{134}$) have been performed as well in order to justify this convenient simplification; see the supplementary information for details.

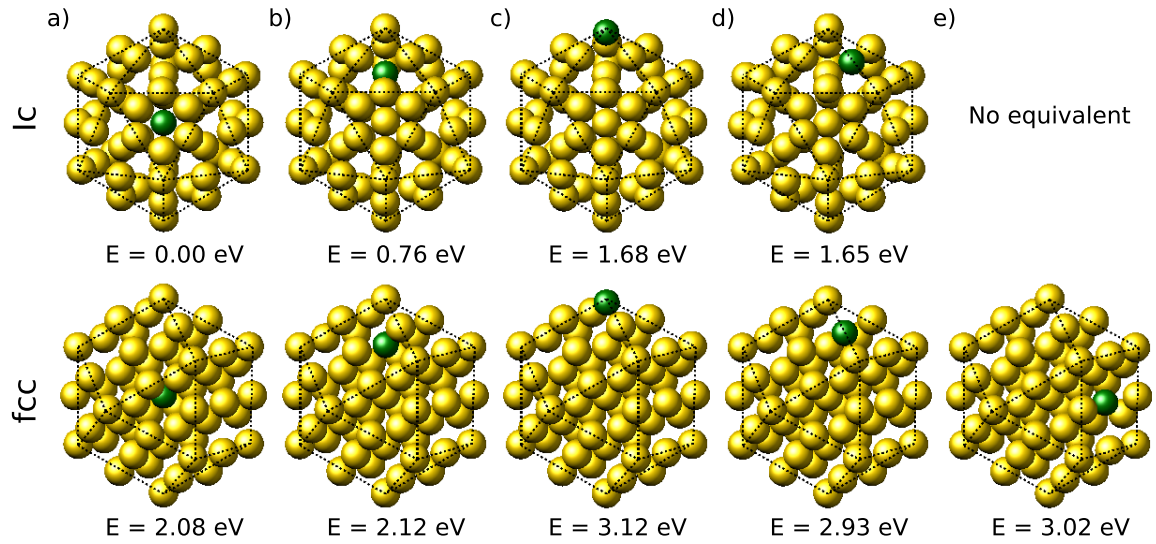

Figure 6.5: Relative DFT energy differences for various positions of the Ni atom in unsupported $NiAu_{54}$ icosahedral (top row) and fcc (bottom row) bimetallic cluster models. For more details, see text.

To determine the energetically most favorable configuration, the $NiAu_{54}$ cluster geometry is first optimized for five different positions of the Ni atom as depicted in Fig. 6.5: centered position (a), subsurface position (b), surface corner position (c), surface edge position (d), and, in the case of fcc, also a centered surface position on the (100) face (e). For the given cluster size an icosahedral shape is energetically most favorable. Nickel positions within the cluster also lead to lower energies compared to surface positions. Noteable is the remarkable energy difference between the centered and the subsurface position for nickel in the icosahedral cluster. This is consistent with the embedded atom model (EAM)-based calculations of Bochicchio and Ferrando [15], who investigated the core-shell configurations of various weakly miscible systems. They found that the embedding of a smaller atom at the center of an icosahedral cluster allows a release of the high strain at the central site. They note, however, that this is unique to the icosahedral structure and that in fcc-structured and decahedral clusters subsurface positions are

typically favored. The favoring of fcc subsurface positions is also confirmed by DFT-based investigations of Tenney *et al.* [130] on fcc-structured core-shell Ni-Au clusters. Furthermore, the preferred placement of small impurities in fcc clusters is known to be size- and facet-dependent.[78, 106] In our calculations, subsurface positions lead to a 0.04 eV energy penalty relative to the centered position. This can be attributed to the smaller size of the clusters in our calculations in comparison to other studies.

In order to investigate the influence of oxygen on the core-shell inversion process we repeat the structure studies of above for the $NiAu_{54}$ cluster, but this time with a single oxygen molecule adsorbed to the cluster surface. Although it can be assumed that more reactive oxygen species are present in the experiment due to the electron energy deposited during TEM examination, the impact of molecular oxygen is most relevant for oxidation processes at ambient temperature and pressure conditions in future applications of bimetallic nanoparticles. As can be seen from Fig. 6.6, the adsorbed oxygen molecule causes lower relative energies for nickel at the surfaces positions, which indicates increased adsorption capabilities for inverted clusters. On the other hand, this also suggests that core-shell inversion becomes an exothermal reaction upon oxygen adsorption, only hindered by the remaining reaction barrier for nickel diffusion through a shell of gold. In the case of fcc clusters, all surface positions are favored over positions within the cluster after the absorption. In the case of icosahedral clusters, the centered position remains the energetically most favorable position, but surface positions are again always favored over a subsurface position. A similar stabilizing effect of surface positions was found by Tenney *et al.* for the adsorption of CO onto Ni-Au clusters. [130]

The second set of calculations on the icosahedral $NiAu_{54}$ system is dedicated to reaction kinetics, as it explores the role of oxygen adsorption on the diffusion barrier of nickel through gold. Climbing image nudged elastic band calculations (CI-NEB) [61, 65, 98] are used to determine the energy barrier for the diffusion process from the subsurface position to the surface corner position with and without the presence of molecular oxygen. All paths are optimized to an accuracy of 0.1 eV/Å.

Fig. 6.7 shows the resulting reaction paths for icosahedral $NiAu_{54}$. The calculated energy barrier without oxygen is 1.67 eV. This barrier is reduced to 1.17 eV after the adsorption of molecular oxygen. This value is in remarkably good agreement with the experimental estimate of 0.96 eV based on the HAADF measurements of the radial density profiles during a heating cycle. We note that this plotted reaction pathway is just one among numerous possibilities of surface diffusion, and although the selected pathway shows the lowest barrier we could find, a more representative estimate would

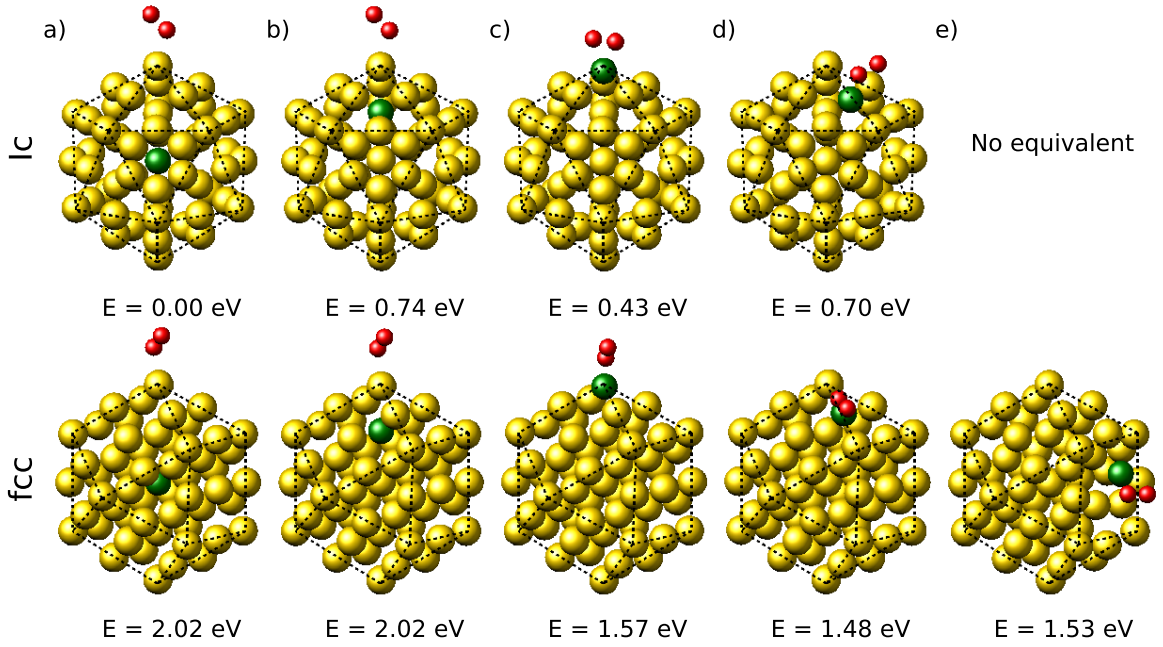

Figure 6.6: Relative DFT energy differences for various positions of the Ni atom in unsupported $NiAu_{54}$ icosahedral (top row) and fcc bimetallic cluster models (bottom row) after the adsorption of a single oxygen molecule.

have to be based on statistical approaches such as Monte Carlo sampling, which is extremely costly for energy and gradient evaluations at the necessary level of theory. However, the qualitative impact of oxygen is a general feature and can be assumed to show the same tendency for all Ni diffusion pathways possible.

4 Conclusions

The temperature-dependent structural inversion of bimetallic core-shell systems of Ni and Au is carefully investigated and visualized via TEM imaging of the diffusion process *in situ* on a heated carbon substrate. First, metastable Ni-Au core-shell particles are synthesized in superfluid He nanodroplets and deposited on heatable TEM grids. Different cluster sizes are studied and the radial intensity profiles of HAADF images are investigated in order to explore the limitations of a noble-metal passivation of a reactive metal. A temperature-dependent diffusion constant is derived from cluster density profiles and an activation energy for the surface emergence of Ni is obtained. This parameter is identified as a convenient indicator for the onset of intermetallic mixing. Additionally, the diffusion behavior of the Ni-Au system is further analyzed in the context of surface

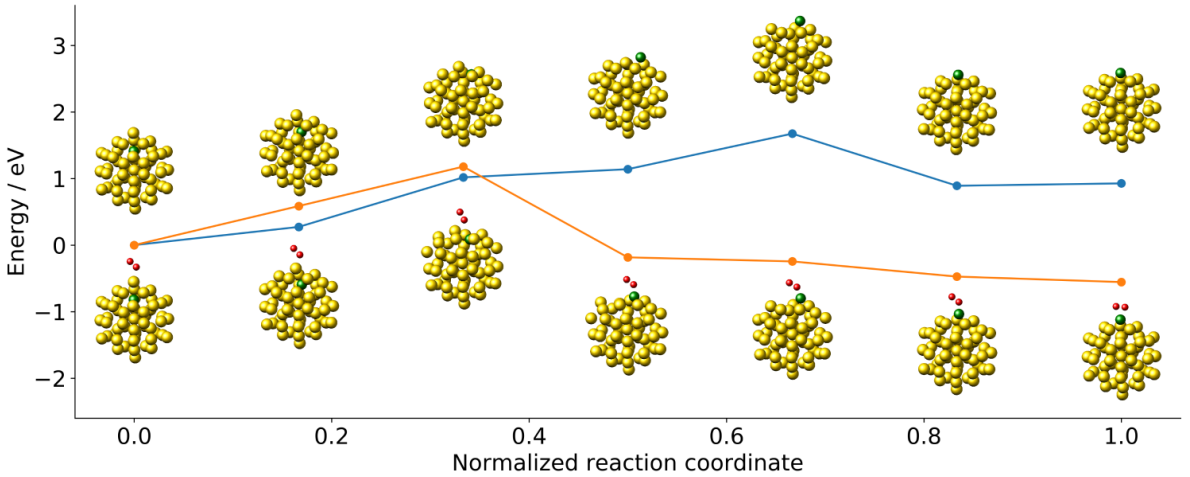

Figure 6.7: Reaction paths describing the diffusion of a single Ni atom in an unsupported icosahedral gold cluster ($NiAu_{54}$), indicating the transition from structure b) to c) in Figures 6.5 and 6.6, i.e. the subsurface to surface migration with (lower path, red) and without (upper path, blue) the presence of molecular oxygen.

oxidation. Element-specific EELS and EDX measurements reveal an oxidation of the Ni atoms after diffusion to the particle surface. The obtained structure is much more stable, rendering this structural inversion of the core-shell particle irreversible. The experimental outcome further suggests that the mere presence of molecular oxygen on the cluster surface acts as a driving mechanism for Ni diffusion to the surface.

The underlying assumption that the physisorption of molecular oxygen effectively reduces the energy barrier for Ni diffusion is supported by density functional theory calculations on a core-shell model. The energetically most favorable position of the Ni-Au system was determined for $NiAu_{54}$ in icosahedral as well as fcc structure. In the absence of oxygen, a centered Ni atom within a Au_{54} shell is the energetically most stable configuration, which is consistent with the calculations of Bochicchio and Ferrando. However, when oxygen is present, the total energy can be reduced by the diffusion of the Ni atom to the surface, where it provides a preferred physisorption site for the O_2 molecule. The energy barrier for this surface migration of the Ni atom is estimated via nudged elastic band calculations in both cases. The reaction pathway starts at a subsurface position of the Ni atom and ends at a cornered surface position with or without an adsorbed oxygen molecule in its vicinity. Oxygen presence reduces the energy barrier (1.67 eV) by approximately 0.5 eV, which is in good agreement with the experimentally determined barrier of 0.96 eV. The subsequent, inevitable full oxidation of diffused Ni on the cluster

surface would drive this exothermic reaction further downhill, which explains the final 'locking' in an inverted core-shell structure. However, note that the initial oxidation of Ni is not the cause but the consequence of an enhanced diffusion of subsurface Ni atoms which occurs even upon physisorption of molecular oxygen.

To summarize, theory as well as experiment lead to the conclusion that the Ni-Au core-shell system is the energetically most stable configuration during synthesis within the He droplet. However, when oxygen presence is inevitable during TEM measurements, an inverted Au-Ni core-shell system becomes thermodynamically preferred at elevated temperatures, even before a full oxidation of the reactive metal takes place. In terms of reaction kinetics, the process of Ni diffusion to the surface is catalyzed by the mere presence of oxygen. In general, for future applications of bimetallic nanoparticles in this size regime as catalysts it needs to be taken into consideration that gas adsorption onto the protective noble metal shell can destabilize the core-shell structure by an enhancement of intermetallic diffusion.

5 Materials and Methods

Nanoparticle Synthesis. High purity helium (grade 6 = 99.9999%) is expanded through a 5 ¯m nozzle at temperatures below 8 K. Expansion and further collimation by a 400 ¯m skimmer results in the formation of a beam of highly pure helium droplets serving as 'nanolabs' for the synthesis of metallic clusters. The average droplet size can be adjusted via the nozzle temperature and the stagnation pressure (20 bar for these experiments). In this work, the conditions were chosen as $T_{\text{nozzle}} = [5.4, 6.7, 8]\,K$, which corresponds to an average amount of $N_{\text{He}} \approx [10^{10}, 5 \cdot 10^{7}, 5 \cdot 10^{6}]$ helium atoms per droplet.[51] The nanodroplets pass through two separated pickup cells containing the desired metal species. The vapor pressure is controlled independently by the temperature in each evaporation cell, which in turn changes the amount of metal atoms picked up by the helium droplets in each section. In the first cell, single metal clusters of desired size are formed. In the second cell, they become subsequently encapsulated by further pickup of the second metal species. This way, the superfluid, inert helium droplet environment enables the synthesis of arbitrary core-shell structures via sequential doping.[57] We note that nanoparticle synthesis becomes strongly affected by the phenomenon of quantum vortices[29, 105] if the He nanodroplets are chosen too large, which leads to the formation of more elongated structures.[52, 133, 141] Therefore, a safe regime below a droplet size of 10^7 atoms has been chosen for this study. The release of

kinetic and binding energy of the metal atoms upon cluster formation leads to a partial evaporation of the helium droplet, which is monitored via a residual gas analyzer (Balzer QMA 200/ QME 200). Finally, the beam is again collimated by a 2 mm skimmer before entering the measurement chamber, where the clusters are deposited on a heatable TEM grid (DENSsolutions Nano-Chip XT carbon) in a soft-landing process where the excess helium is vaporized upon impact.[4, 27, 134] For a more detailed description of the experimental setup we refer to previous works.[132, 133, 142]

Characterization. High angular annular dark-field images of the temperature-dependent diffusion and alloying process are recorded with a probe-corrected FEI Titan^3 G2 60-300. Material compositions and their spatial distribution are determined with a four-quadrant energy-dispersive X-ray spectroscopy detector (EDX) and a Gatan Quantum energy filter for electron energy loss spectroscopy (EELS). The carbon TEM grids can be heated from room temperature up to $\approx 1300\,^{\circ}\mathrm{C}$ with maximum heating rates of $200\,^{\circ}\mathrm{C/ms}$.

Computational details. Scalar-relativistic density functional theory calculations on the small $NiAu_{54}$ system are carried out using the Quantum Espresso suite of programmes. [48] The PBE exchange-correlation functional [108] is used in combination with projected-augmented-wave (PAW) pseudopotentials [14][73] to find the energetically most favorable configurations of unsupported clusters. A 45 x 45 x 45 Bohr^3 supercell and a cutoff of 30 Ryd for the energy and 300 Ryd for the density are chosen. In addition, all calculations employ the smearing technique of Methfessel and Paxton [96] with a smearing parameter of 0.01 Ryd. All geometries are optimized using the BFGS-algorithm [18][41][49][121] with thresholds of 10^{-4} Ryd and 10^{-3} Ryd/Bohr for energies and forces, respectively. A series of benchmark calculations including Grimme's D3 correction[54] has been performed as well in order to judge the lack of long-range dynamic correlation, a well-known weakness of local and hybrid exchange-correlation functionals. The inclusion of dispersion corrections (PBE-D3) leads to large but almost constant shifts in total energies for the relevant geometries. Therefore, relative energies are barely affected, indicating a minimal impact of dispersion interactions on the Ni propagation under study.

6 Acknowledgement

Martin Schnedlitz and Maximilian Lasserus thank Florian Lackner, Roman Messner and Alexander Schiffmann for many fruitful discussions. This research has been supported

by the Austrian Science Fund (FWF) under Grant PIR8-N34. Further support by NAWI Graz is gratefully acknowledged.

7 Supporting Information

This Supporting Information consists of three sections. In Section 7 .1, we present a more detailed description of the image-processing technique, which is used to determine the temperature- dependent diffusion constant $D(T)$. Section 7 .2 reports on a series of calculations on larger NiAu clusters in order to test the impact of Ni-Ni interactions on the outcome presented in the main article. Section 7 .3 lists all final cluster geometries obtained from DFT optimizations.

7 .1 Derivation of the diffusion constant $D(T)$

Here we present a more detailed description for the extraction of the Ni-Au temperature-dependent diffusion constant $D(T)$ out of HAADF observations. In Section "Diffusion and Alloying" of the main article we already presented a rudimentary description of the derivation of $D(T)$. Additionally, a detailed description can also be found in a previous article for the Au-Ag system.[80]

Inspired by the HAADF observations, we assume spherically symmetric Ni-Au core-shell clusters. The initial radial density profiles $\rho_{\mathrm{Ni}}(r,t=0)$ and $\rho_{\mathrm{Au}}(r,t=0)$ can be approximated by error functions using an analytical expression $d(r,R,\sigma)$:

$$d(r,R,\sigma) = \frac{1}{2}\left(\mathrm{erf}\left(\frac{r+R}{\sqrt{2}\sigma}\right) - \mathrm{erf}\left(\frac{r-R}{\sqrt{2}\sigma}\right)\right), \tag{6.3}$$

with the following definitions for Ni and Au:

$$\rho_{\mathrm{Ni}}(r,t=0) = d(r,R_{\mathrm{Ni}},\sigma), \tag{6.4}$$

$$\rho_{\mathrm{Au}}(r,t=0) = d(r,R_{\mathrm{Au}},\sigma) - d(r,R_{\mathrm{Ni}},\sigma), \tag{6.5}$$

with R_{Ni} being the Ni core radius and R_{Au} the outer Au shell radius. σ determines the slope of the profiles, which controls the density progression at the Ni-Au interface. The initial radial density profiles are plotted in Fig. 6.8.

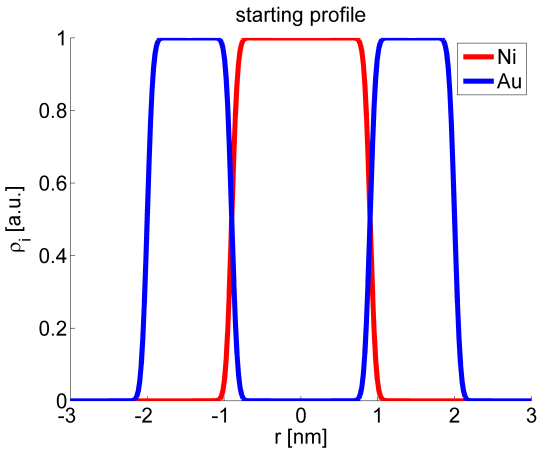

Figure 6.8: Initial radial density profiles of the Ni-Au system (see Equations 6.3-6.5)

As already mentioned in the main article, the profiles $\rho_i(r,t)$ were evolved in time using the spherical Einsteins diffusion equation,

$$\frac{\partial \rho_i}{\partial t} = \frac{\partial D}{\partial r}\frac{\partial \rho_i}{\partial r} + \frac{2D}{r}\frac{\partial \rho_i}{\partial r} + D\frac{\partial^2 \rho_i}{\partial r^2}, \tag{6.6}$$

with the diffusion constant D. In order to describe the diffusion only within the finite size cluster, D was set to be,

$$D(r) = D_0 \cdot d(r,R_{\mathrm{Au}},\tilde{\sigma}). \tag{6.7}$$

This expression for D not only limits the diffusion to take place within the cluster, but also has the advantage of having a finite derivative at $r = R_{Au}$. $\tilde{\sigma}$ describes the slope of the diffusion constant at $r = R_{Au}$.

Using the initial conditions, we were able to evolve Equation 6.6 in time via a finite differences approach. The solutions $\rho_i(r,t)$ are then combined and used to obtain a simulated intensity profile in Cartesian coordinates, with a reduced z dimension. As the intensity in HAADF recordings is proportional to the quadratic atomic charge, the different $\rho_i(r,t)$ were multiplied with Z_i^2 and finally normalized. The final normalized Cartesian intensity profiles were then compared with the measured normalized intensity profiles from HAADF recordings, using the time t as the fitting constant, which determines the progress of the diffusion. In Fig. 6.9 the measured HAADF profiles are plotted with the best fitting calculated ones.

The temperature dependence arises as $D = f(t)$. Therefore the solutions ρ_i can

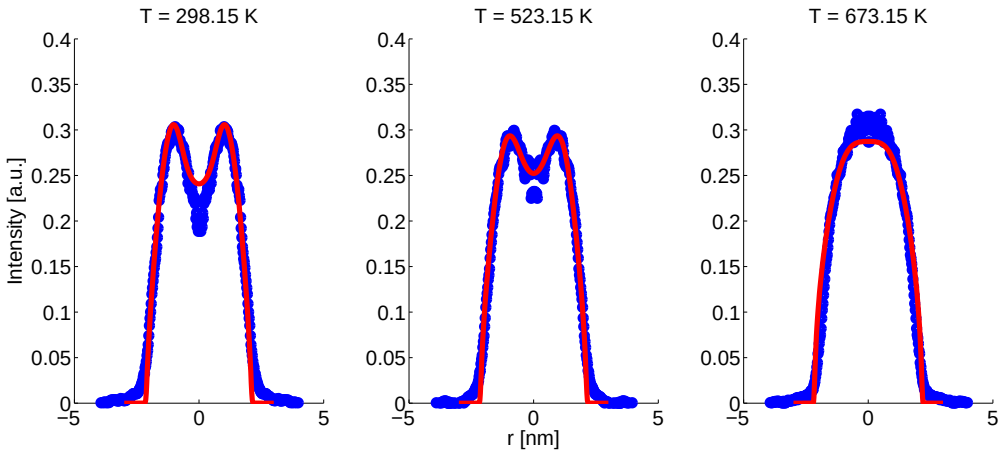

Figure 6.9: Comparison between three different HAADF intensity profiles (blue circles) and the calculated best fitting intensity profiles (red line), obtained from Equation 6.6.

be rewritten as a function of the diffusion progress $\rho_i(r,D(t)t)$. Since the temperature was kept constant for given time interval k, one can determine $D(T)$ from the progress in diffusion from one temperature step to the other. The dependence of the diffusion constant as a function of temperature is illustrated in Fig. 2 in the main article.

7 .2 DFT calculations on selected larger systems

Selected calculations from the main article are repeated for larger systems in order to verify that the $NiAu_{54}$ is a representative model. The cell dimensions are increased to 50 x 50 x 50 $Bohr^3$ in order to accommodate the 147 atom clusters.

7 .2.1 The $NiAu_{146}$ system

Calculations on the $NiAu_{146}$ system containing an additional Au shell are employed to investigate the effect of the high surface to volume ratio in smaller clusters. Figure 6.10 shows the relative energy of various positions of the Ni atom in the cluster. The relative ordering as well as energy differences of comparable structures in the $NiAu_{54}$ system are in good agreement (see main article, Figure 5). For example, the transition from the subsurface corner position (c) to the surface corner position (f), investigated via the nudged elastic band method, shows an energy difference of 0.90 eV for the icosahedral geometry and 0.96 eV for fcc in the larger $NiAu_{146}$ system. This compares well to the energy differences for $NiAu_{54}$ of 0.92 eV and 1.00 eV for icosahedral and fcc, respectively.

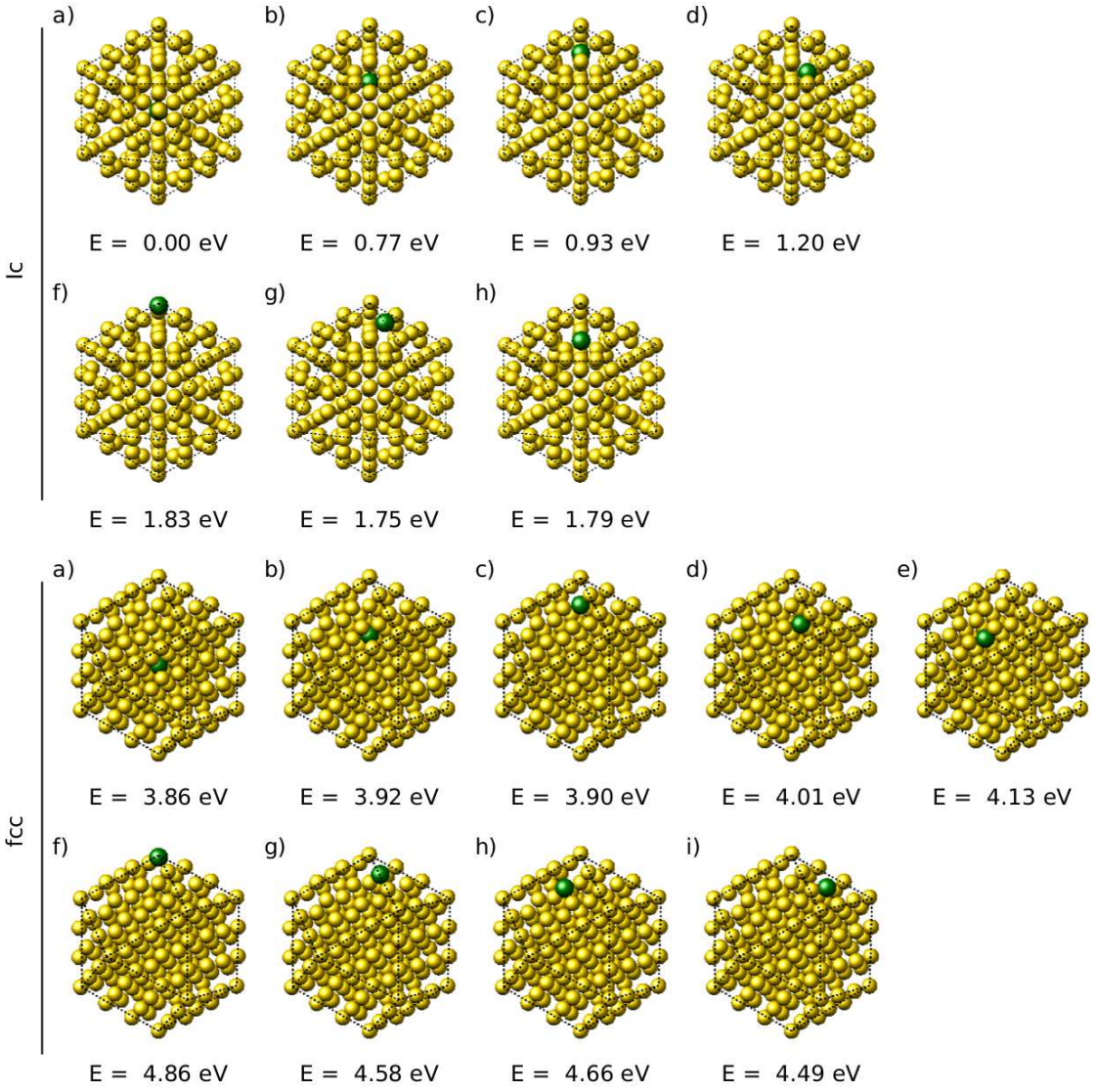

Figure 6.10: Relative DFT energy differences for various positions of the Ni atom in unsupported $NiAu_{146}$ icosahedral (top rows) and fcc (bottom rows) bimetallic clusters.

7 .2.2 The $Ni_{13}Au_{134}$ system

Calculations on a system with a larger Ni core aim to explore the role of the Ni-Ni interaction. The $Ni_{13}Au_{134}$ system consists of a small icosahedral Ni core coated with two layers of Au. Figure 6.11 shows the relative energies of selected positions of a single Ni atom after migration away from the core. The energy difference between the subsurface corner position (b) and the surface corner position (d) of 0.92 eV is again comparable

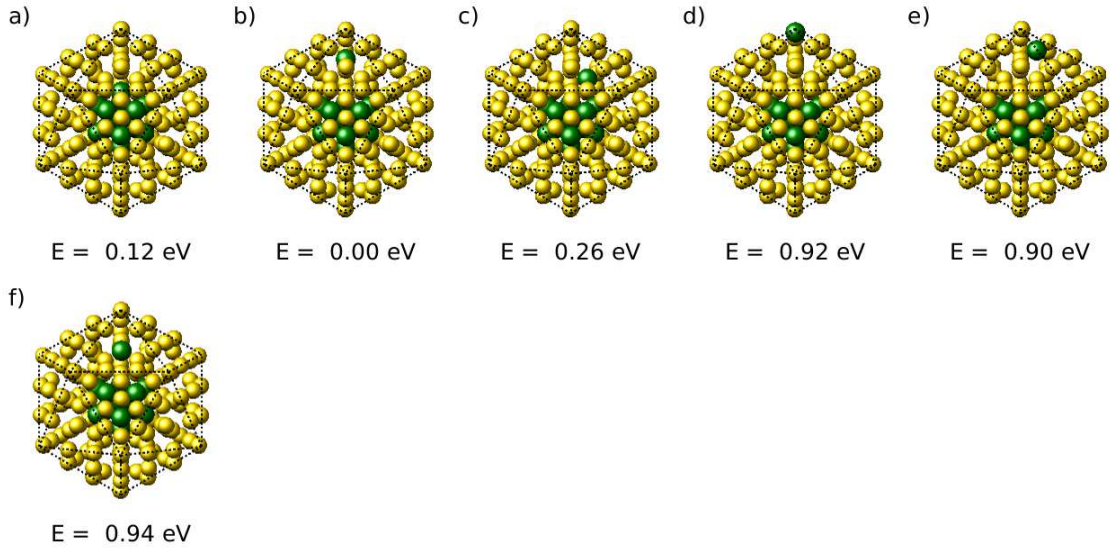

Figure 6.11: Selected relative DFT energy differences for various positions of a single Ni atom in unsupported $Ni_{13}Au_{134}$ icosahedral bimetallic clusters.

to the smaller $NiAu_{54}$ system with ΔE= 0.92 eV and the same sized $NiAu_{146}$ system without Ni-Ni interaction with ΔE= 0.90 eV. The fully centered configuration (a) is no longer the energetically most favorable geometry for a core of 13 Ni atoms surrounded by 134 Au atoms. This can be interpreted as a first effect of the morphological instability investigated by Bochicchio and Ferrando. [15]

7 .3 DFT geometries

The cartesian coordinates of all the optimized cluster geometries shown in the main article are found in the supporting information of the corresponding article "Stability of Core–Shell Nanoparticles for Catalysis at Elevated Temperatures: Structural Inversion in the Ni–Au System Observed at Atomic Resolution" by **Martin Schnedlitz**, Maximilian Lasserus, Ralf Meyer, Daniel Knez, Ferdinand Hofer, Wolfgang E. Ernst and Andreas W. Hauser; textitChemistry of Materials, **30 (3)**, 1113-1120 (2018).

Chapter 7

Summary

This thesis presents the synthesis, characterisation and study of bimetallic nanoparticles at elevated temperature. Irrespective of the future usage of bimetallic core-shell nanoparticles e.g. for medical, optical or chemical purposes, it is clear that the structural integrity of the layers, also at higher temperatures, is a knockout criterion for many planned industrial applications. Taking advantage of the He-mediated synthesis of mixed-metallic structures, it was possible to investigate solvent-free thermally induced diffusion behaviour and to interpret them with the help of computational model calculations.

In the first part of this thesis the structural stability of Fe-/Co-/Ni-Au core-shell particles is studied. It is found that even though the three core elements are very similar with regards to their atomistic properties, these differences result in entirely different restructuring phenomena at elevated temperatures. It has been found that Co has the tendency to form a decentralised cluster, Fe is fragmented into multiple single cores embedded in a Au matrix and Ni undergoes a transition towards full intermixing already at 300°C. As will be shown, these phenomena can be linked to the significant differences in vacancy formation energies which crucially determine the restructuring pathways.

The Ni-Au system has been studied in greater detail, in particular the difference in stability of a centralised and a decentralised Ni-core. The starting geometry has a tremendous impact on intermetallic diffusion behaviour as it determines the resistance against an inevitable alloying which takes place at higher temperatures. Starting at a temperature of 300°C, all initially separated structures undergo a transition towards a fully alloyed state. An analysis of structural changes via TEM imagery revealed that clusters featuring a decentralised core possess a pronounced structural integrity, which

is linked to a different diffusion behaviour. From computationally costly large-scale molecular dynamics simulations over several hundred nanoseconds it is concluded that a decentralised core affects the overall structure of the particle in a way which promotes diffusion processes along the intermetallic interface, but quenches atomic intermixing along the radial coordinate. In the concrete case, this subtle change in the diffusion mechanism leads to an extension of the alloying times by two orders of magnitude.

Furthermore, the impact of oxygen has been studied in the previous chapter about oxygen induced structural inversion of Ni-Au. The temperature-dependent structural inversion of bimetallic core-shell systems of Ni and Au is carefully investigated and visualized *in situ* via TEM imaging of the diffusion process. Element-specific EELS and EDX measurements revealed an oxidation of the Ni atoms after diffusion to the particle surface. The obtained structure is much more stable, rendering this structural inversion of the core-shell particle irreversible. The underlying assumption that the physisorption of molecular oxygen effectively reduces the energy barrier for Ni diffusion is supported by density functional theory calculations on a core-shell model. In terms of reaction kinetics, the process of Ni diffusion to the surface is catalyzed by the mere presence of oxygen.

Chapter 8

Danksagung

Ich möchte die Gelegenheit nutzen um mich an dieser Stelle bei meinen beiden Betreuern Assoc. Prof. Andreas W. Hauser und Em. Univ. Prof. Wolfgang E. Ernst für ihr Engagement und die Möglichkeit bedanken, dass ich eine Dissertation in diesem spannenden und kompetitiven Forschungsgebiet machen durfte. Ich durfte erste Schritte in die Welt der Forschung setzen und in den letzten drei Jahren den wissenschaftlichen Alltag kennenlernen. Insbesondere Andreas W. Hauser sei an dieser Stelle für seine Geduld, die anregenden Diskussionen und die nette Büronachbarschaft in dieser Zeit der Dank ausgesprochen.

Weiters möchte ich mich hier bei allen Kolleginnen und Kollegen am Institut bedanken, welche mit Rat und Tat immer zur Seite standen und mit ihrer überaus freundlichen Attitüde mir über die Jahre sehr ans Herz gewachsen sind. Allen voran sei hier mein Bürokollege und langjähriger Freund Maximilian Lasserus zu erwähnen, welcher immer für eine hitzige Diskussion zu haben war. Ebenfalls möchte ich mich für die einzigartig schöne Zusammenarbeit mit den weiteren "Helenisten", Roman Messner, Alexander Schiffmann, Thomas Jauk und Florian Lackner bedanken. Ebenfalls sei hier die freundliche und effiziente Zusammenarbeit und die Kollegschaft am gesamten Institut erwähnt. Ich möchte mich bei den Femtoleuten, den Heliumstreuern und den Theoretikern für dieses einzigartige Arbeitsklima bedanken.

Schlussendlich möchte ich auch noch meine Eltern hier erwähnen, und mich für ihre Unterstützung während meiner gesamten Studienzeit herzlich bedanken.

Appendix A

Input Codes

In this section, the input codes for the synthesis of core-shell particles in LAMMPS as well as the MATLAB code for the calculation of a size dependent phase diagram are presented.

1 Core-Shell nanoparticle formation in LAMMPS

This section contains the code used for the creation of a Ni-Au core-shell particle. It consists of two parts, the synthesis of the Ni core, followed by the synthesis of the Au shell. 900 Ni atoms are randomly placed inside a sphere with a radius of 14Å. Cooling with a Berendsen thermostat to 1 mK, subsequent heating to 900 K and final cooling to 0.4 K resulted in the formation of a Ni core. This way the Ni atoms are synthesized close to the assumed agglomeration process in a He droplet. Subsequently, the Au atoms are randomly placed around the Ni atoms and the same heating and cooling procedure is applied while keeping the Ni atomic positions fixed.

Ni creation

```
units metal
atom_style      atomic

boundary p p p

# Define system
```

```
region simul block -500. 500. -500. 500. -500. 500. units box
create_box 2 simul
mass            1 58.6934
mass            2 196.96655

pair_style      eam/alloy

pair_coeff      * * AuNi.set Ni Au

neighbor 0.5 bin
neigh_modify delay 0

#create Nickel Atoms

region          hinsert sphere 0.0 0.0 0.0 14.0 side in units box
create_atoms    1 random 900 96532156 hinsert
group           Nickel  type 1
group           ag1 region hinsert


timestep        0.001
thermo_style    one
thermo          10

# Initial low Temp. run to remove instabilities of random creation

fix             11 Nickel momentum 1 linear 1 1 1 angular
fix             2 all temp/berendsen 0.01 0.001 0.032
fix             3 all nve/limit 0.01
dump            2 all  xyz 50 Nickel_cool1.xyz.gz
run             5000
write_data      Ni_001_*.nano
undump 2
unfix  2
unfix  3
```

```
fix             2 all temp/berendsen 0.001 0.0001 0.032
fix             3 all nve
dump            2 all  xyz 50 Nickel_cool2.xyz.gz
run             5000
write_data      Ni_0001_*.nano
undump 2
unfix  2

# initial slow heating

fix             2 all temp/berendsen 0.0001 0.4 0.032
fix             3 all nve
dump            2 all  xyz 50 Nickel_heat04.xyz.gz
run             50000
write_data      Ni_h04_*.nano
undump 2
unfix  2

fix             2 all temp/berendsen 0.4 0.4 0.032
fix             3 all nve
dump            2 all  xyz 500 Nickel_04.xyz.gz
run             50000
write_data      Ni_04_*.nano
undump 2
unfix  2

fix             2 all temp/berendsen 0.4 300. 0.032
fix             3 all nve
dump            2 all  xyz 500 Nickel_heat300.xyz.gz
run             50000
write_data      Ni_h300_*.nano
undump 2
unfix  2
```

```
fix             2 all temp/berendsen 300. 300. 0.032
fix             3 all nve
dump            2 all  xyz 500 Nickel_300.xyz.gz
run             50000
write_data      Ni_300_*.nano
undump 2
unfix  2

fix             2 all temp/berendsen 300. 600. 0.032
fix             3 all nve
dump            2 all  xyz 500 Nickel_heat600.xyz.gz
run             50000
write_data      Ni_h600_*.nano
undump 2
unfix  2

fix             2 all temp/berendsen 600. 600. 0.032
fix             3 all nve
dump            2 all  xyz 500 Nickel_600.xyz.gz
run             50000
write_data      Ni_600_*.nano
undump 2
unfix  2

fix             2 all temp/berendsen 600. 900. 0.032
fix             3 all nve
dump            2 all  xyz 500 Nickel_heat900.xyz.gz
run             50000
write_data      Ni_h900_*.nano
undump 2
unfix  2

# 900K long run

label           cargas
```

```
variable        b loop 1 100

fix             2 all temp/berendsen 900. 900. 0.032
fix             3 all nve
dump            2 all  xyz 500 Nickel_900_${b}.xyz.gz
run             50000
write_restart      Ni_900_${b}_*.nano
undump 2
unfix  2
next b
jump         Nickel_creation.in cargas

# Slow cooling

fix             2 all temp/berendsen 900. 800. 0.032
fix             3 all nve
dump            2 all  xyz 50 cNickel_cool800.xyz.gz
run             5000
write_data     cool_Nic800_*.nano
undump 2
unfix  2

fix             2 all temp/berendsen 800. 700. 0.032
fix             3 all nve
dump            2 all  xyz 50 cNickel_cool700.xyz.gz
run             5000
write_data     cool_Nic700_*.nano
undump 2
unfix  2


fix             2 all temp/berendsen 700. 600. 0.032
fix             3 all nve
dump            2 all  xyz 500 cNickel_cool600.xyz.gz
```

```
run             50000
write_data      cool_Nic600_*.nano
undump 2
unfix  2

fix             2 all temp/berendsen 600. 600. 0.032
fix             3 all nve
dump            2 all  xyz 500 cNickel_600.xyz.gz
run             50000
write_data      cool_Ni600_*.nano
undump 2
unfix  2

fix             2 all temp/berendsen 600. 500. 0.032
fix             3 all nve
dump            2 all  xyz 500 cNickel_cool500.xyz.gz
run             50000
write_data      cool_Nic500_*.nano
undump 2
unfix  2

fix             2 all temp/berendsen 500. 500. 0.032
fix             3 all nve
dump            2 all  xyz 500 cNickel_500.xyz.gz
run             50000
write_data      cool_Ni500_*.nano
undump 2
unfix  2

fix             2 all temp/berendsen 500. 400. 0.032
fix             3 all nve
dump            2 all  xyz 500 cNickel_cool400.xyz.gz
run             50000
write_data      cool_Nic400_*.nano
undump 2
```

```
unfix  2

fix             2 all temp/berendsen 400. 400. 0.032
fix             3 all nve
dump            2 all  xyz 500 cNickel_400.xyz.gz
run             50000
write_data     cool_Ni400_*.nano
undump 2
unfix  2

fix             2 all temp/berendsen 400. 300. 0.032
fix             3 all nve
dump            2 all  xyz 500 cNickel_cool300.xyz.gz
run             50000
write_data     cool_Nic300_*.nano
undump 2
unfix  2

fix             2 all temp/berendsen 300. 300. 0.032
fix             3 all nve
dump            2 all  xyz 500 cNickel_300.xyz.gz
run             50000
write_data     cool_Ni300_*.nano
undump 2
unfix  2

fix             2 all temp/berendsen 300. 200. 0.032
fix             3 all nve
dump            2 all  xyz 500 cNickel_cool200.xyz.gz
run             50000
write_data     cool_Nic200_*.nano
undump 2
unfix  2

fix             2 all temp/berendsen 200. 200. 0.032
```

```
fix             3 all nve
dump            2 all  xyz 500 cNickel_200.xyz.gz
run             50000
write_data     cool_Ni200_*.nano
undump 2
unfix  2

fix             2 all temp/berendsen 200. 100. 0.032
fix             3 all nve
dump            2 all  xyz 500 cNickel_cool100.xyz.gz
run             50000
write_data     cool_Nic100_*.nano
undump 2
unfix  2

fix             2 all temp/berendsen 100. 100. 0.032
fix             3 all nve
dump            2 all  xyz 500 cNickel_100.xyz.gz
run             50000
write_data     cool_Ni100_*.nano
undump 2
unfix  2

fix             2 all temp/berendsen 100. 50. 0.032
fix             3 all nve
dump            2 all  xyz 500 cNickel_cool50.xyz.gz
run             50000
write_data     cool_Nic50_*.nano
undump 2
unfix  2

fix             2 all temp/berendsen 50. 50. 0.032
fix             3 all nve
dump            2 all  xyz 500 cNickel_50.xyz.gz
run             50000
```

```
write_data     cool_Ni50_*.nano
undump 2
unfix  2

fix             2 all temp/berendsen 50. 0.4 0.032
fix             3 all nve
dump            2 all  xyz 500 cNickel_cool04.xyz.gz
run             50000
write_data     cool_Nic04_*.nano
undump 2
unfix  2

# keep at 0.4

label           cargas_cool

variable        b loop 1 100

fix             2 all temp/berendsen 0.4 0.4 0.032
fix             3 all nve
dump            2 all  xyz 500 cNickel_04_${b}.xyz.gz
run             50000
write_data      cool_Ni_04_${b}_*.nano
undump 2
unfix  2
next b
jump          Nickel_creation.in cargas_cool
unfix 3
unfix 11
```

Au shell creation

```
units metal
atom_style      atomic

boundary p p p

# load Nickel

read_data       ../cool_Ni_04_100_11120000.nano

# Define system

mass            1 58.6934
mass            2 196.96655

pair_style      eam/alloy

pair_coeff      * * ../AuNi.set Ni Au

#create Gold Atoms

region          Ninsert sphere 0.0 0.0 0.0 14.0 side out units box
region          Ginsert sphere 0.0 7.0 0.0 24.0 side in units box
region          hinsert  intersect  2 Ninsert Ginsert
create_atoms    2 random 2100 96532156 hinsert
group           Gold_de  type 2


# Initial low Temp. run to remove instabilities of random creation



fix             2 Gold_de temp/berendsen 0.01 0.001 0.032
fix             3 Gold_de nve/limit 0.01
```

```
dump            2 all  xyz 50 Gold_de_cool1.xyz.gz
run             5000
write_data      Au_de_001_*.nano
undump 2
unfix  2
unfix  3

fix             2 Gold_de temp/berendsen 0.001 0.0001 0.032
fix             3 Gold_de nve
dump            2 all  xyz 50 Gold_de_cool2.xyz.gz
run             5000
write_data      Au_de_0001_*.nano
undump 2
unfix  2


# initial slow heating


fix             2 Gold_de temp/berendsen 0.0001 0.4 0.032
fix             3 Gold_de nve
dump            2 all  xyz 50 Gold_de_heat04.xyz.gz
run             50000
write_data      Au_de_h04_*.nano
undump 2
unfix  2

fix             2 Gold_de temp/berendsen 0.4 0.4 0.032
fix             3 Gold_de nve
dump            2 all  xyz 500 Gold_de_04.xyz.gz
run             50000
write_data      Au_de_04_*.nano
undump 2
unfix  2
```

```
fix             2 Gold_de temp/berendsen 0.4 300. 0.032
fix             3 Gold_de nve
dump            2 all  xyz 500 Gold_de_heat300.xyz.gz
run             50000
write_data      Au_de_h300_*.nano
undump 2
unfix  2

fix             2 Gold_de temp/berendsen 300. 300. 0.032
fix             3 Gold_de nve
dump            2 all  xyz 500 Gold_de_300.xyz.gz
run             50000
write_data      Au_de_300_*.nano
undump 2
unfix  2

fix             2 Gold_de temp/berendsen 300. 600. 0.032
fix             3 Gold_de nve
dump            2 all  xyz 500 Gold_de_heat600.xyz.gz
run             50000
write_data      Au_de_h600_*.nano
undump 2
unfix  2

fix             2 Gold_de temp/berendsen 600. 600. 0.032
fix             3 Gold_de nve
dump            2 all  xyz 500 Gold_de_600.xyz.gz
run             50000
write_data      Au_de_600_*.nano
undump 2
unfix  2

fix             2 Gold_de temp/berendsen 600. 900. 0.032
fix             3 Gold_de nve
dump            2 all  xyz 500 Gold_de_heat900.xyz.gz
```

```
run             50000
write_data      Au_de_h900_*.nano
undump 2
unfix  2

# 900K long run

label           cargas

variable        b loop 1 300

fix             2 Gold_de temp/berendsen 900. 900. 0.032
fix             3 Gold_de nve
dump            2 all  xyz 500 Gold_de_900_${b}.xyz.gz
run             50000
write_restart      Au_de_900_${b}_*.nano
undump 2
unfix  2
next b
jump         Gold_cover.in cargas

# Slow cooling

fix             2 Gold_de temp/berendsen 900. 800. 0.032
fix             3 Gold_de nve
dump            2 all  xyz 50 cGold_de_cool800.xyz.gz
run             5000
write_data     cool_Auc800_*.nano
undump 2
unfix  2

fix             2 Gold_de temp/berendsen 800. 700. 0.032
fix             3 Gold_de nve
dump            2 all  xyz 50 cGold_de_cool700.xyz.gz
run             5000
```

```
write_data     cool_Auc700_*.nano
undump 2
unfix  2


fix             2 Gold_de temp/berendsen 700. 600. 0.032
fix             3 Gold_de nve
dump            2 all  xyz 500 cGold_de_cool600.xyz.gz
run             50000
write_data     cool_Auc600_*.nano
undump 2
unfix  2

fix             2 Gold_de temp/berendsen 600. 600. 0.032
fix             3 Gold_de nve
dump            2 all  xyz 500 cGold_de_600.xyz.gz
run             50000
write_data     cool_Au600_*.nano
undump 2
unfix  2

fix             2 Gold_de temp/berendsen 600. 500. 0.032
fix             3 Gold_de nve
dump            2 all  xyz 500 cGold_de_cool500.xyz.gz
run             50000
write_data     cool_Auc500_*.nano
undump 2
unfix  2

fix             2 Gold_de temp/berendsen 500. 500. 0.032
fix             3 Gold_de nve
dump            2 all  xyz 500 cGold_de_500.xyz.gz
run             50000
write_data     cool_Au500_*.nano
undump 2
```

```
unfix  2

fix             2 Gold_de temp/berendsen 500. 400. 0.032
fix             3 Gold_de nve
dump            2 all  xyz 500 cGold_de_cool400.xyz.gz
run             50000
write_data     cool_Auc400_*.nano
undump 2
unfix  2

fix             2 Gold_de temp/berendsen 400. 400. 0.032
fix             3 Gold_de nve
dump            2 all  xyz 500 cGold_de_400.xyz.gz
run             50000
write_data     cool_Au400_*.nano
undump 2
unfix  2

fix             2 Gold_de temp/berendsen 400. 300. 0.032
fix             3 Gold_de nve
dump            2 all  xyz 500 cGold_de_cool300.xyz.gz
run             50000
write_data     cool_Auc300_*.nano
undump 2
unfix  2

fix             2 Gold_de temp/berendsen 300. 300. 0.032
fix             3 Gold_de nve
dump            2 all  xyz 500 cGold_de_300.xyz.gz
run             50000
write_data     cool_Au300_*.nano
undump 2
unfix  2

fix             2 Gold_de temp/berendsen 300. 200. 0.032
```

```
fix             3 Gold_de nve
dump            2 all  xyz 500 cGold_de_cool200.xyz.gz
run             50000
write_data     cool_Auc200_*.nano
undump 2
unfix  2

fix             2 Gold_de temp/berendsen 200. 200. 0.032
fix             3 Gold_de nve
dump            2 all  xyz 500 cGold_de_200.xyz.gz
run             50000
write_data     cool_Au200_*.nano
undump 2
unfix  2

fix             2 Gold_de temp/berendsen 200. 100. 0.032
fix             3 Gold_de nve
dump            2 all  xyz 500 cGold_de_cool100.xyz.gz
run             50000
write_data     cool_Auc100_*.nano
undump 2
unfix  2

fix             2 Gold_de temp/berendsen 100. 100. 0.032
fix             3 Gold_de nve
dump            2 all  xyz 500 cGold_de_100.xyz.gz
run             50000
write_data     cool_Au100_*.nano
undump 2
unfix  2

fix             2 Gold_de temp/berendsen 100. 50. 0.032
fix             3 Gold_de nve
dump            2 all  xyz 500 cGold_de_cool50.xyz.gz
run             50000
```

```
write_data     cool_Auc50_*.nano
undump 2
unfix  2

fix             2 Gold_de temp/berendsen 50. 50. 0.032
fix             3 Gold_de nve
dump            2 all  xyz 500 cGold_de_50.xyz.gz
run             50000
write_data     cool_Au50_*.nano
undump 2
unfix  2

fix             2 Gold_de temp/berendsen 50. 0.4 0.032
fix             3 Gold_de nve
dump            2 all  xyz 500 cGold_de_cool04.xyz.gz
run             50000
write_data     cool_Auc04_*.nano
undump 2
unfix  2

# keep at 0.4

label           cargas_cool

variable        b loop 1 100

fix             2 Gold_de temp/berendsen 0.4 0.4 0.032
fix             3 Gold_de nve
dump            2 all  xyz 500 cGold_de_04_${b}.xyz.gz
run             50000
write_data      cool_Au_de_04_${b}_*.nano
undump 2
unfix  2
next b
jump          Gold_cover.in cargas_cool
```

2 Calculation of a Ni-Au phase diagram

As discussed in Chapter 3.3 and presented in Chapter 5, the CALPHAD method was used to calculate phase diagrams with a correction regarding the finite size of the system. The emperically determined data were taken from Sopouvsek et al.[124] In the first part, the Gibbs free energies for Au and Ni in either the liquid and solid phase are listed as a function of empirically determined parameters, typically specified for a specific temperature range. Also the excess energies are empirically determined and both the Gibbs energies as well as the excess energies are summed together to calculate the total Gibbs free energy of a liquid and a solid alloy. The transition temperature from solid to liquid can be determined via a comparison of Gibbs free of both phases as a function of temperature. Solidus and liquidus lines represent the compositions at which the the derivative of Gibbs free energy with respect to composition for both liquid and solid at the transition temperature is equal.

```
%% Gibbs energies for the pure elements and the excess energies
% Values taken from Sopousek et al. 2017

%Excess Gibbs Energy (S = solid, F = fcc, L = liquid)

%Gold (Au) (wrong values in the mid range, we use instead G from Ag-Au)
GLBAu = @(T) heaviside(929.4-T).*...
    (5613.14+97.4442*T-22.7545*T.*log(T)-0.00385924*T.^2-...
    3.79625*10^(-7)*T.^3-25097./T)+...
    heaviside(T-929.4).*heaviside(1337.33-T).*...
    (-81034.5+1012.31*T-155.707*T.*log(T)+0.0875602*T.^2-...
    1.15187*10^(-5)*T.^3+1.06372*10^(-7)./T)+...
    heaviside(T-1337.33).*heaviside(1735.8-T).*...
    (326620-2025.76*T+263.252*T.*log(T)-0.118217*T.^2+...
    8.92384*10^(-6)*T.^3-6.79998*10^(-7)./T)+...
    heaviside(T-1735.8).*...
    (418.217+155.887*T-30.9616*T.*log(T));
```

```
GFBAu = @(T) heaviside(929.4-T).*...
    (-6938.86+106.83*T-22.7545*T.*log(T)-0.00385924*T.^2-...
    3.79625*10^(-7)*T.^3-25097./T)+...
    heaviside(T-929.4).*heaviside(1337.33-T).*...
    (-93586.5+1021.7*T-155.707*T.*log(T)+0.0875602*T.^2-...
    1.15187*10^(-5)*T.^3+1.06372*10^(-7)./T)+...
    heaviside(T-1337.33).*heaviside(1735.8-T).*...
    (314068-2016.38*T+263.252*T.*log(T)-0.118217*T.^2+...
    8.92384*10^(-6)*T.^3-6.79998*10^(-7)./T)+...
    heaviside(T-1735.8).*...
    (-12133.8+165.273*T-30.9616*T.*log(T));

%Gold (Au) (inclusive nano correction)
GLAu = @(T,r) heaviside(1336.15-T).*...
    ((-3352+2.73*10^(-5)./r)+(215.885-7.98*10^(-10)./r).*T-...
    40.73*T.*log(T)+(0.0128756-2.18*10^(-13)./r).*T.^2-...
    2.535266*10^(-6)*T.^3+846536./T-7.069217*10^(9)./(T.^3)-...
    3.5899325*10^(-21)*T.^7)+...
    heaviside(T-1336.15).*...
    ((23570+2.73*10^(-5)./r)+(89.502-7.98*10^(-10)./r).*T-...
    23.454*T.*log(T)-(2.18*10^(-13)./r).*T.^2-8892561.16./T);

GSAu = @(T,r) heaviside(1336.15-T).*...
    ((-15745+4.380*10^(-5)./r)+(225.142-9.67*10^(-9)./r).*T-...
    40.73*T.*log(T)+0.0128756*T.^2-2.535266*10^(-6)*T.^3+...
    846536./T-7.069217*10^(9)./(T.^3))+...
    heaviside(T-1336.15).*...
    ((10886+4.380*10^(-5)./r)+(98.987-9.67*10^(-9)./r).*T-...
    23.454*T.*log(T)-8892561.1./T+1.72894275*10^(29)./(T.^9));

%Nickel (Ni)
GLBNi = @(T) heaviside(1728-T).*...
    (11235.5+108.457*T-22.096*T.*log(T)-0.0048407*T.^2-...
    3.82318*10^(-21)*T.^7)+...
    heaviside(T-1728).*...
```

```
    (-9549.82+268.598*T-43.1*T.*log(T));

GFBNi = @(T) heaviside(1728-T).*...
    (-5179.16+117.854*T-22.096*T.*log(T)-0.0048407*T.^2)+...
    heaviside(T-1728).*...
    (-27840.6+279.135*T-43.1*T.*log(T)+1.12754*10^(31)*T.^(-9));

%Nano Ni
GLNi = @(T,r) GLBNi(T)+2.91*10^(-5)./r-1.1*10^(-10)./r.*T-...
    7.09*10^(-13)*T.^2./r;

GSNi = @(T,r) GFBNi(T)+4.07*10^(-5)./r-5.43*10^(-9).*T./r;

%Excess Gibbbs energy
%L parameters
L0LB = @(T) 9500-5.429*T;
L1LB = @(T) 1614;

L0FB = @(T) 28696-11.274*T;
L1FB = @(T) -10945+6.154*T;
L2FB = @(T) 2519;

%Nano L parameters
L0L = @(T,r) L0LB(T)-3.83509*10^(-5)./r+1.30947*10^(-8)*T./r;
L1L = @(T,r) L1LB(T)+7.39585*10^(-5)./r-3.66543*10^(-8)*T./r;
L2L = @(T,r) -1.22542*10^(-5)./r+5.22776*10^(-9)*T./r;

L0S = @(T,r) L0FB(T)-3.73884*10^(-5)./r+7.73554*10^(-9)*T./r;
L1S = @(T,r) L1FB(T)+4.89981*10^(-5)./r-1.9097*10^(-8)*T./r;
L2S = @(T,r) L2FB(T)-2.16627*10^(-5)./r+9.00106*10^(-9)*T./r;

%Gibbs energy
GLE = @(XAu,XNi,T,r) XAu.*XNi.*(L0L(T,r)+L1L(T,r).*(XAu-XNi)+L2L(T,r).*...
    (XAu-XNi).^2);
GSE = @(XAu,XNi,T,r) XAu.*XNi.*(L0S(T,r)+L1S(T,r).*(XAu-XNi)+L2S(T,r).*...
```

```
    (XAu-XNi).^2);

%Ideal Gas Constant
R = 8.314459;

GToTL = @(XAu,XNi,T,r) GLE(XAu,XNi,T,r)+XAu.*GLAu(T,r)+XNi.*GLNi(T,r)+...
    R*T.*(XAu.*log(XAu)+XNi.*log(XNi));
GToTS = @(XAu,XNi,T,r) GSE(XAu,XNi,T,r)+XAu.*GSAu(T,r)+XNi.*GSNi(T,r)+...
    R*T.*(XAu.*log(XAu)+XNi.*log(XNi));

GToT = @(XAu,XNi,T,r) GToTS(XAu,XNi,T,r)-GToTL(XAu,XNi,T,r);

GbS = @(XAu,XNi,T,r) XAu.*GLAu(T,r)+XNi.*GLNi(T,r);

%% Initialisation

rvec = [1,7*10^(-9)]; %Size of particle [m]
XNiv = linspace(0.0001,0.9999,2000); %Fraction of Au in AgAu compound
XAuv = 1-XNiv;
TMatrix = zeros(length(rvec),length(XNiv));
lwidth = 2;
set(0,'DefaultAxesFontSize',18)

%% Phase diagram calculation
figure()
hold on
grid on
xlabel('X_{Ni}')
ylabel('T [K]')
ab = 10;

for u = 1:length(rvec)

    Tvec = zeros(size(XNiv));
    rr = rvec(u);
```

```
for k = 1:length(XNiv)
    Gfun = @(T) GToT(XAuv(k),XNiv(k),T,rr);
    Tvec(k) = fzero(Gfun,1000);
end

%Solidus and Liquidus curve
x = XNiv;
dx = x(2)-x(1);
dkv = zeros(1,length(XNiv));

for kk = 3:length(XNiv)-2

    TT = Tvec(kk);
    xx = XNiv(kk);

    %Derivative
    GprimeL = firstder(GToTL(1-x,x,TT,rr),dx);
    GprimeS = firstder(GToTS(1-x,x,TT,rr),dx);

    dlength = min([kk,length(XNiv)-kk])-2;
    dG = GprimeL((kk-1):-1:(kk-1-dlength))-...
        GprimeS((kk-1):1:(kk-1+dlength));
    dkv(kk) = find(abs(dG)==min(abs(dG)));

end

dkv(10:200) = 1;

dkv1 = 1:length(XAuv);
dkv1 = dkv1-dkv;

dkv2 = 1:length(XAuv);
dkv2 = dkv2+dkv;
```

```
    plot(XNiv(dkv1),Tvec,'k-','LineWidth',lwidth)
    plot(XNiv(dkv2),Tvec,'k-','LineWidth',lwidth)

    if u == 1
        p1 = plot(XNiv,Tvec,'r-','LineWidth',lwidth);
    else
        p2 = plot(XNiv,Tvec,'b-','LineWidth',lwidth);
    end

end

legend([p1 p2],{['r = ',num2str(rvec(1)),' m'],...
    ['r = ',num2str(rvec(2)),' m']},'Location','northwest')
hold off

function [fprime] = firstder(f,dx)
fprime = [0,(f(2:end)-f(1:end-1)),0];
end
```

Bibliography

[1] Notice that the α *bcc* phase is the most stable in the bulk of iron for temperatures below ca. 900 °C (see, e.g., Ref. 123). In contrast, the experiment shows that an *fcc* structure is favoured for the iron core of the synthesised Fe-Au core-shell nanoparticles in this work.

[2] To accelerate the convergence, the geometry relaxation of all atoms from (4×4×4) slabs was carried out at PBE level in a first step. Then, the vdW-corrected DFT scheme was applied on top of the PBE-relaxed structures and the atoms were allowed to relax further with the exception of cobalt.

[3] Z. Adamczyk. Particle adsorption and deposition: role of electrostatic interactions. *Advances in colloid and interface science*, 100:267–347, 2003.

[4] N. F. Aguirre, D. Mateo, A. O. Mitrushchenkov, M. Pi, and M. P. de Lara-Castells. Helium Mediated Deposition: Modeling the He-TiO 2(110)-(1×1) Interaction Potential and Application to the Collision of a Helium Droplet from Density Functional Calculations. *J. Chem. Phys.*, 136(12):124703, Mar. 2012.

[5] S. Alayoglu, A. U. Nilekar, M. Mavrikakis, and B. Eichhorn. Ru-pt core-shell nanoparticles for preferential oxidation of carbon monoxide in hydrogen. *Nat. Mater.*, 7(4):333–338, 04 2008.

[6] J. Ali, N. Ali, L. Wang, H. Waseem, and G. Pan. Revisiting the mechanistic pathways for bacterial mediated synthesis of noble metal nanoparticles. *J. Microbiol. Methods*, 159:18–25, 2019.

[7] V. Amendola and M. Meneghetti. Laser ablation synthesis in solution and size manipulation of noble metal nanoparticles. *Phys. Chem. Chem. Phys.*, 11(20):3805–3821, 2009.

[8] W. An and P. Liu. Rationalization of Au Concentration and Distribution in AuNiPt Core-Shell Nanoparticles for Oxygen Reduction Reaction. *ACS Catal.*, 5(11):6328–6336, 2015.

[9] F. Ancilotto, P. B. Lerner, and M. W. Cole. Physics of solvation. *J. Low Temp. Phys.*, 101(5-6):1123–1146, 1995.

[10] K. J. Andersson, F. Calle-Vallejo, J. Rossmeisl, and I. Chorkendorff. Adsorption-Driven Surface Segregation of the Less Reactive Alloy Component. *J. Am. Chem. Soc.*, 131(6):2404–2407, Jan. 2009.

[11] F. Baletto, C. Mottet, and R. Ferrando. Growth of three-shell onionlike bimetallic nanoparticles. *Phys. Rev. Lett.*, 90(13):135504, 2003.

[12] Z. Ban, Y. A. Barnakov, F. Li, V. O. Golub, and C. J. O'Connor. The Synthesis of Core-Shell Iron@gold Nanoparticles and their Characterization. *J. Mater. Chem.*, 15(43):4660–4662, 2005.

[13] D. Bhattacharyya, P. K. Sarswat, M. Islam, G. Kumar, M. Misra, and M. L. Free. Geometrical Modifications and Tuning of Optical and Surface Plasmon Resonance Behaviour of Au and Ag Coated TiO_2 Nanotubular Arrays. *RSC Adv.*, 5:70361–70370, 2015.

[14] P. E. Blöchl. Projector augmented-wave method. *Phys. Rev. B*, 50:17953–17979, Dec 1994.

[15] D. Bochicchio and R. Ferrando. Morphological instability of core-shell metallic nanoparticles. *Phys. Rev. B*, 87:165435, Apr 2013.

[16] P. Boyer, D. Ménard, and M. Meunier. Nanoclustered co-au particles fabricated by femtosecond laser fragmentation in liquids. *J. Phys. Chem. C*, 114(32):13497–13500, 2010.

[17] C. J. Brinker and G. W. Scherer. *Sol-gel science: the physics and chemistry of sol-gel processing*. Academic press, 2013.

[18] C. Broyden. The convergence of a class of double-rank minimization algorithms. *J. Inst. Math. Appl*, 6:76–90, 1970.

[19] H. Buchenau, E. L. Knuth, J. Northby, J. P. Toennies, and C. Winkler. Mass spectra and time-of-flight distributions of helium cluster beams. *J. Chem. Phys.*, 92(11):6875–6889, June 1990.

[20] L. Burr, I. Schubert, W. Sigle, C. Trautmann, and M. E. Toimil-Molares. Surface Enrichment in Au-Ag Alloy Nanowires and Investigation of the Dealloying Process. *J. Phys. Chem. C*, 119(36):20949–20956, 2015.

[21] C. Callegari and W. E. Ernst. Helium droplets as nanocryostats for molecular spectroscopy - from the vacuum ultraviolet to the microwave regime. In F. Merkt and M. Quack, editors, *Handbook of High Resolution Spectroscopy*. John Wiley & Sons, Chichester, 2011.

[22] C. Carreño-Gallardo, I. Estrada-Guel, C. López-Meléndez, and R. Martínez-Sánchez. Dispersion of silicon carbide nanoparticles in a aa2024 aluminum alloy by a high-energy ball mill. *Journal of alloys and compounds*, 586:S68–S72, 2014.

[23] A. Chakrabarty, E. T. Bentria, S. A. Omotayo, O. Bouhali, N. Mousseau, C. S. Becquart, and F. E. Mellouhi. Elucidating the role of extended surface defects at fe surfaces on co adsorption and dissociation. *App. Surf. Sci.*, 491:792 – 798, 2019.

[24] T. Chen and V. O. Rodionov. Controllable catalysis with nanoparticles: Bimetallic alloy systems and surface adsorbates. *ACS Catal.*, 6(6):4025–4033, 2016.

[25] A. Christensen, P. Stoltze, and J. Norskov. Size dependence of phase separation in small bimetallic clusters. *Journal of Physics: Condensed Matter*, 7(6):1047, 1995.

[26] F. Cleri and V. Rosato. Tight-binding potentials for transition metals and alloys. *Phys. Rev. B*, 48:22–33, Jul 1993.

[27] M. P. de Lara-Castells, N. F. Aguirre, H. Stoll, A. O. Mitrushchenkov, D. Mateo, and M. Pi. Communication: Unraveling the ^{4}He droplet-mediated soft-landing from *Ab initio*-assisted and time-resolved density functional simulations: Au@^{4}He$_{300}$/TiO$_2$(110). *J. Chem. Phys.*, 142:131101, 2015.

[28] M. P. de Lara-Castells, A. W. Hauser, J. M. Ramallo-López, D. Buceta, L. J. Giovanetti, M. A. López-Quintela, and F. G. Requejo. Increasing the optical response of tio 2 and extending it into the visible region through surface activation with highly stable cu 5 clusters. *Journal of Materials Chemistry A*, 7(13):7489–7500, 2019.

[29] R. J. Donelly. *Quantized Vortices in Helium II.* Cambridge University Press, Cambridge, 1991.

[30] S. Duan and R. Wang. Bimetallic nanostructures with magnetic and noble metals and their physicochemical applications. *Prog. Nat. Sci.: Mater. Int.*, 23(2):113 – 126, 2013.

[31] D. Duhl, K.-I. Hirano, and M. Cohen. Diffusion of iron, cobalt and nickel in gold. *Acta Metall.*, 11(1):1 – 6, 1963.

[32] S. V. Eremeev, A. G. Lipnitskii, A. I. Potekaev, and E. V. Chulkov. Vacancies at the surfaces of f.c.c. metals. *Russian Phys. J.*, 40:276–284, 1997.

[33] S. Eustis and M. A. El-Sayed. Why gold nanoparticles are more precious than pretty gold: Noble metal surface plasmon resonance and its enhancement of the radiative and nonradiative properties of nanocrystals of different shapes. *Chem. Soc. Rev.*, 35(3):209–217, 2006.

[34] H. Eyring. The activated complex in chemical reactions. *The Journal of Chemical Physics*, 3(2):107–115, 1935.

[35] Z. Fan, M. Shelton, A. K. Singh, D. Senapati, S. A. Khan, and P. C. Ray. Multifunctional plasmonic shell-magnetic core nanoparticles for targeted diagnostics, isolation, and photothermal destruction of tumor cells. *ACS Nano*, 6(2):1065–1073, 2012. PMID: 22276857.

[36] E. Fantino, A. Chiappone, I. Roppolo, D. Manfredi, R. Bongiovanni, C. F. Pirri, and F. Calignano. 3d printing of conductive complex structures with in situ generation of silver nanoparticles. *Adv. Mater.*, 28(19):3712–3717, 2016.

[37] D. L. Fedlheim and C. A. Foss. *Metal nanoparticles: synthesis, characterization, and applications.* CRC press, 2001.

[38] R. Fernández-Perea, L. F. Gómez, C. Cabrillo, M. Pi, A. O. Mitrushchenkov, A. F. Vilesov, and M. P. de Lara-Castells. Helium droplet-mediated deposition and aggregation of nanoscale silver clusters on carbon surfaces. *J. Phys. Chem. C*, 121(40):22248–22257, 2017.

[39] R. Ferrando. Symmetry breaking and morphological instabilities in core-shell metallic nanoparticles. *Journal of Physics: Condensed Matter*, 27(1):013003, 2014.

[40] R. Ferrando. *Structure and Properties of Nanoalloys*, volume 10. Elsevier, 2016.

[41] R. Fletcher. A new approach to variable metric algorithms. *Comput. J.*, 13(3):317–322, 1970.

[42] V. Gandhi, R. Ganesan, H. H. Abdulrahman Syedahamed, and M. Thaiyan. Effect of cobalt doping on structural, optical, and magnetic properties of zno nanoparticles synthesized by coprecipitation method. *J. Phys. Chem. C*, 118(18):9715–9725, 2014.

[43] J. Gao, H. Gu, and B. Xu. Multifunctional magnetic nanoparticles: Design, synthesis, and biomedical applications. *Acc. Chem. Res.*, 42(8):1097–1107, 2009.

[44] Y. Gao, J. Lim, S.-H. Teoh, and C. Xu. Emerging translational research on magnetic nanoparticles for regenerative medicine. *Chem. Soc. Rev.*, 44(17):6306–6329, 2015.

[45] Q. Ge, Y. Huang, F. Qiu, and S. Li. Bifunctional catalysts for conversion of synthesis gas to dimethyl ether. *App. Catal. A: General*, 167(1):23–30, 1998.

[46] L. Gell and H. Hakkinen. Theoretical Analysis of the $M_{12}Ag_{32}(SR)_{40}^{4-}$ and $XM_{12}Ag_{32}(SR)_{30}^{4-}$ Nanoclusters (M = Au, Ag; X = H, Mn). *J. Phys. Chem. C*, 119(20):10943–10948, 2015.

[47] R. Ghosh Chaudhuri and S. Paria. Core/shell nanoparticles: Classes, properties, synthesis mechanisms, characterization, and applications. *Chem. Rev.*, 112(4):2373–2433, 2012. PMID: 22204603.

[48] P. Giannozzi, S. Baroni, N. Bonini, M. Calandra, R. Car, C. Cavazzoni, D. Ceresoli, G. L. Chiarotti, M. Cococcioni, I. Dabo, A. Dal Corso, S. de Gironcoli, S. Fabris, G. Fratesi, R. Gebauer, U. Gerstmann, C. Gougoussis, A. Kokalj, M. Lazzeri, L. Martin-Samos, N. Marzari, F. Mauri, R. Mazzarello, S. Paolini, A. Pasquarello, L. Paulatto, C. Sbraccia, S. Scandolo, G. Sclauzero, A. P. Seitsonen, A. Smogunov, P. Umari, and R. M. Wentzcovitch. Quantum espresso: A modular and open-source software project for quantum simulations of materials. *J. Phys. Condens. Matter*, 21(39):395502, 2009.

[49] D. Goldfarb. A family of variable-metric methods derived by variational means. *Math. Comp.*, 24:23–26, 1970.

[50] L. F. Gomez, K. R. Ferguson, J. P. Cryan, C. Bacellar, R. M. P. Tanyag, C. Jones, S. Schorb, D. Anielski, A. Belkacem, C. Bernando, R. Boll, J. Bozek, S. Carron, G. Chen, T. Delmas, L. Englert, S. W. Epp, B. Erk, L. Foucar, R. Hartmann, A. Hexemer, M. Huth, J. Kwok, S. R. Leone, J. H. S. Ma, F. R. N. C. Maia, E. Malmerberg, S. Marchesini, D. M. Neumark, B. Poon, J. Prell, D. Rolles, B. Rudek, A. Rudenko, M. Seifrid, K. R. Siefermann, F. P. Sturm, M. Swiggers, J. Ullrich, F. Weise, P. Zwart, C. Bostedt, O. Gessner, and A. F. Vilesov. Shapes and vorticities of superfluid helium nanodroplets. *Science*, 345:906–909, 2014.

[51] L. F. Gomez, E. Loginov, R. Sliter, and A. F. Vilesov. Sizes of large he droplets. *J. Chem. Phys.*, 135(15):154201, 2011.

[52] L. F. Gomez, E. Loginov, and A. F. Vilesov. Traces of vortices in superfluid helium droplets. *Phys. Rev. Lett.*, 108:155302, 2012.

[53] S. Grimme, J. Antony, S. Ehrlich, and H. Krieg. A consistent and accurate ab initio parametrization of density functional dispersion correction (dft-d) for the 94 elements h-pu. *J. Chem. Phys.*, 132:154104, 2010.

[54] S. Grimme, S. Ehrlich, and L. Goerigk. Effect of the damping function in dispersion corrected density functional theory. *J. Comp. Chem.*, 32:1456–1465, 2011.

[55] L. Guo, J. Gu, X. Gong, S. Ni, and M. Song. Calphad aided design of high entropy alloy to achieve high strength via precipitate strengthening. *Science China Materials*, 63(2):288–299, 2020.

[56] R. P. Gupta. Lattice relaxation at a metal surface. *Phys. Rev. B*, 23:6265–6270, Jun 1981.

[57] G. Haberfehlner, P. Thaler, D. Knez, A. Volk, F. Hofer, W. E. Ernst, and G. Kothleitner. Formation of bimetallic clusters in superfluid helium nanodroplets analysed by atomic resolution electron tomography. *Nat. Commun.*, 6:8779, 2015.

[58] M. Hartmann, R. Miller, J. Toennies, and A. Vilesov. Rotationally Resolved Spectroscopy of SF_6 in Liquid Helium Clusters: A Molecular Probe of Cluster Temperature. *Phys. Rev. Lett.*, 75(8):1566–1569, 1995.

[59] A. W. Hauser, M. Schnedlitz, and W. E. Ernst. A coarse-grained monte-carlo approach to diffusion processes in metallic nanoparticles. *Eur. Phys. J. D*, 71(6):150, 2017.

[60] A. W. Hauser, A. Volk, P. Thaler, and W. E. Ernst. Atomic Collisions in Suprafluid Helium-Nanodroplets: Timescales for Metal-Cluster Formation Derived from He-Density Functional Theory. *Phys. Chem. Chem. Phys.*, 17(16):10805–10812, Apr. 2015.

[61] G. Henkelman, B. P. Uberuaga, and H. Jónsson. A climbing image nudged elastic band method for finding saddle points and minimum energy paths. *J. Chem. Phys.*, 113(22):9901–9904, 2000.

[62] U. Henne and J. P. Toennies. Electron capture by large helium droplets. *J. Chem. Phys.*, 108(22):9327–9338, 1998.

[63] P. K. Jain, X. Huang, I. H. El-Sayed, and M. A. El-Sayed. Noble metals on the nanoscale: Optical and photothermal properties and some applications in imaging, sensing, biology, and medicine. *Acc. Chem. Res.*, 41(12):1578–1586, 2008.

[64] X. Jia, J. Li, X. Zhang, and E. Wang. Controlling the synthesis and assembly of fluorescent au/ag alloy nanoclusters. *Chem. Commun.*, 51:17417–17419, 2015.

[65] H. Jónsson, G. Mills, and W. Jacobsen. *Classical and Quantum Dynamics in Condensed Phase Simulations*. World Scientific, Singapur, 1998.

[66] M. Jørgensen and H. Groenbeck. Selective acetylene hydrogenation over single-atom alloy nanoparticles by kinetic monte carlo. *Journal of the American Chemical Society*, 141(21):8541–8549, 2019.

[67] G. Kaptay. Nano-calphad: extension of the calphad method to systems with nano-phases and complexions. *Journal of Materials Science*, 47(24):8320–8335, 2012.

[68] U. R. Kattner. The calphad method and its role in material and process development. *Tecnol. Metal. Mater. Miner.*, 13:3–15, 2016.

[69] D. Knez, M. Schnedlitz, M. Lasserus, A. W. Hauser, W. E. Ernst, G. Kothleitner, and F. Hofer. Segregation in Ni-Au Nanoalloys Induced by Swift Electrons. *Appl. Phys. Lett.*, 115:123103, 2019.

[70] D. Knez, P. Thaler, A. Volk, G. Kothleitner, W. E. Ernst, and F. Hofer. Transformation Dynamics of Ni Clusters into NiO Rings under Electron Beam Irradiation. *Ultramicroscopy*, 176(Supplement C):105 – 111, 2017.

[71] E. L. Knuth and U. Henne. Average size and size distribution of large droplets produced in a free-jet expansion of a liquid. *J. Chem. Phys.*, 110(5):2664–2668, Feb. 1999.

[72] M. Krajewski. Magnetic-field-induced synthesis of magnetic wire-like micro- and nanostructures. *Nanoscale*, 9:16511–16545, 2017.

[73] G. Kresse and D. Joubert. From ultrasoft pseudopotentials to the projector augmented-wave method. *Phys. Rev. B*, 59:1758–1775, Jan 1999.

[74] G. Kresse and J. Furthmüller. Efficient iterative schemes for ab initio total-energy calculations using a plane-wave basis set. *Phys. Rev. B*, 54:11169, 1996.

[75] A. Kroupa, V. Vykoukal, T. Káňa, A. Zemanova, J. Pinkas, and M. Šob. The theoretical and experimental study of the sb-sn nano-alloys. *Calphad*, 64:90–96, 2019.

[76] K. Laasonen, E. Panizon, D. Bochicchio, and R. Ferrando. Competition between icosahedral motifs in AgCu, AgNi, and AgCo nanoalloys: a combined atomistic–DFT study. *The Journal of Physical Chemistry C*, 117(49):26405–26413, 2013.

[77] K. C. Lai, Y. Han, P. Spurgeon, W. Huang, P. A. Thiel, D.-J. Liu, and J. W. Evans. Reshaping, intermixing, and coarsening for metallic nanocrystals: Nonequilibrium statistical mechanical and coarse-grained modeling. *Chem. Rev.*, 119(11):6670–6768, 2019.

[78] C. Langlois, Z. Li, J. Yuan, D. Alloyeau, J. Nelayah, D. Bochicchio, R. Ferrando, and C. Ricolleau. Transition from core–shell to janus chemical configuration for bimetallic nanoparticles. *Nanoscale*, 4(11):3381–3388, 2012.

[79] M. Lasserus, D. Knez, M. Schnedlitz, A. W. Hauser, F. Hofer, and W. E. Ernst. On the passivation of iron particles at the nanoscale. *Nanoscale Advances*, 2:454, 2019.

[80] M. Lasserus, M. Schnedlitz, D. Knez, R. Messner, A. Schiffmann, F. Lackner, A. W. Hauser, F. Hofer, and W. E. Ernst. Thermally Induced Alloying Processes in a Bimetallic System at the Nanoscale: AgAu Sub-5 nm Core–Shell Particles Studied at Atomic Resolution. *Nanoscale*, 10:2017–2024, 2018.

[81] B. Li, Q. Zhang, L. Chen, P. Cui, and X. Pan. Vacancy-mediated diffusion of carbon in cobalt and its influence on co activation. *Phys. Chem. Chem. Phys.*, 12:7848–7855, 2010.

[82] Q. Liao, N. Li, S. Jin, G. Yang, and C. Wang. All-Solid-State Symmetric Supercapacitor Based on Co_3O_4 Nanoparticles on Vertically Aligned Graphene. *ACS Nano*, 9(5):5310–5317, 2015.

[83] P. López-Caballero, A. W. Hauser, and M. P. de Lara-Castells. Exploring the Catalytic Properties of Unsupported and TiO_2-Supported Cu_5 Clusters: CO_2 Decomposition to CO and CO2 Photoactivation. *J. Phys. Chem. C*, 123(37):23064–23074, 2019. PMID: 31598186.

[84] X. Lu, P. Yang, J. Luo, J. Ren, H. Xue, and Y. Ding. Tensile mechanical performance of ni–co alloy nanowires by molecular dynamics simulation. *RSC advances*, 9(44):25817–25828, 2019.

[85] Y. Lu, Y. Zhao, L. Yu, L. Dong, C. Shi, M.-J. Hu, Y.-J. Xu, L.-P. Wen, and S.-H. Yu. Hydrophilic Co@Au yolk/shell Nanospheres: Synthesis, Assembly, and Application to Gene Delivery. *Adv. Mater.*, 22(12):1407–1411, 2010.

[86] Z. Lu, D. Laks, S.-H. Wei, and A. Zunger. First-principles simulated-annealing study of phase transitions and short-range order in transition-metal and semiconductor alloys. *Physical Review B*, 50(10):6642, 1994.

[87] Y.-Y. Luk, M. Kato, and M. Mrksich. Self-assembled monolayers of alkanethiolates presenting mannitol groups are inert to protein adsorption and cell attachment. *Langmuir*, 16(24):9604–9608, 2000.

[88] H. Lv, Z. Xi, Z. Chen, S. Guo, Y. Yu, W. Zhu, Q. Li, X. Zhang, M. Pan, G. Lu, S. Mu, and S. Sun. A new core/shell niau/au nanoparticle catalyst with pt-like activity for hydrogen evolution reaction. *J. Am. Chem. Soc.*, 137(18):5859–5862, 2015. PMID: 25927960.

[89] S. Lysgaard, J. S. Mỳrdal, H. A. Hansen, and T. Vegge. A DFT-based genetic algorithm search for AuCu nanoalloy electrocatalysts for CO_2 reduction. *Physical Chemistry Chemical Physics*, 17(42):28270–28276, 2015.

[90] Z. Ma and S. Dai. Design of novel structured gold nanocatalysts. *ACS Catal.*, 1(7):805–818, 2011.

[91] A. L. Mackay. A dense non-crystallographic packing of equal spheres. *Acta Crystallographica*, 15(9):916–918, 1962.

[92] G. Maduraiveeran, R. Rasik, M. Sasidharan, and W. Jin. Bimetallic gold-nickel nanoparticles as a sensitive amperometric sensing platform for acetaminophen in human serum. *J. Electroanal. Chem.*, 808:259–265, 2018.

[93] H. Markides, M. Rotherham, and A. J. El Haj. Biocompatibility and toxicity of magnetic nanoparticles in regenerative medicine. *J. Nanomater.*, 2012:13:13–13:13, Jan. 2012.

[94] P. E. Blöch. Projector augmented-wave method. *Phys. Rev. B*, 50:17953, 1994.

[95] B. Medasani, M. Haranczyk, A. Canning, and M. Asta. Vacancy Formation Energies in Metals: A Comparison of MetaGGA with LDA and GGA Exchange–Correlation Functionals. *Comput. Mater. Sci.*, 101:96–107, 2015.

[96] M. Methfessel and A. T. Paxton. High-precision sampling for brillouin-zone integration in metals. *Phys. Rev. B*, 40:3616–3621, Aug 1989.

[97] P. Milani and W. A. deHeer. Improved pulsed laser vaporization source for production of intense beams of neutral and ionized clusters. *Review of scientific instruments*, 61(7):1835–1838, 1990.

[98] G. Mills, H. Jónsson, and G. K. Schenter. Reversible work transition state theory: Application to dissociative adsorption of hydrogen. *Surf. Sci.*, 324(2):305 – 337, 1995.

[99] H. J. Monkhorst and J. D. Pack. Special points for brillouin-zone integration. *Phys. Rev. B*, 13:5188–5192, 1976.

[100] G. E. Moore et al. Cramming more components onto integrated circuits, 1965.

[101] D. Nelli and R. Ferrando. Core-shell vs multi-shell formation in nanoalloy evolution from disordered configurations. *Nanoscale*, 11:13040–13050, 2019.

[102] T. D. Nguyen, C. C. Nguyen, and V. H. Tran. Molecular dynamics study of microscopic structures, phase transitions and dynamic crystallization in ni nanoparticles. *RSC Adv.*, 7:25406–25413, 2017.

[103] H. Okamoto, T. Massalski, T. Nishizawa, and M. Hasebe. The Au-Co (gold-cobalt) system. *Bull. Alloy Phase Diagrams*, 6(5):449–454, 1985.

[104] H. Okamoto, T. Massalski, L. Swartzendruber, and P. Beck. The Au-Fe (gold-iron) system. *Bull. Alloy Phase Diagrams*, 5(6):592–601, 1984.

[105] L. Onsager. Introductory talk. In *Proc. Int. Conf. Theor. Phys.*, pages 877–880. Science Council of Japan, Tokyo, 1953.

[106] J.-P. Palomares-Baez, E. Panizon, and R. Ferrando. Nanoscale effects on phase separation. *Nano Lett.*, 17(9):5394–5401, 2017.

[107] D. C. Papageorgopoulos and F. A. de Bruijn. Examining a potential fuel cell poison: A voltammetry study of the influence of carbon dioxide on the hydrogen oxidation capability of carbon-supported pt and ptru anodes. *J. Electrochem. Soc.*, 149(2):A140–A145, 2002.

[108] J. P. Perdew, K. Burke, and M. Ernzerhof. Generalized gradient approximation made simple. *Phys. Rev. Lett.*, 77:3865–3868, 1996.

[109] J. P. Perdew, A. Ruzsinszky, G. I. Csonka, O. A. Vydrov, G. E. Scuseria, L. A. Constantin, X. Zhou, and K. Burke. Erratum: Restoring the density-gradient expansion for exchange in solids and surfaces [phys. rev. lett. 100, 136406 (2008)]. *Phys. Rev. Lett.*, 102:039902, Jan 2009.

[110] A. Pimpinelli and J. Villain. *Physics of crystal growth*, volume 19. Cambridge university press, 1998.

[111] L. Pleth Nielsen, F. Besenbacher, I. Stensgaard, E. Laegsgaard, C. Engdahl, P. Stoltze, K. W. Jacobsen, and J. K. Nørskov. Initial growth of Au on Ni(110): Surface alloying of immiscible metals. *Phys. Rev. Lett.*, 71:754–757, Aug 1993.

[112] S. Plimpton. Fast parallel algorithms for short-range molecular dynamics. *J. Comp. Phys.*, 117(1):1 – 19, 1995.

[113] Z. Qiao, H. Feng, and J. Zhou. Molecular dynamics simulations on the melting of gold nanoparticles. *Phase Transitions*, 87(1):59–70, 2014.

[114] J. M. Rahm and P. Erhart. Understanding chemical ordering in bimetallic nanoparticles from atomic-scale simulations: The competition between bulk, surface, and strain. *The Journal of Physical Chemistry C*, 122(49):28439–28445, 2018.

[115] V. Rosato, M. Guillope, and B. Legrand. Thermodynamical and structural properties of f.c.c. transition metals using a simple tight-binding model. *Philos. Mag. A*, 59(2):321–336, 1989.

[116] S. M. Rossoulenejad-Mousavi and Y. Zhang. Interatomic potentials transferability for molecular simulations: A comparative study for platinum, gold and silver. *Sci. Rep.*, 8:2424, 2018.

[117] A. Samanta and I. L. Medintz. Nanoparticles and dna - a powerful and growing functional combination in bionanotechnology. *Nanoscale*, 8:9037–9095, 2016.

[118] M. Schnedlitz, R. Fernandez-Perea, D. Knez, M. Lasserus, A. Schiffmann, F. Hofer, A. W. Hauser, M. P. de Lara-Castells, and W. E. Ernst. Effects of the core location on the structural stability of ni–au core–shell nanoparticles. *J. Phys. Chem. C*, 123:20037–20043, 2019.

[119] M. Schnedlitz, M. Lasserus, D. Knez, A. W. Hauser, F. Hofer, and W. E. Ernst. Thermally induced breakup of metallic nanowires: Experiment and theory. *Phys. Chem. Chem. Phys.*, 19(14):9402–9408, 2017.

[120] M. Schnedlitz, M. Lasserus, R. Meyer, D. Knez, F. Hofer, W. E. Ernst, and A. W. Hauser. On the stability of core-shell nanoparticles for catalysis at elevated temperatures: Structural inversion in the ni-au system observed at atomic resolution. *Chem. Mater.*, 30:1113–1120, 2018.

[121] D. F. Shanno. Conditioning of quasi-Newton methods for function minimization. *Math. Comp.*, 24:647–656, 1970.

[122] H. Siekmann, C. Lüder, J. Faehrmann, H. Lutz, and K. Meiwes-Broer. The pulsed arc cluster ion source (pacis). *Zeitschrift für Physik D Atoms, Molecules and Clusters*, 20(1):417–420, 1991.

[123] P. Söderlind, J. A. Moriarty, and J. M. Wills. First-principles theory of iron up to earth-core pressures: Structural, vibrational, and elastic properties. *Phys. Rev. B*, 53:14063–14072, Jun 1996.

[124] J. Sopoušek, A. Kryštofová, M. Premović, O. Zobač, S. Polsterová, P. Brož, and J. Buršík. Au-ni nanoparticles: Phase diagram prediction, synthesis, characterization, and thermal stability. *Calphad*, 58:25–33, 2017.

[125] P. Srinoi, Y.-T. Chen, V. Vittur, M. D. Marquez, and T. R. Lee. Bimetallic nanoparticles: Enhanced magnetic and optical properties for emerging biological applications. *Appl. Sci.*, 8:1106, 2018.

[126] P. Strasser, S. Koh, T. Anniyev, J. Greeley, K. More, C. Yu, Z. Liu, S. Kaya, D. Nordlund, H. Ogasawara, M. F. Toney, and A. Nilsson. Lattice-strain control of the activity in dealloyed core–shell fuel cell catalysts. *Nat. Chem.*, 2(6):454, 2010.

[127] C. Sun, J. S. Lee, and M. Zhang. Magnetic nanoparticles in mr imaging and drug delivery. *Adv. Drug Deliv. Rev.*, 60(11):1252–1265, 2008.

[128] J. Sun, F. Yang, D. Zhao, C. Chen, and X. Yang. Integrated Logic Gate for Fluorescence Turn-on Detection of Histidine and Cysteine Based on Ag/Au Bimetallic Nanoclusters-Cu^{2+} Ensemble. *ACS Appl. Mater. Interfaces*, 7(12):6860–6866, 2015.

[129] Y. Sun, B. Wiley, Z.-Y. Li, and Y. Xia. Synthesis and optical properties of nanorattles and multiple-walled nanoshells/nanotubes made of metal alloys. *J. Am. Chem. Soc.*, 126(30):9399–9406, 2004.

[130] S. A. Tenney, W. He, C. C. Roberts, J. S. Ratliff, S. I. Shah, G. S. Shafai, V. Turkowski, T. S. Rahman, and D. A. Chen. CO-Induced Diffusion of Ni Atoms to the Surface of Ni-Au Clusters on TiO_2(110). *J. Phys. Chem. C*, 115(22):11112–11123, 2011.

[131] P. Thaler. *Buildup and Characterization of an Apparatus for the Synthesis of Metallic Nanoparticles Inside Helium Droplets.* PhD thesis, TU Graz, 2015.

[132] P. Thaler, A. Volk, D. Knez, F. Lackner, G. Haberfehlner, J. Steurer, M. Schnedlitz, and W. E. Ernst. Synthesis of nanoparticles in helium droplets – a characterization comparing mass-spectra and electron microscopy data. *J. Chem. Phys.*, 143(13):134201, 2015.

[133] P. Thaler, A. Volk, F. Lackner, J. Steurer, D. Knez, W. Grogger, F. Hofer, and W. E. Ernst. Formation of Bimetallic Core-Shell Nanowires Along Vortices in Superfluid He Nanodroplets. *Phys. Rev. B*, 90:155442, 2014.

[134] P. Thaler, A. Volk, M. Ratschek, M. Koch, and W. E. Ernst. Molecular dynamics simulation of the deposition process of cold Ag-clusters under different landing conditions. *J. Chem. Phys.*, 140:044326, 2014.

[135] J. Tiggesbäumker and F. Stienkemeier. Formation and properties of metal clusters isolated in helium droplets. *Phys. Chem. Chem. Phys.*, 9(34):4748–4770, 2007.

[136] J. P. Toennies and A. F. Vilesov. Superfluid helium droplets: a uniquely cold nanomatrix for molecules and molecular complexes. *Angew. Chem. Int. Ed.*, 43(20):2622–2648, 2004.

[137] M. Valden, X. Lai, and D. W. Goodman. Onset of catalytic activity of gold clusters on titania with the appearance of nonmetallic properties. *science*, 281(5383):1647–1650, 1998.

[138] L. Verlet. Computer "experiments" on classical fluids. i. thermodynamical properties of lennard-jones molecules. *Phys. Rev.*, 159:98, 1967.

[139] A. Volk. *Nanocluster and Nanowire Growth in Superfluid Helium Nanodroplets*. PhD thesis, TU-Graz, 2016.

[140] A. Volk, D. Knez, P. Thaler, A. W. Hauser, W. Grogger, F. Hofer, and W. E. Ernst. Thermal instabilities and Rayleigh breakup of ultrathin silver nanowires grown in helium nanodroplets. *Physical Chemistry Chemical Physics*, 17(38):24570–24575, Sept. 2015.

[141] A. Volk, P. Thaler, D. Knez, A. W. Hauser, J. Steurer, W. Grogger, F. Hofer, and W. E. Ernst. Correction: The impact of doping rates on the morphologies of silver and gold nanowires grown in helium nanodroplets. *Phys. Chem. Chem. Phys.*, 18:1451–1459 and 3359, 2016.

[142] A. Volk, P. Thaler, M. Koch, E. Fisslthaler, W. Grogger, and W. E. Ernst. High Resolution Electron Microscopy of Ag-Clusters in Crystalline and Non-crystalline Morphologies Grown Inside Superfluid Helium Nanodroplets. *J. Chem. Phys.*, 138:214312, 2013.

[143] A. B. Vysakh, C. L. Babu, and C. P. Vinod. Demonstration of synergistic catalysis in au@ni bimetallic core-shell nanostructures. *J. Phys. Chem. C*, 119(15):8138–8146, 2015.

[144] J. Wang, X.-G. Lu, B. Sundman, and X. Su. Thermodynamic assessment of the Au–Ni system. *Calphad*, 29(4):263–268, 2005.

[145] P. Wang, L. Lin, Z. Guo, J. Chen, H. Tian, X. Chen, and H. Yang. Highly Fluorescent Gene Carrier Based on Ag-Au Alloy Nanoclusters. *Macromol. Biosci.*, 16(1):160–167, 2016.

[146] B. N. Wanjala, J. Luo, R. Loukrakpam, B. Fang, D. Mott, P. N. Njoki, M. Engelhard, H. R. Naslund, J. K. Wu, L. Wang, O. Malis, and C.-J. Zhong. Nanoscale alloying, phase-segregation, and core-shell evolution of gold-platinum nanoparticles and their electrocatalytic effect on oxygen reduction reaction. *Chem. Mater.*, 22(14):4282–4294, 2010.

[147] Z. Wu, J. Liu, Y. Gao, H. Liu, T. Li, H. Zou, Z. Wang, K. Zhang, Y. Wang, H. Zhang, and B. Yang. Assembly-induced enhancement of cu nanoclusters luminescence with mechanochromic property. *J. Am. Chem. Soc.*, 137(40):12906–12913, 2015. PMID: 26397821.

[148] Y. Xia, X. Xia, Y. Wang, and S. Xie. Shape-controlled synthesis of metal nanocrystals. *MRS Bulletin*, 38(4):335–344, 2013.

[149] Y. Xia, Y. Xiong, B. Lim, and S. E. Skrabalak. Shape-controlled synthesis of metal nanocrystals: simple chemistry meets complex physics? *Angewandte Chemie International Edition*, 48(1):60–103, 2009.

[150] Z. Yan, M. G. Taylor, A. Mascareno, and G. Mpourmpakis. Size-, shape-, and composition-dependent model for metal nanoparticle stability prediction. *Nano Letters*, 18(4):2696–2704, 2018. PMID: 29578341.

[151] T. Young, F. Chen, and C. M. Burba. A quantitative investigation of ion clusters in a double salt ionic liquid by both vibrational spectroscopy and molecular dynamics simulation. *The Journal of Physical Chemistry B*, 2020.

[152] S. Zhao, G. M. Stocks, and Y. Zhang. Defect energetics of concentrated solid-solution alloys from ab initio calculations: Ni 0.5 Co 0.5, Ni 0.5 Fe 0.5, Ni 0.8 Fe 0.2 and Ni 0.8 Cr 0.2. *Phys. Chem. Chem. Phys.*, 18:24043–24056, 2016.

[153] S. Zhou, G. Jackson, and B. Eichhorn. AuPt Alloy Nanoparticles for CO-Tolerant Hydrogen Activation: Architectural Effects in Au-Pt Bimetallic Nanocatalysts. *Adv. Funct. Mater.*, 17(16):3099–3104, 2007.

[154] S. Zhou, H. Yin, V. Schwartz, Z. Wu, D. Mullins, B. Eichhorn, S. H. Overbury, and S. Dai. In Situ Phase Separation of NiAu Alloy Nanoparticles for Preparing Highly Active Au/NiO CO Oxidation Catalysts. *ChemPhysChem*, 9(17):2475–2479, Dec. 2008.

[155] X. W. Zhou, R. A. Johnson, and H. N. G. Wadley. Misfit-Energy Increasing Dislocations in Vapor-Deposited CoFe/NiFe Multilayers. *Phys. Rev. B*, 69(144113):10, 2004.

[156] J. Zhu. Surface Plasmon Resonance from Bimetallic Interface in Au-Ag Core-Shell Structure Nanowires. *Nanoscale Res. Lett.*, 4(9):977–981, 2009.